In the name of God

Institute for Research in Fundamental Sciences

Institute for Studies in Theoretical Physics and Mathematics (IPM)

School of Nano Science

Ph.D. Thesis

A molecular dynamics approach to study the thermal conductivity of amyloid beta in organic surface

By
Neda Rafieiolhosseini

Supervisor
Prof. Mohammad Reza Ejtehadi

Advisor
Dr. Ali Hassanali

March 2021

To my wonderful husband

Ali

and my kind parents

Jalal & Mahin

for their love and support.

Acknowledgments

I appreciate that I have been really fortunate to work in the scientific, active and friendly group of Prof. Mohammad Reza Ejtehadi. I enjoyed the scientific discussions and exchange of ideas with all the motivated members of the group. I sincerely thank Prof. Mohammad Reza Ejtehadi for his professional supervision, endless help, and generous support. He taught me many lessons that helped me not only in my carrier but also in my life.

Secondly, I appreciate all the help and support I received from all of my family members, especially my wonderful husband, Ali, who always motivates me. I am grateful to all the help and support I have always received and am still receiving from my kind parents, my brother, and my sister.

I would like to acknowledge the IPM staff for providing me with computational facilities during my Ph.D. and for all their help and support during my study. I would also like to warmly thank Dr. Ali Hassanali for his contribution to my Ph.D. thesis and for his help and support during my stays at ICTP.

I am so grateful that I could be one of the DAAD scholarship holders in the last years of my Ph.D. and I would like to thank this organization for providing me with a one-year research grant. I would also like to sincerely thank Prof. Dr. Daniel Hoffmann for hosting me in his group (Bioinformatics and Computational Biophysics) and providing me with the required computational facilities during my stay at the University of Duisburg-Essen.

At the end, I would like to show my gratitude to all of the persons including my previous teachers and friends who paved the way for my education.

Abstract

The cell membrane plays an important role in signaling, protecting, and the transportation of ions between the intracellular and the extracellular environments of a cell. In spite of the wide literature, only a few has been dedicated to the thermal properties of the membrane. Whether the thermal conductivity of the cell membrane is affected by its components specifically cholesterol or the membrane proteins has not been investigated so far. Although the experimental measurement of the membrane thermal conductivity was not available until very recently, computational methods have been widely used for this purpose. Nonequilibrium molecular dynamics simulation is one of the commonly-used computational techniques to study transport properties of a system. Thermal conductivity of a model membrane was first computed by Müller et al. using their devised method called Müller-Plathe technique, which has been used by others in the last few years as well.

Among different types of nanoparticles, silica or amorphous silicon dioxide (SiO_2) has gained much attention due to the specific features including low toxicity, low cost and high biocompatibility. Silica nanoparticles can affect the behavior of the nearby biomolecules in different ways depending on the nanoparticle size, curvature, surface charge, surface chemistry, and also the type of surface functional groups.

The effect of organic/inorganic surfaces on the behavior of biomolecules and the impact of biomolecules on the surfaces have gained much attention in recent years. In the present study, we use classical molecular dynamics simulation to investigate the interaction of specific biomolecules with two different surfaces: cell membrane and amorphous silica.

In the first part of this thesis, we carry out nonequilibrium molecular dynamics simulation to investigate the relation between the concentration of cholesterol and the thermal conductivity of a model membrane. Our results suggest an increase in the membrane thermal conductivity upon increasing the concentration of cholesterol in the membrane. Moreover, we find that the asymmetric distribution of cholesterol in the two membrane leaflets decreases thermal conductivity.

We also find a rectification effect when heat flows in opposite directions through a model membrane decorated with the amyloid precursor protein. The results of this study apply to the advancement of selective treatment methods, as well as the development of new materials such as biological rectifiers.

In the second part, we conduct molecular dynamics simulations of a hydrophobic segment of the amyloid beta peptide near the amorphous silica water interface. The peptide binds strongly to the surface via the hydrophobic and electrostatic interactions. These interactions affect the specific conformations and also the rotational mobility of the peptide. The orientation of the peptide relative to the surface is likely to play an important role in the fate of amyloid aggregation at the surface of silica nanoparticles.

Keywords

Thermal conductivity, Amyloid beta, Organic surfaces, Molecular dynamics simulation, Amorphous silica, Clustering, Autocorrelation

Contents

List of Figures

xiv

List of Tables

List of Abbreviations

Aβ	Amyloid Beta
AD	Alzheimer's Disease
AFM	Atomic Force Microscopy
APP	Amyloid Precursor Protein
BD	Brownian Dynamics
CHARMM	Chemistry at HARvard Molecular Mechanics
CHL	Cholesterol
DNA	DeoxyriboNucleic Acid
GM	Ganglioside lipids
DPPC	DipalmitoylPhosPhatidylCholine
GROMACS	GROningen MAchine for Chemical Simulations
LAMMPS	Large-scale Atomic/Molecular Massively Parallel Simulator
MC	Monte Carlo
MD	Molecular Dynamics
NEMD	NonEquilibrium Molecular Dynamics
OPM	Orientation of Protein in Membrane
PC	PhosphatidylCholine
PDB	Protein Data Bank
PE	PhosphatidylEthanolamine
PME	Particle Mesh Ewald
PS	PhosphatidylSerine
RDF	Radial Distribution Function
SM	SphingoMelin
SNP	Silica Nano Particle
SS	Stress Strain
ssNMR	solid state Nuclear Magnetic Resonance
VMD	Visual Molecular Dynamics

Chapter 1

Introduction

1.1 Computational methods to study biological systems

An exact description of the dynamics and states of a molecular system is possible through the time-dependent Schrödinger equation. However, because of the multi-dimensionality of the problem and the extensive degrees of freedem this equation does not have an exact solution at the present time. Approximations to handle this problem include Born-Oppenheimer and Hartree-Fock [11, 12]. In Born-Oppenheimer approximation it is assumed that the nuclei are fixed (in the timescale of electron vibrations) while in the Hartree-Fock approximation, the movement of one electron is considered to be independent of the other electrons. Using these approximations, the Schrödinger equation can be solved numerically for up to 50 to 100 atoms which is not applicable to large biomolecules.

Computer simulations make a bridge between theory and experiment [13]. To study large molecules, a classical approximation is required to speed up the calculations. Molecular mechanics (MM) fulfills this aim. Considering atoms as spheres connected to each other by bonds, MM calculates the motion of atoms based on van der Waals and Coulomb interactions [11, 14]. In this method, correctness and precision of the results highly depend on the way the parameters are given to the model. The parameters are usually provided by theoretical (quantum mechanical calculations) means or evaluated by empirical values [12].

1.1.1 Molecular dynamics simulation

In general, molecular simulations provide an understanding of macroscopic properties of a molecular system based on the microscopic or intermolecular interactions [15]. Molecular Dynamics (MD), Monte Carlo (MC), and Brownian Dynamics (BD) simulation are commonly used methods of molecular simulation. Monte Carlo is useful to analyze systems at thermodynamic equilibrium, but is not suitable for dynamical properties. Molecular dynamics can be used for both purposes. MD is especially useful for the investigation of transport properties or to study a system at nonequilibrium condition [16].

In molecular dynamics simulation, the particles are moved based on the numerical solution of classical equations of motion. A very general description of a molecular dynamics algorithm for a system consisting of N particles is as follows:

1- Initial positions and velocities are assigned to particles in the simulation box. Conditions at which the simulation should be done (temperature, pressure, etc.) are determined as well.

2- The forces acting on each particle is obtained by solving Newton's equations of motion (Equation 1.1).

$$f_i = m\ddot{r}_i \tag{1.1}$$

where f is force acting on particle i, m is mass and r indicates the position of particle i ($i = 1, ..., N$).

3- The equations of motion are integrated and accordingly, the system is evolved over time. Several algorithms have been designed for this purpose. The necessary feature of all these algorithms is time-reversibility. Verlet and leap-frog are two examples. Verlet method for estimating new positions of particles is described in Equation 1.2. This equation indicates that the error in the calculation of positions in Verlet method is in the order of Δt^4, where Δt is the simulation time step. Velocities are

calculated using Equation 1.3 with an error in the order of Δt^2.

$$r(t + \Delta t) = 2r(t) - r(t - \Delta t) + \frac{f(t)}{m}\Delta t^2 + O(\Delta t^4) \tag{1.2}$$

$$v(t) = \frac{r(t + \Delta t) - r(t - \Delta t)}{2\Delta t} + O(\Delta t^2) \tag{1.3}$$

It should be mentioned that there are other algorithms that computes the velocity more accurately than Verlet does. On the other hand, the error depends on the simulation time step as well. The smaller the time step, the more accurate the results. However, an optimized algorithm is the one that compromises between the accuracy and the computational cost. What is necessary to consider is that the time step of the simulation must be smaller than the fastest motions in the system. In the biological systems, such as the ones we have in our study, the oscillation of hydrogen atoms is the fastest motion which is in the order of 1-10 fs. Therefore, the time step of our simulations cannot be smaller than 1 fs.

4- Finally, the averages of the desired quantities are calculated.

Thermodynamic ensembles (NVE, NVT, NPT)

In molecular dynamics simulations, microscopic behavior of the system can be obtained using the positions and velocities of the particles at each time step. A link between the microscopic world and the macroscopic properties of the system is then required for the calculation of thermodynamic observables such as pressure or heat capacity. Statistical mechanics provides this link via the notion of ensembles [17]. Under ergodic condition, the ensemble average of the system is equal to the time average over the trajectories obtained from MD simulations.

The most fundamental ensemble, called the microcanonical (NVE) ensemble, describes a system consisting of N particles in a constant volume V with a fixed internal energy E. However, to have a microcanonical ensemble the system should be isolated from the environment. This is usually far from the usual conditions in the experiments [17].

To better reflect the experimental setups, the canonical ensemble (NVT) has been

3

developed in which the constant control variables are: the number of particles N, the volume of the system V, and the temperature T. Considering the relation between the temperature and the kinetic energy of a system (Eq. 1.4), the temperature of a system can be controlled by manipulating the velocities of the particles in that system.

$$\sum_{i=1}^{N} \frac{p_i^2}{2m_i} = \frac{3Nk_BT}{2} \tag{1.4}$$

where N is the number of particles in the system, k_B is the Boltzmann constant, T is the absolute temperature in kelvin, and p_i and m_i are the momentum and mass of the particles, respectively.

In molecular dynamics simulation, to keep the temperature of the system constant, it is necessary to include a thermostat in the Hamiltonian of the system. To this aim, several algorithms have been developed. Some examples are: Berendsen [18], Nose-Hoover [19, 20], and Langevin [21]. Temperature coupling is more stable in the Langevin thermostat in which the equations of motion are changed either by the inclusion of a "random force" or by the addition of a deterministic "frictional force" which is proportional to particle velocities. For a more detailed discussion of Langevin equation the reader is referred to sectoin 12.2 in reference [22].

Doing experiments under constant pressure is more usual in the laboratory. Therefore, the isothermal-isobaric (NPT) ensemble has been developed to better mimic the experimental conditions. In this ensemble, the system is coupled not only to a thermal bath, which keeps the system at a constant temperature, but also to an isotropic piston which allows the system volume to fluctuate [17].

Force Fields

As we mentioned earlier, to move the particles at each step of the simulation, we need to know the forces acting on them. As Equation 1.5 shows, force is derived from the potential energy. The exact form of the potential energy and its relative parameters are provided in files called force fields.

$$f_i = \frac{\partial}{\partial r_i} u \tag{1.5}$$

Potential energy of a system generally consists of two parts: intramolecular and intermolecular potentials.

Intramolecular potential which refers to the potential energy between atoms inside a molecule, arises from stretching, bending, and out of plane motions (Equation 1.6). A simple yet sufficiently accurate model to describe these motions is a harmonic potential. Equations 1.7, 1.8, and 1.9 show different terms of the intramolecular potential. In these equations, k is the spring constant and r_{eq} and θ_{eq} are the equilibrium values for the bond length and angle, respectively. For more details, the reader is referred to the reference [13].

$$U_{intramolecular} = U_{bonds} + U_{bend-angles} + U_{torsion-angles} \tag{1.6}$$

$$U_{bonds} = \frac{1}{2} \sum_{bonds} k_{ij}^s (r_{ij} - r_{eq})^2 \tag{1.7}$$

$$U_{bend-angles} = \frac{1}{2} \sum_{bend-angles} k_{ijk}^\theta (\theta_{ijk} - \theta_{eq})^2 \tag{1.8}$$

$$U_{torsion-angles} = \frac{1}{2} \sum_{torsion-angles} \sum_m k_{ijkl}^{\phi,m} (1 + cos(m\phi_{ijkl} - \gamma_m)) \tag{1.9}$$

Intermolecular potential refers to the potential between nonbonded atoms. Two terms of the intermolecular potential are Lennard-Jones (LJ) and Coulomb potentials. LJ is a two-body potential which is described by Equation 1.10.

$$v^{LJ}(r) = 4\epsilon \left((\frac{\sigma}{r})^{12} - (\frac{\sigma}{r})^6 \right) \tag{1.10}$$

where σ is the distance between two atoms at which the potential energy is zero, ϵ is the well depth of the potential function and r is the distance between two atoms.

The Coulomb potential exists in the presence of charged particles and is described

by Equation 1.11.

$$v^{Coulomb}(r) = \frac{Q_1 Q_2}{4\pi\epsilon_0 r} \tag{1.11}$$

where Q_1 and Q_2 are charges and ϵ_0 is the free space permittivity.

Nonequilibrium molecular dynamics

From a statistical mechanical point of view, a nonequilibrium system is modeled as an equilibrium ensemble which is perturbed by a field. This field prevents the system from relaxing to its equilibrium state by doing work on it [23]. This results in the generation of heat in the system.

In equilibrium, conjugate thermodynamic variables (such as pressure and volume) generate conjugate ensembles (NVT and NPT). Similarly, conjugate state variables define conjugate ensembles at nonequilibrium. For instance, consider a thermostat acting on a system at nonequilibrium to remove the dissipated heat from the system. The rate of heat flow (dQ/dt) in the system can be written as a multiplication of a thermodynamic force and a thermodynamic flux. Therefore, a nonequilibrium ensemble in which the thermodynamic force is the independent state variable is equivalent to an ensemble in which the state variable is the thermodynamic flux. This is a very similar concept to the paired Thévenin and Norton ensembles in the electrical circuit theory [23].

In nonequilibrium molecular dynamics (NEMD) simulation, we are interested in finding system response to a perturbation [24]. Most of the times, the perturbation is a thermodynamic force while the response is a thermodynamic flux. Simulation provides us with the microscopic expressions that we need to evaluate these fluxes. Where the flux is directly proportional to the driving force, the Green-Kubo formalism can be used to study nonlinear properties using the equilibrium simulations. However, it is limited to the linear regime.

NEMD is widely used to obtain transport properties of a system. Transport equations relate the fluxes of properties to the property gradient. Among the many applications of NEMD, we refer to the measurement of thermal conductivity which is the scope of this study. There are two possible approaches to obtain the thermal

conductivity of a material. In the first approach, which is called the direct method, one can create a temperature gradient across the system and measure the rate of heat flow throughout the system. The thermal conductivity coefficient is then obtained by dividing the rate of heat flow to the temperature gradient. Because of some drawbacks, including highly fluctuating heat flow and slow convergence of the system, an alternative method is to continuously apply a nonphysical heat flux to the system until a physical heat flux establishes throughout the system. After some time, the physical and nonphysical heat flow rates are equalized and the system reaches a so-called steady state. In this situation, a stable temperature gradient establishes across the system. This method is called reverse nonequilibrium molecular dynamics (RNEMD) and was first proposed by Müller-Plathe [25]. The Müller-Plathe technique can be simply implemented, is compatible with the periodic boundary condition, and keeps the total energy and total linear momentum conserved. This method samples temperature gradient instead of heat flux. This is a real advantage because other methods such as Green-Kubo [25] suffers from the slow convergence of heat flux and its autocorrelation function.

1.1.2 Cluster analysis

In cluster analysis, the aim is to find patterns in a data set by grouping the observations. To optimize clustering, objects within a cluster should be similar while those between clusters must be dissimilar. It should be noted that in clustering, the number of groups is not known in advance. There are many types of clustering algorithms based on different measures of similarity. In many of clustering algorithms, a measure of distance is used to group the observations into clusters. A common distance function is the Euclidean distance.

Hierarchical and partitioning clustering are two common methods of clustering. In hierarchical clustering each observation is initially considered as a cluster and in a sequential process, clusters merge together until a whole cluster containing all the observations is formed. This procedure which is called agglomerative hierarchical approach can also be reversed. In this case, it will start with one cluster containing all the observations which divides into clusters at each step. This is called divisive hierarchical approach. However, the former approach is more common.

Results of a hierarchical clustering approach is illustrated using a tree diagram called "dendrogram" which indicates all the steps of hierarchical procedure as well as the distances at which clusters are merged together. Based on the size of the distances, one can make a decision about the optimal number of clusters. Among the many available agglomerative algorithms, Ward's and the average linkage method have gained more popularity because of their overall performance. To find more details on the method, the reader is referred to the reference book [26] and the main papers [27, 28].

Ward's Method

In Ward's method, also known as the incremental sum of squares method, the within-cluster (squared) distances as well as the between-cluster (squared) distances are used as measures of similarity. We consider AB to be the cluster obtained after merging clusters A and B. The sum of within-cluster distances can then be obtained.

$$D_A = \sum_{i=1}^{n_A} (y_i - \overline{y}_A)'(y_i - \overline{y}_A), \qquad (1.12)$$

$$D_B = \sum_{i=1}^{n_B} (y_i - \overline{y}_B)'(y_i - \overline{y}_B), \qquad (1.13)$$

$$D_{AB} = \sum_{i=1}^{n_{AB}} (y_i - \overline{y}_{AB})'(y_i - \overline{y}_{AB}) \qquad (1.14)$$

where $\overline{y}_{AB} = (n_A \overline{y}_A + n_B \overline{y}_B)/(n_A + n_B)$ and n_A, n_B, and $n_{AB} = n_A + n_B$ are sizes of A, B, and AB, respectively. In Ward's method, each two clusters that minimize I_{AB}, as defined in Equation 1.15, can be combined together. This is exactly equivalent to minimizing the between-clusters distances.

$$I_{AB} = D_{AB} - (D_A + D_B) \qquad (1.15)$$

where D_A and D_B are within-cluster distances (distances of each item in the cluster from the cluster mean vector) for clusters A and B, respectively, and D_{AB} is the distance between clusters A and B.

Hierarchical clustering

In hierarchical clustering, each observation is initially considered as a cluster and in an iterative manner, the number of clusters and elements within a cluster is optimized based on the between- and within-clusters distances [28].

1.2 Interaction between biomolecules and surfaces

The interaction of biomolecules with surfaces has been a topic of interest in many applications and hence, the target of many studies for decades [29, 30, 31, 32, 33, 34]. One of the main motivations for this is the importance of biomolecule-surface interaction specifically at the nano scale. The large surface-area-to-volume ratio of NPs leads to the dominance of the behavior of the surface atoms over the interior ones and consequently affects the physical, chemical, and biological interaction of nano sized particles with other materials. Unique properties of NPs made them suitable candidates for potential applications from industry to medicine including drug delivery, gene delivery, biosensing, and bioimaging [35, 36, 37, 38, 39, 40, 41]. However, the adsorption of a variety of proteins on the surface of NPs modify the NP properties such as their physicochemical identity, cellular uptake, and toxicity. Therefor, a prior knowledge about the interaction of biomolecules with NPs is required.

Interaction of NPs with biomolecules may result in one of the two immobilization mechanisms: simple adsorption or chemical linkage. Simple adsorption includes van der Waal forces, hydrogen bonding, or ionic interactions which are categorized as non-covalent forces. An example is the immobilization of enzymes on the surface of NPs in which the active site of the enzyme is not disturbed. Difference in chemical bonds, which results in different physical properties, usually immobilize biomolecules interacting with a biocompatible matrix such as a phospholipid membrane. In this case, not only physical properties of the biomolecules (such as hardness, melting point, and conductivity) but also their biological activities are altered as well [42].

Alzheimer's disease and the formation of Amyloids

Alzheimer's disease is a neurodegenerative disorder leading to the neural cell death and brain shrinkage. Many factors are involved in the initiation and the progression of Alzheimer's disease. Aging, genetics, and heredity are known to be the main risk factors. Furthermore, those suffering from diabetes, high blood pressure, and high levels of cholesterol, who are also at risk of vascular diseases, are at a higher risk of AD.

Several studies have addressed the main cause of neural cell death. Amyloid hypothesis which appears to be the most widely accepted one during the last 20 years, proposes that aggregation of a protein called Amyloid beta ($A\beta$) leads to plaque formation that are neurotoxic and can cause neural cell death. Plaques also damage synapses and block cell signaling. Moreover, accumulation of $A\beta$ in vascular system of the cerebellum causes constriction in blood vessels and neuronal dysfunction, which was found to be associated with AD [43]. However, more recent studies suggest that although $A\beta$ is associated with the development of AD, it has not been proved to be the main cause of AD according to several reasons. Firstly, removal of $A\beta$ plaques by pharmaceutical methods had no effect neither on the progression of AD nor on the memory improvement. Secondly, neuronal loss was observed in the areas of the brain far from the areas where $A\beta$ was accumulated. Thirdly, $A\beta$ aggregations emerge in the areas of neocortex and hippocampus many years before the appearance of clinical symptoms of AD. So, what triggers the disease is still a matter of debate.

1.2.1 Effect of surface on the amyloid formation

Among several studies on the interaction of different biomolecules with surfaces, many have focused on the effect of surface on amyloid formation. As the hallmarks of many neurodegenerative disorders such as Alzheimer's or Huntington's disease [44], amyloid fibrils are formed when unfolded proteins aggregate and form beta sheet structures. Amyloid beta is one of the well-known amyloidogenic proteins in this respect.

Structure of amyloid beta

Aβ(1-42) is a sequence of amino acids as listed in the following:

Asp-Ala-Glu-Phe-Arg-His-Asp-Ser-Gly-Tyr-Glu-Val-His-His-Gln-**Lys-Leu-Val-Phe-Phe-Ala-Glu-Asp**-Val-Gly-Ser-Asn-Lys-Gly-Ala-Ile-Ile-Gly-Leu-Met-Val-Gly-Gly-Val-Val-Ile-Ala

The sequence 16-23 is known to be amyloidogenic and more important in fibril formation [6, 45].

Different forms of Aβ exist in different structural forms with different stabilities and pathological functions. Some of these forms are as follows:

1. Short oligomers with higher toxicity [46] and lower physical and mechanical stability

2. Protofibrils which are transient structures before fibril formation, are more toxic than mature fibrils [44].

3. Fibrils which have the lowest free-energy and thus the highest stability against physical perturbation [47]. They also have high thermal stability [48].

A recent study applied experimental approaches including ultraviolet resonance Raman spectroscopy and atomic force microscopy (AFM) in combination with molecular dynamics (MD) simulations and stress strain (SS) calculations to study structural and mechanical properties of amyloid fibrils such as secondary structure and Young's modulus [49]. Results suggested that these properties are size- and structure-dependent.

Another study suggests that Aβ aggregates in the form of fibrils or other self-assembled forms have a significant role in the progression of Alzheimer's disease (AD).

Fibrils formed by both Aβ (1-40) and Aβ (1-42) are polymorphic with variation in their molecular structures which depends on their growth condition. Moreover, the correlation between different Aβ polymorphs and AD phenotypes was investigated using solid state nuclear magnetic resonance (ssNMR)[50].

Toxicity

It is evident that nanomolar concentrations of Aβ is crucial for neural development and neurotransmission [43]. In fact, only high concentrations of Aβ is toxic. Therefore, there is a relationship between the concentration of Aβ and its toxicity. In normal cases, there is a steady state in which the rate of Aβ production and elimination are the same. If this state is perturbed, it leads to dysregulation of Aβ and plaque formation.

Some other studies suggest that specific structural forms of Aβ are able to induce toxicity. Aggregated peptides, soluble oligomers and insoluble Aβ assemblies are known to be the most toxic species among the others [43].

Oligomeric intermediates are formed in the process of fibril formation in solution. Results of a recent experiment on hen egg white lysozyme (HEWL) suggest that silica nanoparticles (SNPs) prevent the formation of these toxic intermediates by accelerating the fibrillation process [51]. The same study showed that the structure of fibrils change in the presence of silica. Fibrils formed near silica are mostly beta sheet rich structures while those formed in solution appears in the form of globular aggregates. The authors have also talked about the observation of a peak in the high-frequency region of FTIR spectrum which is the hallmark for anti-parallel beta sheets. They did their experiments at acidic and high temperature conditions in which HEWL has an unfolded structure. Therefore, they proposed that the aggregation process will become faster if the aggregation hot spots of HEWL are exposed to the solvent. To verify this, they characterized the hot spot regions of HEWL using the online server AGREESCAN and observed no acidic residue in the hot spot regions. Since at pH=2 (in which the experiment was done) the surface of silica nanoparticles are neutral and HEWL has a large positive charge, it was predicted that the binding of

HEWL on silica is mostly due to the hydrogen bonding between the silanol groups of silica and -COOH groups of the acidic residues of HEWL. Therefore, they predicted that the non-amyloidogenic parts of HEWL attach to silica nanoparticles and the amyloidogenic parts are exposed to the solvent facilitating the formation of ordered beta sheets.

1.3   Silica: an inorganic surface

Among different types of nanoparticles, silica (amorphous silicon dioxide, SiO_2) has gained much attention due to some specific features such as low toxicity, low cost and high biocompatibility [52]. For instance, silica nanoparticles (SNPs) have been recently found to be suitable candidates for protein removal from human serum samples at physiological pH [53]. The procedure is based mainly on the attractive interaction between serum proteins and SNP which results in the aggregations and precipitation of proteins and particles. This way, experimentalists can get clear results from nuclear magnetic resonance spectra and have a more accurate diagnosis based on the serum content.

Silica nanoparticles can affect the behavior of the nearby biomolecules in different ways depending on their size, curvature, surface charge, surface chemistry, and also the type of functional groups on their surface [54, 55, 56, 57]. In the specific case of peptide adsorption to SNPs, there are other factors that also determine binding strength as well as the prevalence of different binding modes. Surface hydrophobicity/hydrophilicity, peptide bulk concentration, and solution salt concentration and pH are known to be important factors in this respect [58]. For instance, a change in the environmental pH from acidic to neutral leads to a higher tendency of cationic peptides for binding to the silica surface. This is mostly due to an increase in the number of deprotonated silanol groups on the silica surface at neutral pH in comparison with the acidic environment. However, the scenario is completely different for hydrophobic negatively charged peptides. Electrostatic interactions at neutral pH result in a repulsion between the negatively charged peptides and silica surface. Therefore, negatively charged peptides previously attached to the silica nanoparticles

in an acidic environment could be easily detached from the surface at neutral pH [59].

A comparison between the effect of pH and ionic strength on binding of lysozyme to silica nanoparticles has been recently reported [60]. The results revealed that protein-silica binding was mostly affected by pH and not by the electrolyte concentration except in two specific cases, one near pH 5 and the other one near the protein isoelectric point. Similar effects have already been reported in experimental studies for DNA adsorption/desorption into/from silica surface by changing pH [61]. The effect of pH and ionic strength on multiphasic adsorption of DNA into silica nanoparticles has also been investigated [62]. It was observed that low pH and high ionic strength are good conditions for stronger binding. Moreover, the flexibility of DNA has been found to change during different phases of binding from an initially rigid into a viscoelastic conformation after some minutes which could be partly because of a decrease in the number of contacts after binding to the surface.

1.3.1 Adsorption of biomolecules on the silica surface and the main driving forces

The main reason for binding of peptide to the SNP has been a topic of interest in recent years. In an experimental study, binding coefficients of single amino acids to silica has been calculated for all 20 natural amino acids by Xie et al. [31]. According to their findings, both electrostatic and hydrophobic interactions play important roles in the adsorption of amino acids to surfaces. In a recent work, Patwardhan et al. proved both computationally and experimentally that a combination of electrostatic and non-electrostatic interactions are responsible for the binding of cationic and non-cationic peptides to the silica surface [63].

Experiments provide important characterization on the behavior of biomolecules at the silica surface; however, the molecular details are often missing. There have been several theoretical works studying the behavior of different types of biomolecules at the interface.

In 2007, Hassanali et al. developed a model (as an extension to the BKS and

SPC/E models) to describe the undissociated amorphous silica surface and obtained the model parameters using ab initio quantum chemical calculations. The calculated heat of immersion in water with this model was in good agreement with the corresponding experimental value [64].

In 2010, the same group extended this model by including the dissociated silanol groups [65]. The extended model characterizes the interaction of silica surface with water and sodium and chloride ions. The model was verified either with experimental measurements (such as the heat of immersion) or with ab initio results.

In 2015, the model was further developed for the general studies of biomolecules at the silica-water interface using ab initio quantum chemical data [1]. To this end, the interaction of specific molecules was investigated with a selection of groups on the silica surface. Figure 1-1 demonstrates these interactions. The selected surface groups include a variety of polar, charged, and hydrophobic groups. Among the probe molecules there are also nonpolar (methane), polar (methanol), charged (ammonium and acetate), and aromatic (benzene) groups.

a) methane–O$_X$ b) methane–O$_H$ c) methanol–O$_H$ d) methanol–O$_M$

e) ammonium–O$_H$ f) ammonium–O$_M$ g) acetate–O$_H$ h) benzene–O$_X$/O$_H$
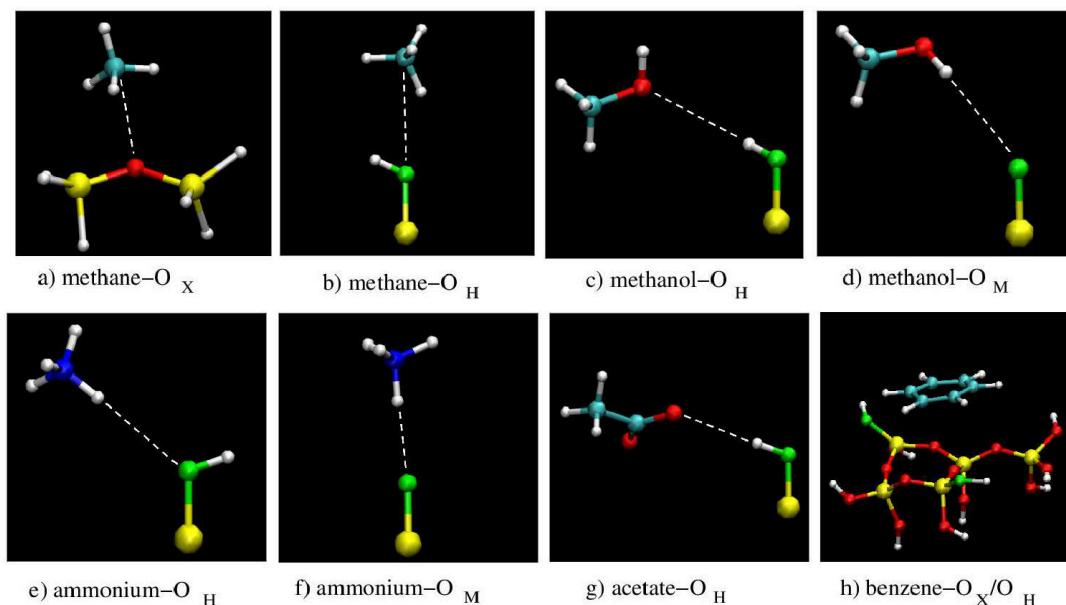
Figure 1-1: Different groups of silica interact with probe molecules. Interactions between (a) methane and oxygen atom of the siloxane group (Si-O-Si), (b) methane and oxygen atom of the silanol group (Si-O-H), (c) methanol and oxygen atom of the silanol group, (d) methanol and oxygen atom of the dissociated silanol group (Si-O$^-$), (e) ammonium and oxygen atom of the silanol group, (f) ammonium and oxygen atom of the dissociated silanol group (Si-O$^-$), (g) acetate and oxygen atom of the silanol group, and (h) benzene and oxygen atom of the silanol/dissociated silanol group. This figure is adopted from reference [1].

To understand why negatively charged DNA binds to the negatively charged silica surface, the same group [1] investigated the mechanism of DNA binding to silica using the force field developed previously by themselves [64, 65]. Two main mechanisms were reported for DNA binding to silica: attraction between phosphate group in DNA and silanol groups on the silica surface; hydrophobic interaction between DNA bases and the hydrophobic regions of silica where no silanol group is found (see Figure 1-2). In comparison with the bulk density of water and the density of water around silanol groups, a lower water density was previously reported above these hydrophobic patches (Figure 1-2b)[64].
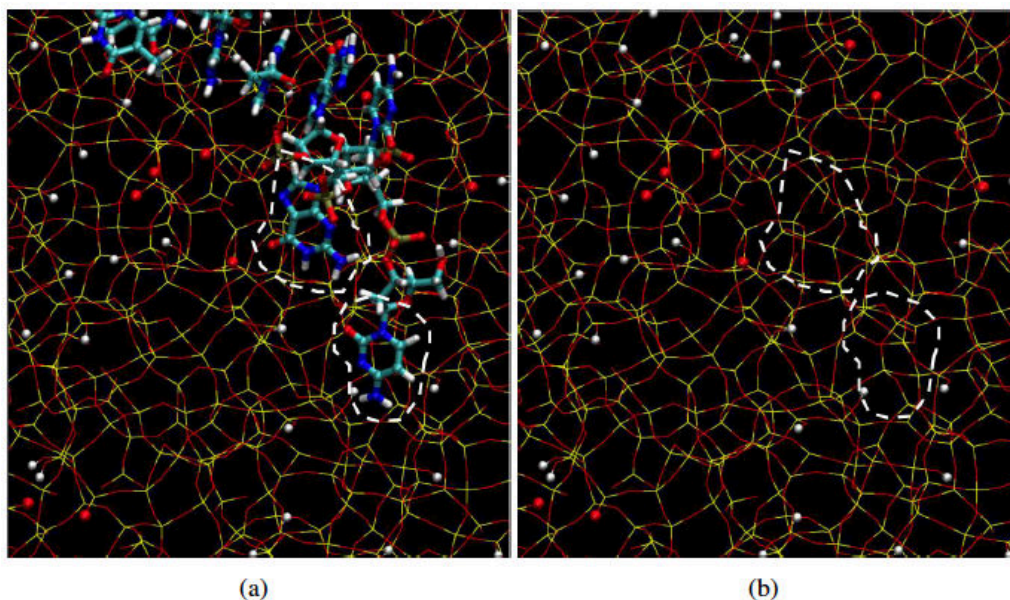
Figure 1-2: (a) Bases in the DNA interact with the hydrophobic regions on the silica surface. (b) Hydrophobic patches of the silica surface. This figure is adopted from reference [1].

The same study has also reported that the binding of single stranded DNA (ss-DNA) is stronger than double stranded DNA (dsDNA) which is mostly due to the fact that ssDNA has unpaired bases, more flexibility, and less charge in comparison with dsDNA.

In a more recent study [66], Shi et al. investigated the binding of two different tripeptides (KWK and EWE) to the silica surface. It is interesting that not only the positively charged peptide (KWK) but also the negatively charged peptide (EWE) binds to the negatively charged silica surface. This explains the important role of several binding mechanisms (specifically the hydrophobic interaction between the indole groups and hydrophobic regions of the surface) other than the electrostatic interactions. In addition, there were cases in which the negatively charged carboxyl groups bind to the silanol hydrogens. All of these binding mechanisms suggest that a variety of binding modes are involved in the binding of biomolecules to the silica surface.

To model the interactions at the silica-water interfaces, another force field was developed in 2014 by Emami et al. [67]. Some of the important features of this force

field are: more accurate interfacial properties in comparison with experiment, full mobility of atoms, match between computed and measured values of density of states, agreement of computed and measured immersion energy of surfaces in water, agreement of the amount of dissociated cations and the value of ζ-potential as a function of pH and particle size, and compatibility with the major biomolecular and organic force fields such as AMBER, CHARMM, INTERFACE, and COMPASS. In an accompanying paper, they investigated the effect of pH and size of silica nanoparticles on peptide adsorption for three different peptides with negative, positive, and zero charges [68]. They obtained the strength of peptide adsorption and selective binding of different residues using molecular dynamics simulations.

According to their results, because of the fewer SiO^- groups on the silica surface at low pH, the positively charged peptides are adsorbed to the surface mostly through their polar and hydrophobic residues. Moreover, the peptide took a flat-on conformation. The authors referred to the role of hydrogen bonded network between water molecules in driving the hydrophobic residues to the silica surface since these residues disrupts the liquid water network.

On the other hand, the higher adsorption of the positively charged peptides on the more negatively charged surfaces at higher pH was mainly through the N-terminal of the peptide. In this case, the peptide took an anchors-like conformation.

However, the story was reported to be completely different for the negatively charged peptides. These peptides had lower affinity toward the more ionized silica surface at higher pH while they adsorbed more and through different residues on the less-ionized silica surface at lower pH.

Authors of the same study concluded that hydrophobic interactions are more abundant at low surface ionization and separation from the aqueous phase is the main driving force for them to come to the surface. However, electrostatic interactions were reported to be stronger than hydrophobic interactions. Strength of interactions were assessed through the calculation of free energies and binding energies. For short peptides (consisted of less than 10 residues), the values of both energies were reported to be almost the same since the entropic contribution is negligible. The reason is that

when a peptide is adsorbed to a surface, its mobility decreases which results in a reduction in entropy. Instead, lots of water molecules are detached from the surface to give their places to the peptide. Therefore, they increase the system entropy and compensate for the reduction in entropy caused by the adsorption of peptide.

1.4 The cell membrane: an organic surface

Plasma membrane, the fundamental component in all cells, separates the inner side of the cell from its outer environment. Components of the cell membrane (mainly lipids and proteins) are stabilized by noncovalent forces, giving the membrane a non-rigid (deformable) feature [2]. The cell membrane regulates the cell metabolism by controlling the transport of materials between the intracellular and the extracellular space. It also plays an important role in controlling the exchange of heat between inner and outer parts of a cell. Moreover, membrane proteins (receptors) play a significant role in cell-cell and cell-matrix recognition.

1.4.1 Membrane composition

It is evident that the properties of the membrane depend highly on the membrane composition [69]. For instance, rigidity which is a structural property of the membrane depends on the concentration of cholesterol.

The cell membrane is mainly composed of amphipathic lipids (i.e. lipids with a hydrophilic and a hydrophobic end), proteins, and carbohydrates [70]. However, the concentration of each constituent is different in different types of cells. Membrane lipids are divided to three main categories: **phospholipids**, **glycolipids**, and **sterols**.

Phospholipids

In the majority of cell types, phospholipids are the most abundant lipids [71]. They constitute more than half of the lipids in the membrane. Phospholipids are made of a glycerol molecule, two uncharged nonpolar tails (fatty acids), and a negatively-charged phosphate group, which makes the polar head. Chemical structure of a

phospholipid molecule called phosphatidylcholine is represented in Figure 1-3. In the aqueous environment, phospholipids form micells. It is mainly because of the tendency of their polar heads to water, whereas their hydrophobic tails escape away from polar water molecules.
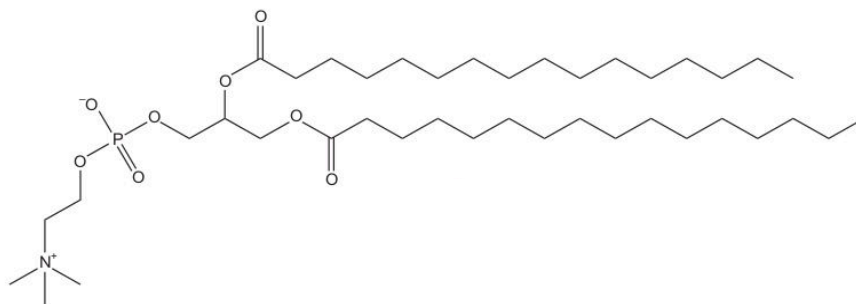
Figure 1-3: Chemical structure of phosphatidylcholine. The figure is adopted from reference [2].

Four main types of phospholipids found in the membrane of animal cells are phosphatidylcholine, phosphatidylethanolamine, phosphatidylserine, and sphingomyelin. These phospholipids are unevenly distributed in the two leaflets of the membrane. As it is illustrated in Figure 1-4, phosphatidylethanolamine and phosphatidylserine are found mainly in the inner leaflet of the bilayer while phosphatidylcholine and sphingomyelin are the most predominant lipids in the outer leaflet [3, 72]. Cholesterol is found in both leaflets.
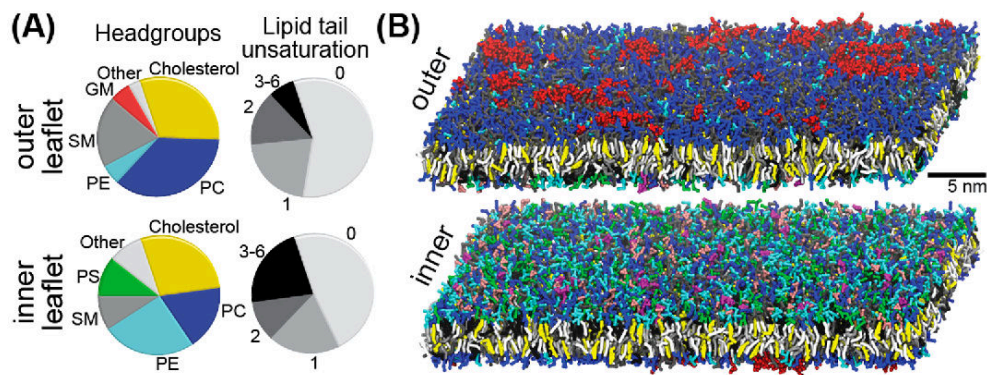
Figure 1-4: Asymmetric distribution of lipids in the two membrane leaflets. GM, SM, PE, PS, and PC stand for ganglioside lipids, sphingomelin, phosphatidylethanolamine, phosphatidylserine, and phosphatidylcholine, respectively. The figure is adopted from reference [3].

Sterols

The most common sterol in animal cells is cholesterol. Similar to most of the lipids in biological membranes, cholesterol has an amphipathic nature (i.e. it is consisted of a hydrophobic and a hydrophilic group). As it is illustrated in Figure 1-5, the hydrophilic (polar) head of cholesterol is a hydroxyl group connected to a planar body composed of four fused rings. A saturated hydrocarbon chain makes the short hydrophobic tail of cholesterol.

Concentration of cholesterol is normally between 10 and 45 molar percentage of total lipids in the membrane [73].
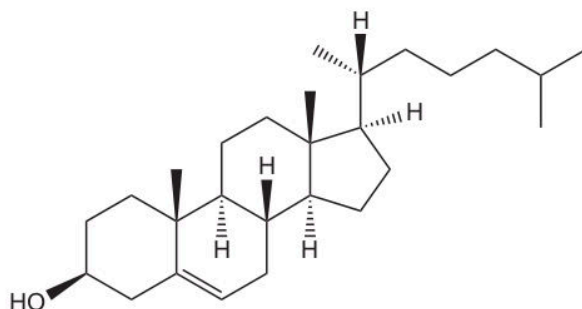
Figure 1-5: Chemical structure of cholesterol molecule. The figure is adopted from reference [2].

Membrane proteins

Proteins are the other important building blocks of the cell membrane doing a variety of tasks. Membrane proteins are divided into two main categories: integral membrane proteins (embedded in the membrane) and peripheral membrane proteins (located on the membrane surface) [2, 71, 74]. Integral membrane proteins interact with membrane via their transmembrane domain, which mostly consists of hydrophobic amino acids.

Membrane proteins interact with the membrane in different ways. They can cause disorders in the membrane and can be affected by the physical state of the lipid bilayer. Membrane thickness can also affect the structure of membrane proteins [2].

Amyloid Precursor Protein (APP) as an integral membrane protein

Amyloid precursor protein (APP) is a well-known example of integral membrane proteins [75, 76]. More than half of the mutations in APP associated with Alzheimer's disease occur in the transmembrane domain of this protein [77].

1.4.2   Effects of cholesterol on the membrane

Cholesterol decreases the permeability of the plasma membrane, reduces the conformational flexibility of membrane proteins, and disturbs the phase transition of saturated phospholipids in the membrane. Several studies report the condensation effect which is a structural change in the membrane upon the addition of cholesterol molecules [78, 79]. Condensation means that the area per lipid molecule decreases to less than the weighted average of areas of pure components [79]. The reason is that cholesterol interacts with lipids via hydrogen bonding and can fill the voids between lipid molecules [80]. The higher the percentage of cholesterol, the smaller the area per lipid molecule. Furthermore, cholesterol affects the phase behavior of phospholipid membranes in a concentration-dependent manner [81]. In cholesterol concentrations less than 25%, the membrane is always in one of the liquid-disordered or solid-ordered phases, depending on the temperature. However, in higher levels of cholesterol, the membrane can be found only in one phase called liquid-ordered phase. It is also ev-

ident that the effect of cholesterol on the structural order of the membrane depends on the temperature. Above the phase transition temperature that lipids are in the liquid phase, the addition of cholesterol to the membrane increases the structural order while below this temperature lipids are in the gel phase and the addition of cholesterol disrupts the order [81].

1.4.3   Asymmetry in the membrane

Two leaflets of the membrane can have different composition and therefore, different properties [2]. In the human erythrocyte, for instance, despite an exchange mechanism (called flip-flop) between the two leaflets, the differences in the lipid compositions in the two membrane leaflets are maintained. In some other types of cells, the distribution of cholesterol is different in the inner and outer leaflets of the membrane. In red cells, for example, the percentage of cholesterol in the outer leaflet is 51%, and in the inner leaflet is 49% [82]. In colorectal cells, cholesterol constitutes about 2.77% of the inner leaflet and 33.3 % of the outer leaflet in healthy cells. In other words, in the membrane of healthy colorectal cells, the ratio of $[CHL]_o$ to $[CHL]_i$ is 12, while it decreases to 5.5 in the membrane of cancerous colorectal cells [73].

1.5 Temperature and its importance in living systems

The effect of temperature on chemical reactions and physiological processes is well known. living objects behave differently at low temperatures. Change in the fluidity of cell membrane or DNA supercoiling are some examples. Moreover, most of the biological rates (such as metabolic rate) depend on temperature. For instance, cilial and flagellar movement rates are temperature dependent since the viscosity of the environment in which cilia and flagella move changes with temperature. Figure 1-6 is a graphical representation of the model developed by Humphries [4] to demonstrate the relationship between temperature and biological rate connected to flagellar movements.
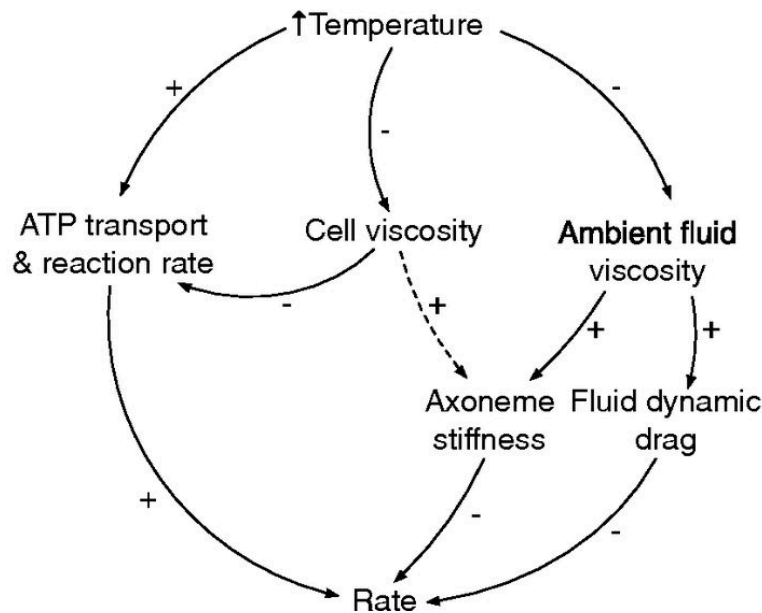
Figure 1-6: Graphical representation of Humphries model. Increase in temperature leads to an increase in reaction rates but also a decrease in the cellular and fluid viscosity. This figure is adopted from reference [4].

In addition, Figure 1-7 demonstrates how biological reaction rates change with temperature.
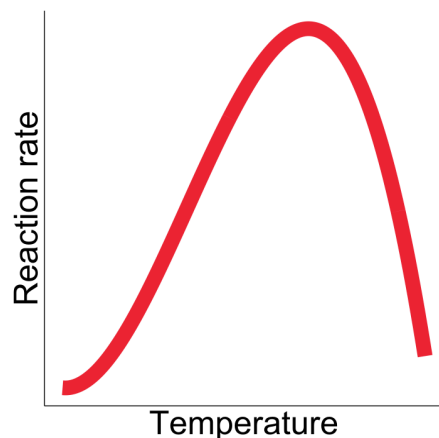
Figure 1-7: Biological reaction rates increase with temperature up to a maximum. This figure is adopted from reference [5].

In one of the previous studies in our group, the effect of a slight change in temperature on the amyloid beta formation has been investigated in the absence and presence of two types of nanoparticles (polystyrene and silica) in the temperature range from 35 to 42°C [6]. Molecular dynamics simulations, as well as experiments, have been performed to investigate the effect of temperature on the exposure of the amyloidogenic part of amyloid beta (residues 17-24). The results revealed more exposure of the sequence 17-24 in the amyloid backbone at higher temperatures. Then, Thioflavin T assay was used to study the effect of temperature on the amyloid fibrillation in the presence of nanoparticles. Figure 1-8 represents the obtained results. According to this figure, even in the absence of nanoparticles increasing the temperature affects the lag phase in the amyloid fibrillation and makes it shorter. An enhanced effect is observed in the presence of silica nanoparticles. In the presence of polystyrene, however, the story is different since it has an inhibitory effect.

It is interesting that a slight change in temperature enhances the effect of both types of nanoparticles on the fibrillation process, whether this effect is inhibition or acceleration.
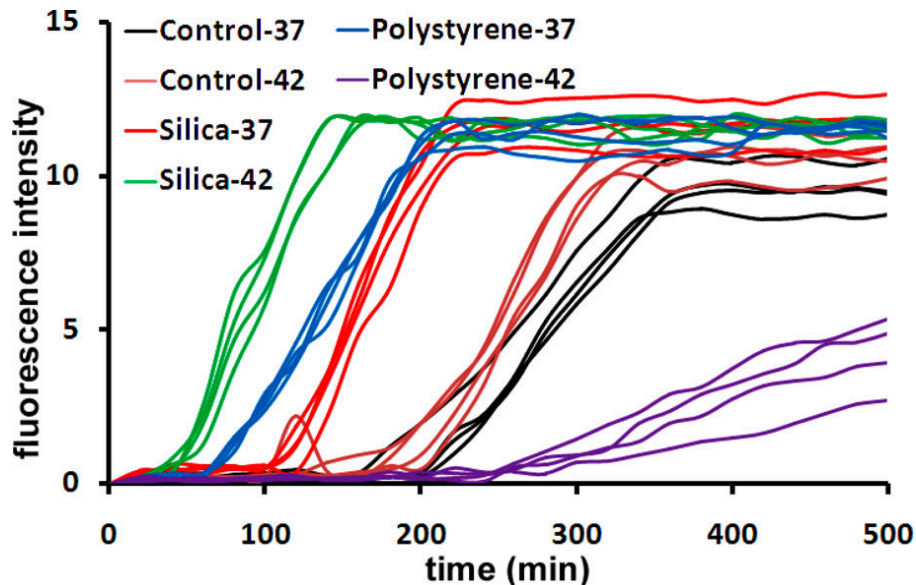
Figure 1-8: Effect of slight temperature change on the acceleratory or inhibitory effect of different nanoparticles on the amyloid fibrillation. This figure is adopted from reference [6].

1.5.1 Heat transport

Conduction, convection, and radiation are different means of heat transport through materials. However, at length scales smaller than the energy carriers wavelength or at time scales comparable with the relaxation time of the carrier the conventional heat transport theory is not valid. Both heat and mass transport at the scale of nanometer are dominated by the large surface-to-volume ratio. At the nanoscale, heat transport via convection requires temperature differences of the order of 10^{17} K [83]. Energy exchange through radiation also follows different rules at the nanoscale in comparison with scales larger than the thermal wavelength [84].

The target of this study is to study the contribution of conduction in heat transfer at the nanoscale.

Heat transfer in cells

Thermoregulation is done through the variation of blood flow to the body. It is recognized that blood plays different roles in the thermal balance of the body. Firstly, it can act as a source to make the body warm or as a sink to cool the body down in

hyperthermia conditions. Secondly, in case of thermal stress or exercise the cardiac output increases resulting in an increase in blood flow and an enhanced heat loss via the skin by sweating [85].

Besides, heat transport in tissues is of great importance in diagnostics and therapeutic applications. Therefore, several methods have been studied to model bioheat transfer in tissues. Some of the well-known methods are Fourier's law as well as several modifications of it such as Maxwell-Cattaneo [86]. Other examples of bioheat transfer models for blood flow are Pennes and Weinbaum-Jiji bioheat equations [85].

It is evident that the thermal properties of the cell change in pathological conditions [87]. The thermal conductivity of two types of cells has been measured experimentally. Results suggest that irrespective of the cell type, the thermal conductivity of the dead cells were 6-13% larger than that of the live cells.

In another study, thermal conductivity and diffusivity of two types of cancer cells (cervical and breast cancer) have been investigated and a 5% increase has been reported in the thermal conductivity within the cancer cell types [88].

A more recent study found statistically meaningful differences between the thermal conductivity values of normal and diseased cells [89]. According to the same study, the thermal conductivity of diseased cells changes with the progression of the disease. Another study suggests that the thermal conductivity measurement is an early-stage diagnosis for malignant melanoma [90]. Based on the results of that study, the thermal conductivity of malignant skin lesions was different (lower) than that of healthy cells and the difference was statistically significant. Furthermore, a correlation between tumor progression and the lesion thermal conductivity was reported.

Thermal conductivity of the cell membrane

Thermal conductivity, which is a structure-dependent property of the cell membrane, has been the topic of interest in recent years due to its potential diagnostic applications. Thermal conductivity measurements of the membrane are of great importance for engineering new materials, such as nanoparticles, to be used in modern treatment

28

techniques. For instance, in a selective treatment method called photothermal cancer therapy, metal nanoparticles inside the tissue generate heat after being radiated by an external source. The generated heat then transports to the nearby cells through the cell membrane [91]. To tune the parameters (such as the power) of the radiative source properly and to achieve high efficiency, one should have an understanding of the thermal conductance and resistance of the cell membranes.

To the best of our knowledge, an experimental measurement of thermal conductivity of the cell membrane was not available until 2019. Only in recent years, luminescence thermometry was utilized for this purpose [7]. In this approach, $LiYF_4{:}Er_3^+/Yb_3^+$ upconverting nanoparticles (UCNPs) were used as heat sources. UCNPs coated with lipid bilayers immersed in water which is served as a heat sink. Simultaneously, the temperature of the surrounding water was measured using an immersed thermocouple. The difference between the temperatures of nanoparticles and environmental fluid was then used to calculate the thermal conductivity of the intermediate lipid bilayers. Figure 1-9 illustrates this experiment.

According to the results of the same study (Figure 1-10), the thermal conductivity of the lipid bilayer as a function of laser power density can be described in two different regimes. In the first regime, up to a specific value of power density, the thermal conductivity of the lipid bilayer decreases, and the difference between the temperature of UCNPs and the immersed thermocouple $(T_p - T_f)$ increases. In this regime, the membrane acts as a thermal barrier. In the second regime, the temperature difference between nanoparticles and fluid decreases, and the conductivity of the lipid bilayer increases dramatically.
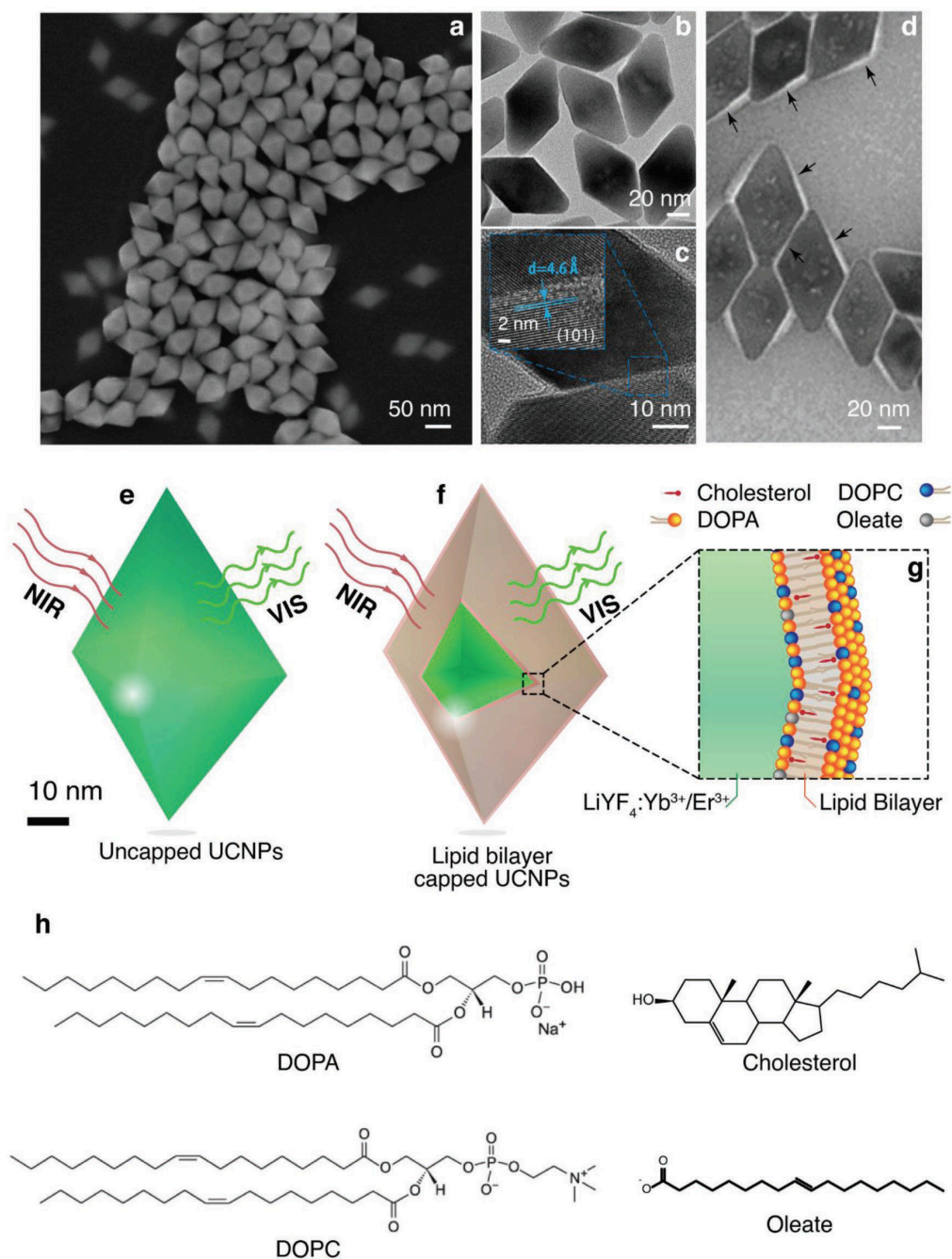
Figure 1-9: (a) SEM and (b) TEM images of UCNPs coated with Oleates. (c) and (d) UCNPs capped with lipid bilayers. (e) Uncapped and (f) lipid bilayer capped UCNPs. (g) The composition of lipid bilayer coating. (h) Structural formulas of the components of lipid bilayer coating. This figure is adopted from reference [7].
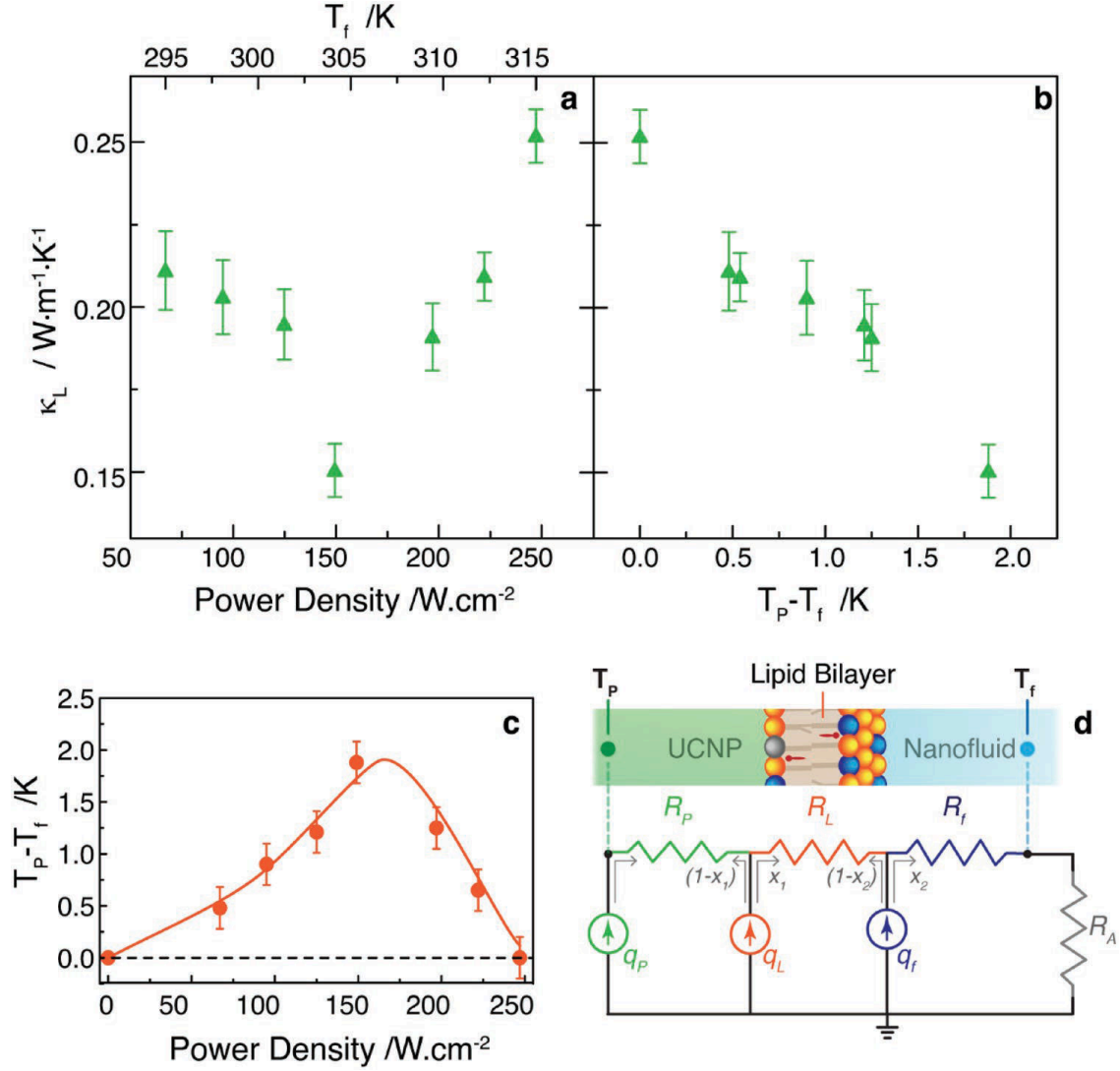
Figure 1-10: Lipid bilayer thermal conductivity as a function of (a) laser power density and (b) temperature difference between UCNPs and immersed thermocouple. (c) The temperature difference between UCNPs and immersed thermocouple obtained from the calculation (line) and experiment (dots). (d) A one-dimensional model for bilayer capped UCNPs. This figure is adopted from reference [7].

Although there are only a few experimental measurements of the membrane thermal conductivity available to date, several computational studies have been developed and utilized for thermal conductivity calculations of lipid bilayers.

Müller-Plathe et al. performed a series of all-atom simulations to study the heat transport across a DPPC membrane [8] using the RNEMD algorithm developed by

them previously [25]. Figure 1-11 shows a schematic representation of their simulation box. They focused on the local thermal conductivity profile of the membrane and proposed that the tail-tail interface between the two leaflets strongly affects the value of the thermal conductivity of the membrane. They obtained the local thermal conductivity profile of the membrane as is illustrated in Figure 1-12. According to this figure, thermal conductivity is minimum in the area between the two membrane leaflets where the alkyl chains meet. A possible reason for such a high thermal resistance could be the lack of a covalent bond in the area between the two membrane leaflets [92]. An asymmetry in thermal conductivity is also reported in the same paper. Later, other studies supported the idea of asymmetric heat conductance through lipid membranes as well as a discontinuity in thermal conductivity profile where lipid tails touch [93, 94]. Furthermore, different thermal conductivity coefficients in normal and lateral directions of a bilayer have been reported [93].
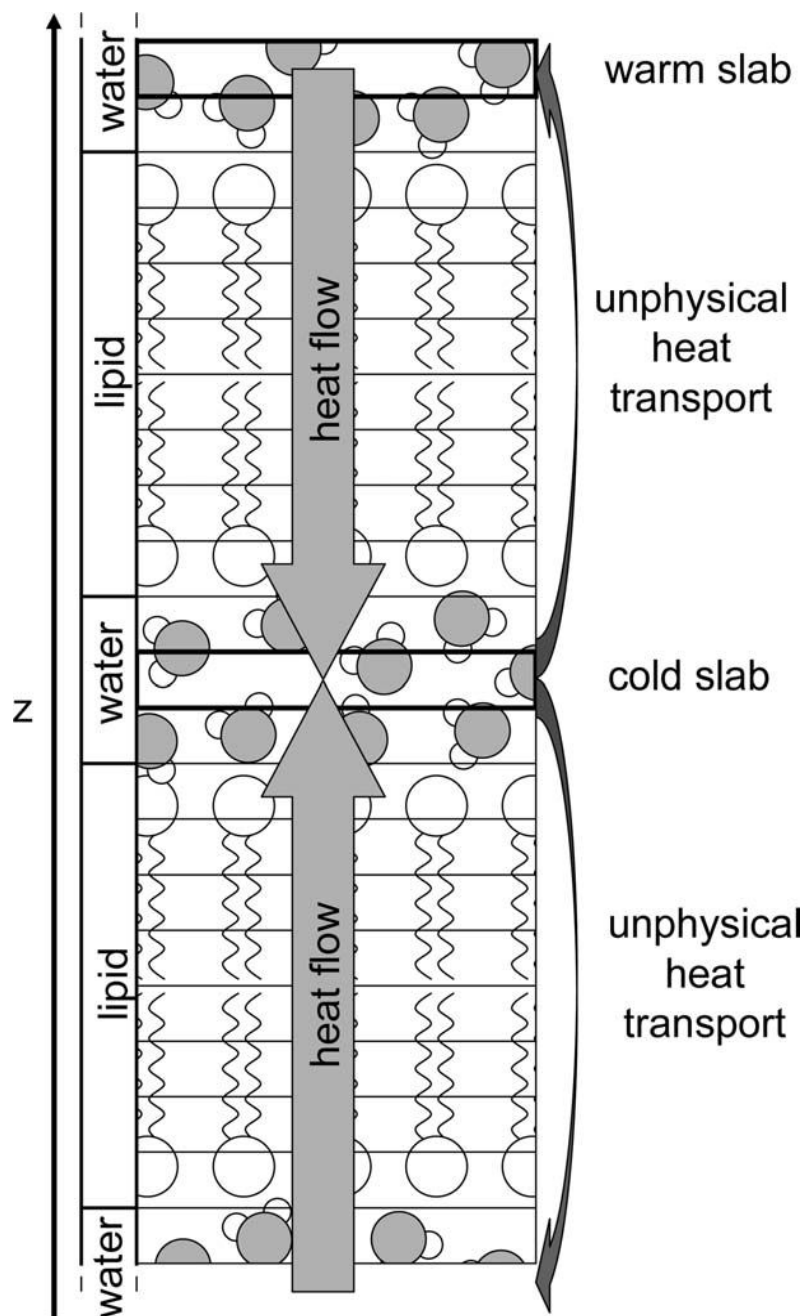
Figure 1-11: To implement the Müller-Plathe RNEMD algorithm, simulation box is divided into several layers. This figure is adopted from reference [8].
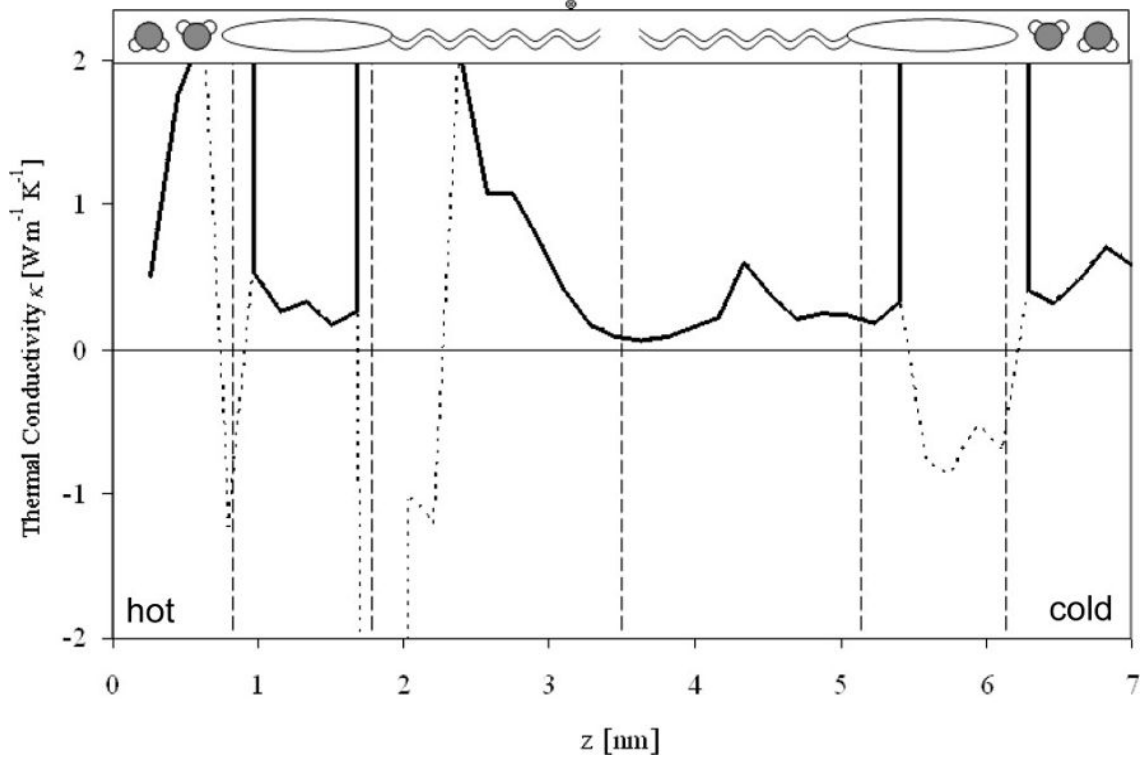
Figure 1-12: Local thermal conductivity profile of a DPPC model membrane across z axis obtained by Müller-Plathe et al. The minimum value of thermal conductivity is observed in the area between the two leaflets in the lipid bilayer. This figure is adopted from reference [8].

1.5.2 Thermal rectification

Rectification occurs when thermal transport depends on the sign of temperature gradient in a specific direction. One of the main mechanisms underlying this phenomenon is the roughness of the surface at contacts. Another mechanism for thermal conductivity rectification is the usage of different materials at a contact. The reason is that thermal conductivity depends on temperature and this dependence varies between different materials.

Thermal rectifiers have several potential applications in various fields. For instance, a thermal rectifier transporting heat in one direction while insulating the compartments in the other direction is a perfect candidate for cooling purposes in nanoelectronics.

Rectification has several definitions in different contexts. For instance, Eq. 1.16

34

represents a definition provided for solid state rectifiers [95, 96].

$$\epsilon = \frac{k^+ - k^-}{k^+ + k^-} \tag{1.16}$$

where k^+ and k^- are the thermal conductivity in the forward and backward directions, respectively. In this definition, thermal conductivity is assumed to be higher in the forward direction in comparison with the backward direction (i.e., k^+ is assumed to be greater than k^-). This way, an ideal rectifier is the one with a maximum difference between the forward and backward thermal conductivities (i.e., zero conduction in one direction and infinite conductivity in the opposite direction) and there will be no rectification if the thermal conductivity values in forward and backward directions are the same

If the temperature gradient is the same in the forward and backward thermal conductivity measurements, the thermal rectification can also be defined as the ratio of the difference in heat fluxes over the sum of heat fluxes.

Eq. 1.17 represents another definition of thermal rectification.

$$\epsilon = \frac{k^+}{k^-} \tag{1.17}$$

For thermal diodes, [97], thermal conductivity is defined as a non-negative value according to Eq. 1.18.

$$\epsilon = \frac{k^+}{k^-} - 1 \tag{1.18}$$

In this study, we define thermal rectification as represented in Eq. 1.18.

Thermal conductivity was first observed in 1936 at the interface of Copper/Cuprous Oxide [98]. A higher thermal and electrical conductivity was reported in the direction from metal to oxide. Heat is transported in metal and oxide through electrons and phonons, respectively. At the interface, electrons are scattered with phonons and transmitted into the oxide or reflected back into the metal. This results in resistance and a jump in the temperature at the interface. Since the rate of energy transfer from electrons to phonons is different from the rate of energy transfer from phonons

to electrons, thermal rectification can happen.

Thermal energy transport at the interfaces consisting of dissimilar materials could also be rectified. The reason is the change in contact area which leads to the change in contact resistance.

Different properties of the materials that are in contact with each other at the interfaces is another proposed mechanism for thermal rectification. The directional effect, in this case, is due to the thermal strain of the material which has a lower thermal conductivity.

Thermal rectification also happens at the interfaces between two metals if they have different work functions. Another mechanism for thermal rectification in bulk is when the thermal conductivities of two materials forming an interface depends differently on temperature. It can cause an asymmetry which results in a directional effect. However, the reason for thermal rectification in nanostructures is different. Although there have been few experiments at the nanoscale, a large number of theoretical and computational studies exist in this respect. The proposed molecular mechanisms of thermal rectification in nanostructures are non-uniform mass distribution and asymmetric geometry of nanostructures at interfaces.

We explain each of these mechanisms briefly in the following section.

According to the results of an experimental study on the carbon and boron nitride nanotubes [95], the non-uniform mass distribution along the nanotubes caused a directional effect along the length of nanotubes. The rectification factors obtained up to a value of 0.01 and 0.034 for carbon and boron nitride nanotubes, respectively. The higher thermal conductivity was reported in the direction of high- to low-density. The reason for rectification in materials that are not homogenous was claimed to be associated with the collision of solitons which are particle-like objects.

In a previous computational study, nonequilibrium molecular dynamics simulations have been performed on non-uniformly mass-distributed carbon nanotubes using the Müller-Plathe algorithm [14]. According to the results, the rectification factors were in a range between 0.015 and 0.074 with higher conduction in the direction of low- to high-density which is in contrast with the previous findings by Chang et. al.

[95].

Asymmetry in the geometry of nanostructures is another mechanism for thermal rectification at the nanoscale. The thermal conductivity of nanowires has been studied theoretically and a thermal rectification of 0.43 has been found in the structures with asymmetric geometry (such as an asymmetric sawtooth) with a smooth boundary in one direction and a rough boundary in the other direction. A thermal rectification of 0.64 has also been found in asymmetric graphene ribbons using molecular dynamics simulations.

Simulations of Carbon nanohorns and nanocones showed a directional preference in the thermal conductivity along the nanostructure with a higher conductivity in the direction of decreasing diameter. Another study reported that the rectifying effect of nanocones increases with an increased temperature gradient up to a temperature gradient of 0.7 normalized by the average temperature of the system. The maximum value of rectification was reported to be 0.44.

Thermal rectification in membranes

Previous studies have reported an anisotropic heat transfer along and across the membranes [92, 93]. Other studies have found that the thermal conductivity of the membrane changes at different temperatures and temperature gradients across the membrane as well. Some proposed that lipids with unlike thermal conductivities can be utilized for building thermal diodes. The use of asymmetric membranes as thermal rectifiers in microelectronics can be advantageous in several ways. First, lipids are bio-compatible materials. Second, their transition temperature can be tuned. Third, they are able to self-assemble. Therefore, there is a high interest in a better understanding of the thermal properties (especially thermal rectification) of lipid membranes.

Thermal rectification in asymmetric membranes of archaeal was investigated by Youssefian et al. [9]. They applied molecular dynamics simulations to find the phase transition temperature, thermal conductivity, and rectification in three different types of archaeal lipids with the same head group but different tail structures (with and without cyclopentane rings). The area per lipid molecule was considered as a measure of the compactness of lipid molecules. According to the results of the same study, cyclopentane rings are responsible for the high level of molecular packing and the increase in the thermal conductivity of the membrane. A graphical representation of their method is provided in Figure 1-13.

The obtained thermal rectification factors of archaeal membranes (using the third definition of rectification provided in Eq. 1.18) were much lower than the rectification factors obtained in other studies for carbon nanotubes. The authors related the results to the smaller size of membranes and the lower temperature gradient across the membranes. A schematic representation of the thermal rectification model for the membrane is provided in Figure 1-14.
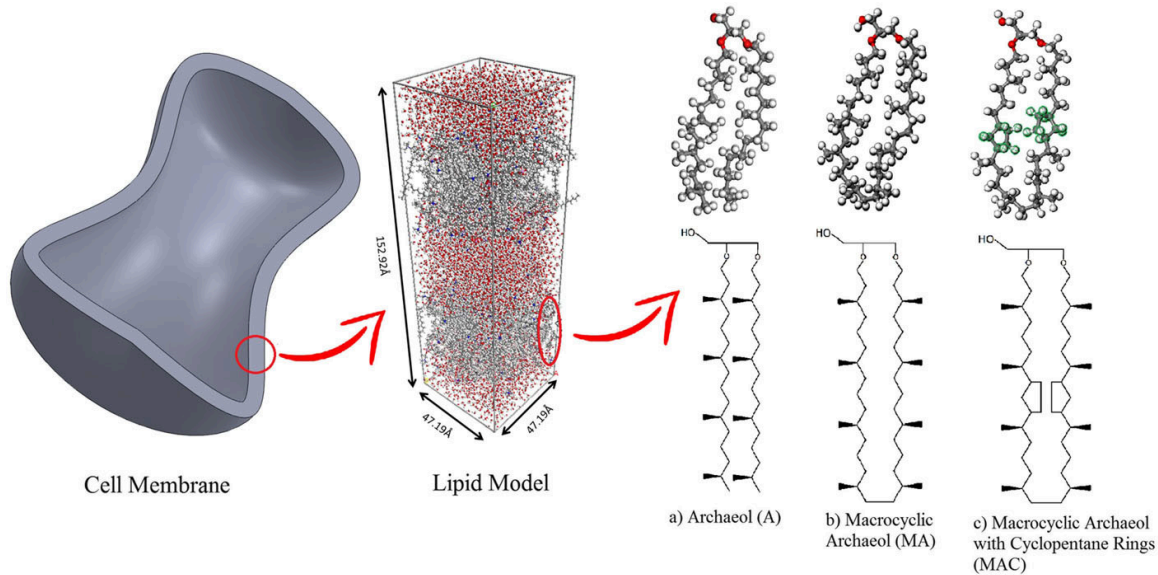
Figure 1-13: A graphical representation of the simulation setup used by Youssefian et al. to study the thermal conductivity of three different archaeal membranes. This figure is adopted from reference [9].
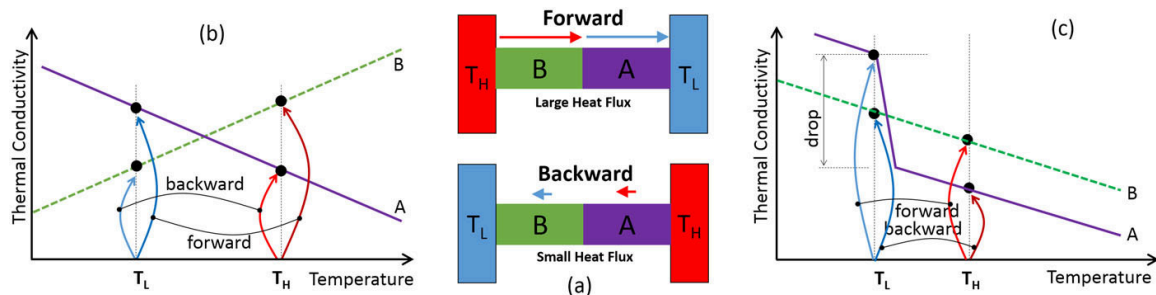
Figure 1-14: (a) A schematic representation of a thermal rectifier which is made of two dissimilar materials A and B. (b) A case in which the thermal conductivity of material A decreases while that of B increases as a function of temperature. (c) A case in which thermal conductivities of material A and B decreases as the temperature increases. Both conditions illustrated in (b) and (c) can result in thermal rectification in lipid membranes. This figure is adopted from reference [9].

They also found that the structure and the level of molecular packing in the archaeal membranes affect the phase transition temperature and thermal conductivity of archaeal membranes. Variation in the thermal conductivity coefficients was observed at different temperatures as well.

Chapter 2

Interaction between amyloid protein and the cell membrane

2.1 Introduction

In this study, we take a computational approach to investigate the thermal conductivity of the cell membranes with different compositions: at different levels of cholesterol and in the presence of APP. The motivation behind this is, on one hand, the dependence of thermal conductivity on the structure, and on the other hand, the relation between the level of cholesterol in the membrane and the membrane structure [79, 81]. To have an understanding of thermal transport in membranes with the ratio $[CHL]_o/[CHL]_i \neq 1$, we extend our study to a model membrane with a ratio of $[CHL]_o/[CHL]_i = 12$, such as the one for normal colorectal cells. The idea behind this comes from a recent investigation on thermal conductivity and rectification of asymmetric archaeal membrane [9].

Results of a previous study suggest that a slight change in temperature affects the interaction of the amyloid protein with hydrophobic/hydrophilic surfaces [34]. Considering the sensitivity of this protein to the temperature, many questions arise about the reaction of this protein to a temperature gradient and how the local temperature profile (and therefore thermal conductivity) can be affected by this protein. For the second part, we study a model DPPC membrane containing the trans-membrane part of APP. Besides, we consider another DPPC membrane with a horizontally laid APP on its surface. For these models, we obtain the rectification factor, which is a measure

of the difference between the thermal conductivity coefficients when heat flows in two opposite directions through the membrane.

2.2 Methods

2.2.1 Building a membrane/membrane-protein model

A protein-membrane system can be built in different ways. One method is to position the protein and lipid molecules randomly in the simulation box and minimize the system. It is evident that this system self assembles into a lipid bilayer with the protein aligned inside it. However, this is a lengthy process, specially for large systems. Another approach is to insert the protein into a pre-equilibrated membrane. For the insertion of proteins in the membrane, important points must be taken into consideration including the orientation of protein in membrane and the stability of the final structure.

Orientation of proteins in membrane

Precise positioning of proteins in the lipid bilayer is so important because it determines the biological activity, intermolecular interactions, stability and folding of membrane-protein complexes [99]. Because of the limited experimental data provided by methods such as X-ray scattering, NMR or infrared spectroscopy, spin-labeling and many others, some attempts have been made to find the right positioning of proteins computationally. Two of these methods which are frequetly used for membrane alignment and protein insertion are LAMBADA and InflateGRO2 [100]. Moreover, there are several databases such as OPM provideing the user with the correct alignment of the protein in membrane [99].

Online membrane builders

There are several databases and online servers providing atomistic/coarse-grained models that can be used to prepare initial structure of any type of membrane (homogeneous and heterogeneous). These builders also provide the option to insert

proteins into membranes for protein-membrane simulations [101]. Two examples are CHARMM-GUI membrane builder [102] and MemBuilder II.

Building the simulation box

Here, we use atomistic models of DPPC lipid bilayer with different levels of cholesterol (Figure 2-2). Each of the inner and outer leaflets of the membranes contains 36 lipid molecules some of which are cholesterol molecules corresponding to the given concentrations (0%, 5%, 11%, and 50%). It should be mentioned that the concentration of cholesterol in the inner and outer membrane leaflets are the same in all of these models. Although the thermal conductivity coefficient of the cholesterol-free DPPC membrane is reported in the previous computational studies [8, 103], we repeat it here not only to validate our model but also to have a reference value for the evaluation of the thermal conductivity of the cholesterol-contained membranes.

As the initial step for all the simulations, the pre-equilibrated structures of lipid bilayers are obtained from the CHARMM-GUI membrane builder [102].

The equilibration of large structures such as membranes requires extensive simulation time and resources. Therefore, to get advantage of the pre-equilibrated membrane structures we used CHARMM-GUI membrane builder which utilizes the CHARMM36 force field parameters. Output files produced by the CHARMM-GUI apply to a variety of molecular dynamics simulation packages. Here, we use the LAMMPS molecular dynamics package [104] for all simulations. Interactions between lipid-lipid, lipid-protein, and lipid-water molecules are treated using the CHARMM36 force field [105, 106], and the TIP3P [107] model is used to model water. In simulation, different water models yield slightly different physical properties and non of the water models can perfectly reproduce all physical properties regarding the experimentally obtained values. Thermal conductivity of water was obtained with different classical water models previously [108]. The results revealed that SPC, SPC/E, TIP3P, and TIP4P water models yield thermal conductivity values of 0.88 ± 0.020 W m^{-1} K^{-1}, 0.93 ± 0.016 W m^{-1} K^{-1}, 0.88 ± 0.019 W m^{-1} K^{-1}, and 0.82 ± 0.015 W m^{-1} K^{-1}, respectively. However, the thermal conductivity value of 0.68 ± 0.007 W m^{-1} K^{-1} as-

sociated with TIP5P model is the closest one to the reported experimental value of $0.61 \text{ W m}^{-1} \text{ K}^{-1}$.

To find the thermal conductivity and rectification of the membranes decorated with the amyloid precursor protein, initial structures of the trans-membrane part of the APP (PDB code: 2llm [77]) and part of the APP that lies on the membrane surface (PDB code: 2lp1 [109]) are obtained from protein data bank [110, 111] and used as the input to the OPM database [112] which provides the orientation of proteins in the membrane. The oriented structure of the protein is fed into the CHARMM-GUI membrane builder to be packed with the specific types of lipid molecules. Finally, the Moltemplate plugin is used to locate the membrane in the right place in the simulation box and to fill the box with the appropriate number water molecules. Some water molecules are then replaced by Na^+ and Cl^- ions to create a physiological salt concentration in the box [113].

In this study, all the simulations are done in two parts. In the first part, an equilibrium molecular dynamics simulation is performed, while in the second part, a nonequilibrium molecular dynamics approach is used to compute the thermal conductivity coefficient.

2.2.2 Equilibrium molecular dynamics

Each system undergoes an energy minimization and equilibration process. To reduce the large forces due to the possible overlaps between atoms, we run the energy minimization. The conjugate gradient method is used to minimize the initial structures. Moreover, to relax the structures, all of the membranes undergo the equilibration process at a high temperature (450 K) and pressure (170 bar) using Langevin dynamics. The equilibration procedure starts with a very small time step (0.01 fs) and is done only for a few steps (1000 steps). We increase time step and the number of steps gradually to reach the time step of 1 fs. (The equilibration is done for 1000 steps at 0.01 fs, followed by 1000 steps at 0.05 fs, followed by 1000 steps at 0.1 fs, followed by 2000 steps at 0.2 fs, followed by 5000 steps at 0.5 fs, followed by 100 000 steps at 1.0 fs.) The equilibration process is then continued by another 1 ns under NPT

condition at temperature 330 K and pressure 1 bar to stabilize the area per lipid molecule. The values of the area per lipid are then evaluated with the previously reported values [78]. The systems are kept at T = 330 K, which is above the phase transition temperature of DPPC (314 K) [114], and the system pressure is adjusted to 1 bar using an isotropic Nose-Hoover barostat [115].

Table 2.1: Dimensions of the simulation box and the number of atoms in each box for different model membranes used in this study.

System	Δx (Å)	Δy (Å)	Δz (Å)	Number of Atoms
0% Cholesterol	48.0	46.0	184.2	42 804
5% Cholesterol	47.4	45.0	186.3	41 756
11% Cholesterol	45.0	46.6	188.4	41 476
50% Cholesterol	42.2	38.8	194.2	33 762
Asymmetric Cholesterol	44.4	44.4	180.0	36 338
APP on the membrane	54.4	54.2	187.0	57 734
APP across the membrane	46.6	46.6	170.6	39 132

To build the appropriate simulation box for the implementation of the NEMD approach and to have a correct periodic boundary condition along the z axis, the model membrane and its mirror image are located parallel to each other in the simulation box which is filled with the appropriate number of water molecules.

Finally, to relax the water molecules and to let the final simulation box find the correct volume and density, we equilibrate the systems once more (only for a short period in the order of some hundreds of picoseconds). The same equilibration procedure as the one applied to the single lipid bilayer is used to equilibrate the double lipid bilayer in the box. Table 2.1 shows dimensions and the number of atoms in the final simulation boxes for the model membranes used in this study.

2.2.3 Thermal conductivity calculation (nonequilibrium molecular dynamics)

To implement reverse nonequilibrium molecular dynamics in our study, we use the Müller-Plathe technique [25]. In this method, the simulation box is divided into several layers. The number of layers should be selected such that it yields correct

performance considering the size of one water molecule. At each time step (or as many time steps as the user wants), the velocity of the hottest particle in the first layer in the box is exchanged with the velocity of the coldest particle in the middle layer of the box. Therefore, the exchange rate is a known, user-defined parameter. Since the total momentum should be kept conserved, only the particles with the same mass are allowed to exchange velocity. After a while, the first and the middle layers of the box changes into the coldest and hottest layers, respectively. Consequently, a physical heat flow is established from the hot region to the cold region in the box. After the system reaches a steady-state, the temperature gradient can be measured and used to calculate the thermal conductivity coefficient using Fourier law.

Implementation of Müller-Plathe technique

We divide the simulation box into 100 layers. The thickness of one layer in the box varies between 1.8 Å and 1.9 Å in our simulations, depending on the height of the box. Further information about the box dimensions and the number of atoms in each system is given in table 2.1. Particles from the first and middle (51st) layers are chosen for velocity exchange. By convention here, we consider that heat flows in the forward direction when the first layer of the box (indicated by T_2 in Fig. 2-3) has the lowest temperature, and the layer in the middle (indicated by T_1 in Fig.2-3) has the highest temperature. Therefore, the heat flows from the center toward the two ends of the box. On the other hand, the backward direction is considered when heat flows from the two ends of the box toward the center. We exchange the velocities every 0.1 ps. With this exchange rate, we are always in the linear response regime. Accordingly, thermal conductivity coefficient is calculated using Eq. (2.1).

$$\kappa = -\frac{J}{\nabla T} = -\frac{1}{2}\frac{\frac{dQ}{Adt}}{\frac{dT}{dz}} \tag{2.1}$$

where $\frac{dQ}{dt}$ is the rate of heat flow, dz is the distance between hot and cold layers in the box, dT is the difference between temperatures of hot and cold layers, and A is the cross-sectional area. Since heat flows in two opposite directions, one-half of the heat flow should be used for the calculation of the thermal conductivity coefficient

(κ).

Estimation of thermal rectification factor

Thermal conductivity coefficients are obtained in forward and backward directions and used to calculate the thermal rectification factor using Eq. (2.2).

$$\epsilon = \frac{|\kappa_f - \kappa_b|}{\kappa_b} \tag{2.2}$$

where κ_f and κ_b are the coefficients when heat flows in the forward and backward directions, respectively.

2.2.4 Block averaging

Block averaging is a technique to find a correct estimate of the error in the time average of quantities that are obtained from computer simulations. According to equation 2.3, the true standard error is achieved when data in all the blocks are statistically independent [116, 117].

$$BSE(f, n) = \frac{\sigma_n}{\sqrt{M}} \tag{2.3}$$

where M is the number of blocks, n is the length of blocks, and f is the quantity for which the average and standard error are calculated. If the length of blocks is shorter than the correlation time, blocked standard error (BSE) under-estimates the statistical error because of the correlation between blocks. The true uncertainty is obtained when BSE no longer changes with block length.

To calculate the thermal conductivity coefficient, we apply the block averaging method, obtain the mean value of the thermal conductivity coefficient in each block, and find the standard error in estimates of the mean based on the different block lengths. As Figure 2-1 shows, in our study the blocked standard error almost reaches a plateau for block lengths around 1000 picoseconds. Therefore, we choose blocks with one nanosecond length for the calculation of thermal conductivity coefficients.
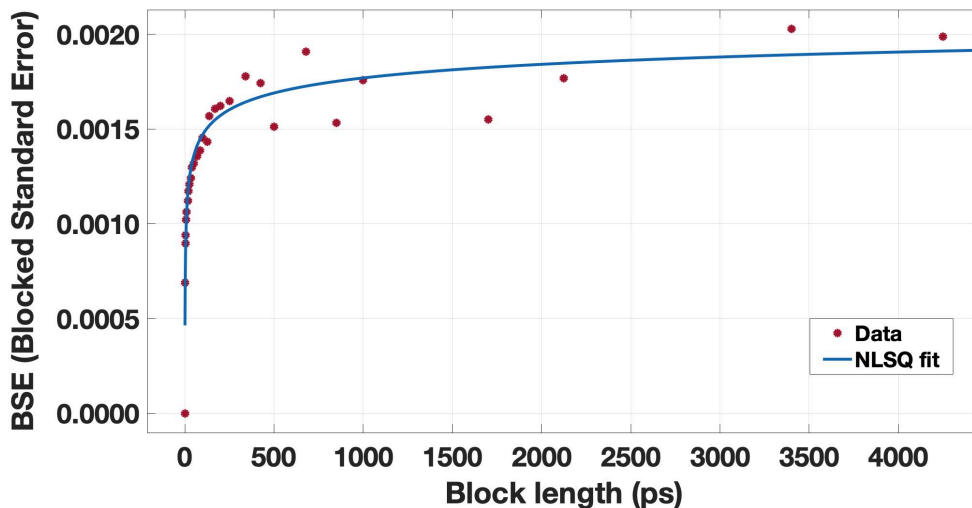
Figure 2-1: Blocked standard error as a function of block length. The nonlinear least square (NLSQ) fit to the data indicates that BSE almost reaches a plateau for block lengths around 1000 picoseconds.

2.3 Results

2.3.1 Thermal conductivity of DPPC membrane at different levels of cholesterol

To investigate the effect of cholesterol on the structure of DPPC membrane, the area per lipid molecule is obtained after the equilibration phase. An increase in the level of cholesterol in the membrane results in a reduction in the area per lipid molecule (Figure 2-4 and table 2.1). It is reported in previous studies as well [118, 79]. Furthermore, our findings suggest that the membranes with more cholesterol molecules have a higher thickness, which is in agreement with previous reports [119, 120].
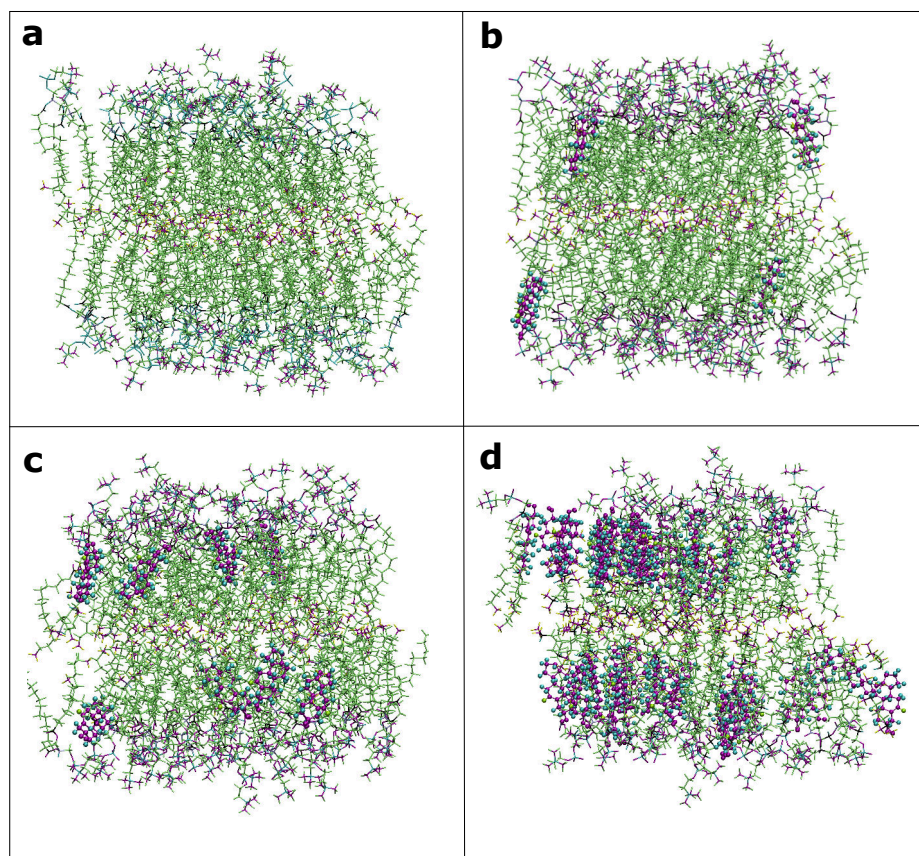
Figure 2-2: Pre-equilibrated DPPC lipid membranes with different cholesterol concentrations: (a) 0% cholesterol, (b) 5% cholesterol, (c) 11% cholesterol, and (d) 50% cholesterol. Each membrane leaflet consists of 36 lipids including DPPC and cholesterol molecules. DPPC molecules are represented with lines in green and cholesterol molecules are represented with ball-and-stick in blue and purple.
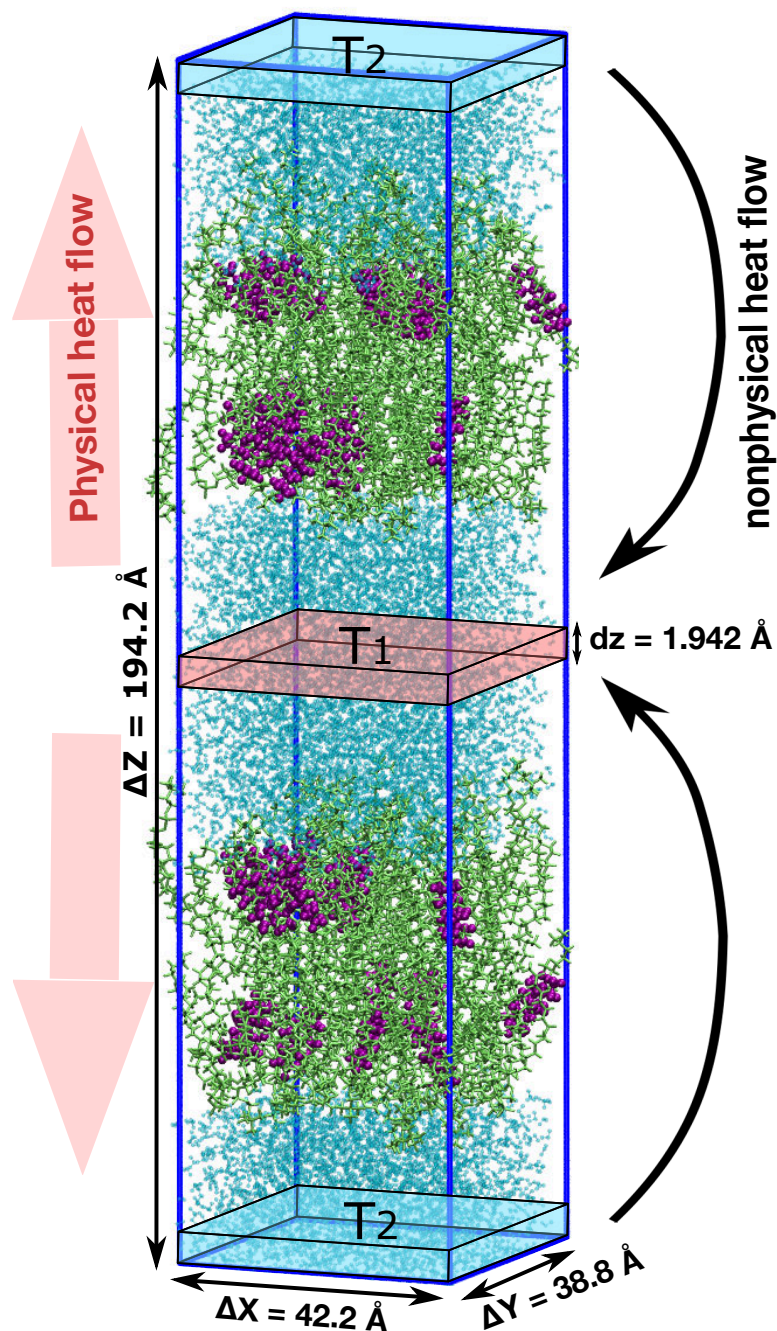
Figure 2-3: Physical and nonphysical heat flow across the model membrane with 50% cholesterol concentration. The Müller-Plathe NEMD algorithm applies a nonphysical heat flow between two layers of the simulation box, specified with T_1 (hottest layer) and T_2 (coldest layer) which results in a physical heat flow across the lipid bilayers. Water layers with the highest and the lowest temperatures are colored in light red and light blue, respectively. In the two lipid bilayers, green lines and purple beads represent DPPC and cholesterol molecules, respectively.
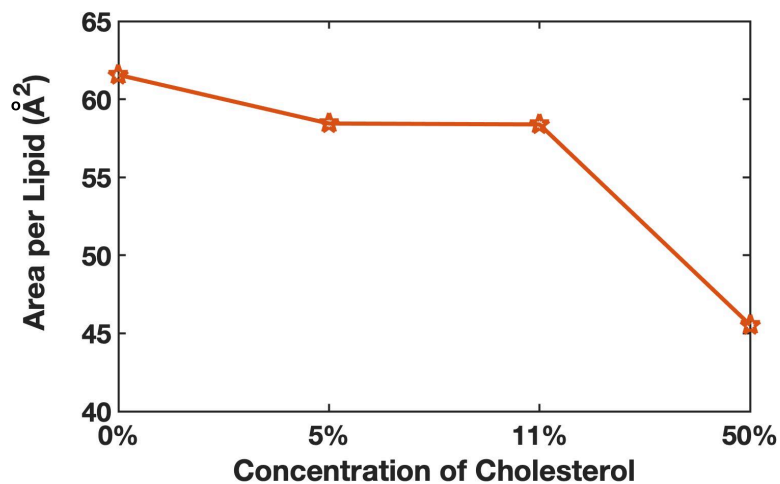
Figure 2-4: Area per lipid molecule for DPPC membranes containing different concentrations of cholesterol. The numbers on the horizontal axis indicate the percentage of cholesterol in each membrane leaflet.

Implementation of the Müller-Plathe algorithm leads to the creation of hot and cold slabs across the membrane. Temperatures of hot and cold slabs reach a steady state after some hundreds of picoseconds (Figure 2-5). In our study, we do all the calculations on the data gathered after the first nanosecond of the simulations.
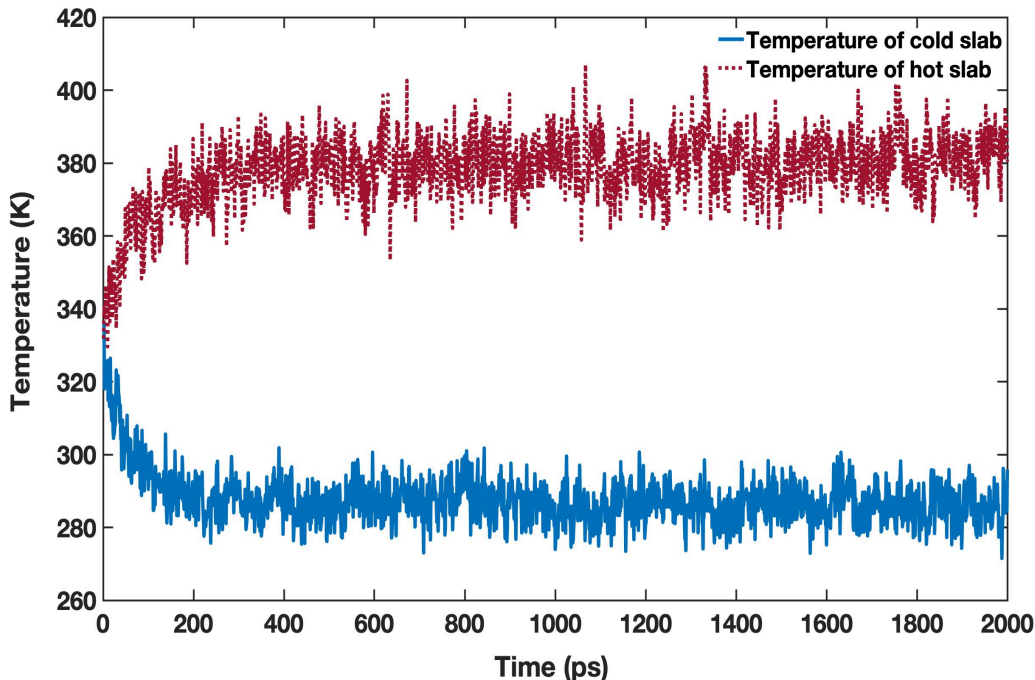
Figure 2-5: Implementation of Müller-Plathe algorithm results in the formation of hot and cold regions in the box. This figure represents the first 2 ns of the NEMD simulation. This plot implies that the temperature of the hot and cold slabs reaches a steady state in hundreds of picoseconds after NEMD starts with an exchange rate of 0.1 ps. All model membranes we use in this study have similar plots to this one.

The density and temperature profiles of the system along the z axis (Figure 2-6) suggest that in the hottest and coldest layers of the box there are only water molecules. It is worth mentioning that the two jumps in the temperature profile (Figure 2-6), one in the region between slab number 20 and 30, and the other in between slab number 70 and 80, match exactly the two minimums in the membrane density profile indicating the areas between the two membrane leaflets where lipid tails touch [8]. Density profiles in Figure 2-6 indicate the density of particles before applying NEMD to the system. After NEMD is applied to the system, there is a slight change in the density of water with a higher density in the cold region and a lower density in the hot region. However, there is no change in the density of lipids.
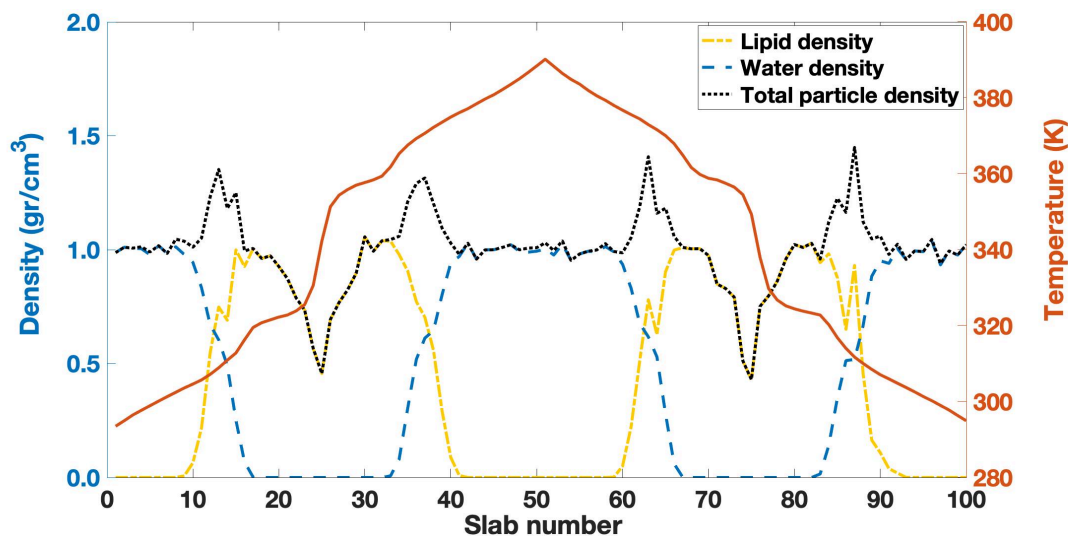
Figure 2-6: Densities of water, lipid, and the total particle density along the z axis are represented on the left vertical axis. The temperature of each layer when the system reaches the steady state is also represented on the right vertical axis. The overall density and temperature profiles of all model membranes we use in this study are similar to this one.

Temperature profiles of the lipid bilayers along x and y axis are averaged over all membrane and illustrated in Figure 2-7 and 2-8.
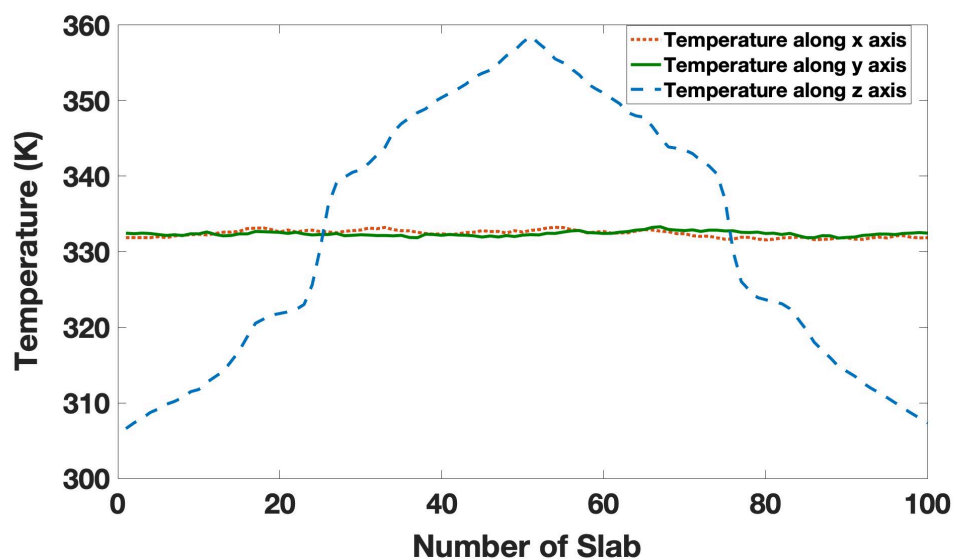
Figure 2-7: Temperature profile of the lipid bilayers in three dimension for the membrane containing 50% cholesterol. In this figure energies are exchanged every 0.2 ps.
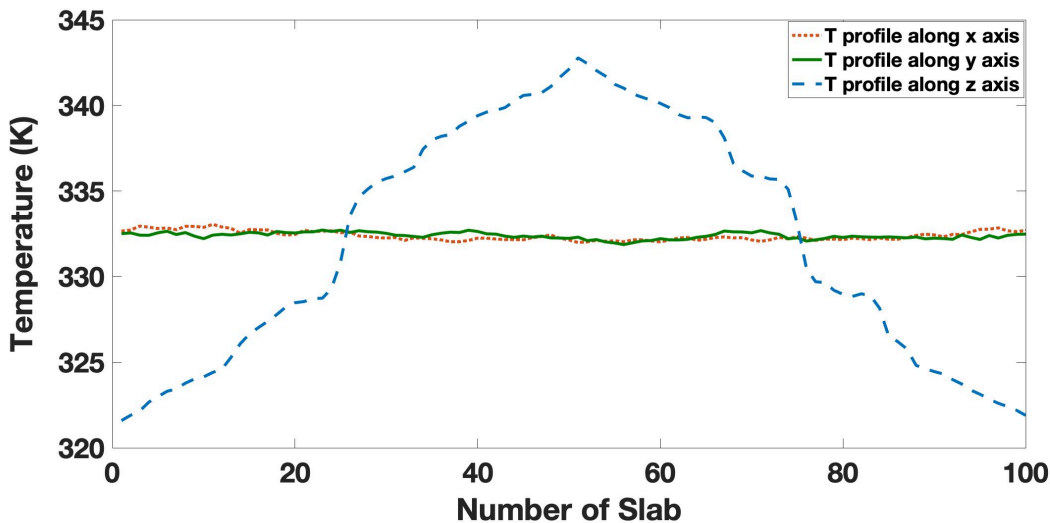
Figure 2-8: Temperature profile of the lipid bilayers in three dimension for the membrane containing 50% cholesterol. In this figure energies are exchanged every 0.5 ps.

We report the value of the thermal conductivity of the DPPC membrane to be 0.57 ± 0.01 W m^{-1} K^{-1} at ΔT=74 K, which is in good agreement with the computationally predicted value (0.51 ± 0.04 W m^{-1} K^{-1} at ΔT=75 K) by Yousefian et. al. [103]. To the best of our knowledge, the only experimentally measured value reported very recently is 0.20 ± 0.02 W m^{-1} K^{-1} obtained for a membrane composed of DOPA:DOPC:cholesterol (with the ratio of 64:7:29) at ΔT=20 K [7]. The difference in the reported values of the membrane thermal conductivity is not only due to the different membrane compositions but also because of the difference in the applied temperature gradients across the membrane [7, 103]. For instance, in a previous computational study, the thermal conductivity of 0.25 W m^{-1} K^{-1} was reported for a DPPC bilayer at ΔT=12 K [92].

According to the results of the t test (Table 2.2), the presence of cholesterol in the membrane, especially in high concentration, increases the thermal conductivity of the lipid bilayer (see Fig. 2-9). The reason can be partly explained by the increased structural order in the membrane (in liquid phase) due to the addition of cholesterol that is in total agreement with the previous reports [81]. These results suggest that the increase in the thermal conductivity of each two membranes (containing different

levels of cholesterol) is statically significant (significance level=0.05), except for the two membranes with cholesterol concentrations 5% and 11%.
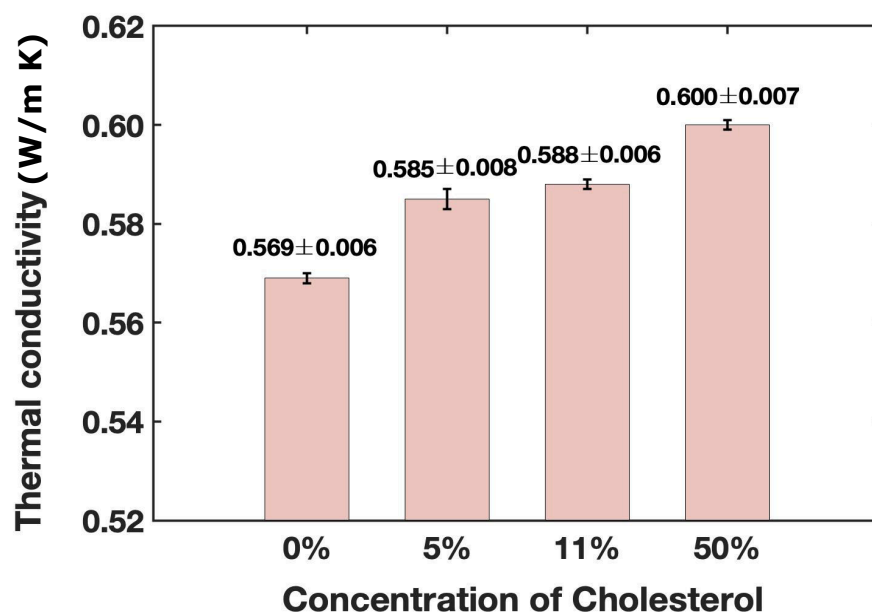
Figure 2-9: Thermal conductivity coefficients of lipid membranes with different concentrations of cholesterol. Simulations are divided into several 1 ns time blocks and the thermal conductivity coefficient is obtained in each block. The mean value ($\pm$ standard deviation) written on top of each bar is obtained using block averaging method. Error bars show the value of standard deviation divided by the square root of the number of blocks.

Table 2.2: Result of the t test for membranes with different levels of cholesterol.

Systems	Mean diff.	Std. err. diff.	t	df	Sig. (2-tailed)
0%, 5%	-0.016	0.002	-7.692	38.0	$p < 0.001$
0%, 11%	-0.019	0.002	-10.958	42.0	$p < 0.001$
0%, 50%	-0.032	0.002	-17.346	43.0	$p < 0.001$
5%, 11%	-0.003	0.002	-1.161	36.0	$p = 0.241$
5%, 50%	-0.015	0.002	-6.546	37.0	$p < 0.001$
11%, 50%	-0.013	0.002	-6.589	41.0	$p < 0.001$

In Müller-Plathe technique, a specific amount of kinetic energy is accumulated in each simulation step which is due to the exchange of velocities. If the velocities are exchanged slowly enough, the accumulated kinetic energy will be a linear (monotonically increasing) function of time. Otherwise, the system will never reach a steady state. The slope of this line gives the rate of heat flow.

To investigate the effect of different temperature gradients on the value of thermal conductivity and to check whether we stay at the linear response or not, thermal conductivity is calculated at three different temperature gradients for the membrane containing 50% cholesterol. The value of thermal conductivity at $\Delta T = 21$ and $\Delta T = 50$ is equal to 0.596 and 0.6, respectively.

Figure 2-10 shows the rate of heat flow as a function of ΔT indicating that even at high ΔT the system stays (with a good approximation) in the linear response regime. Therefore, the value of thermal conductivity in our simulation does not depend on the swap frequency.
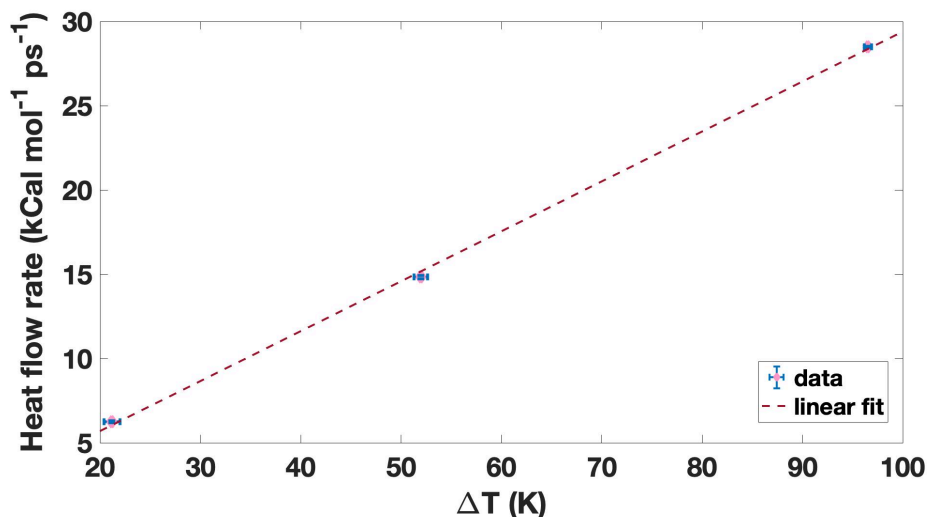
Figure 2-10: Rate of heat flow as a function of ΔT. The blue dots are obtained from MD simulations by swapping every 500, 200, and 100 time steps. A larger ΔT is obtained at higher swap frequencies. The dashed red line is the linear fit to this data. In all three simulations the thickness and cross-sectional area of the surface through which heat is transported are the same.

As we mentioned previously, in Müller-Plathe technique total linear momentum and total energy of the system are conserved because the simulations are done in an NVE ensemble without any thermostat.

2.3.2 Hydration of lipid headgroups

Results of a previous experimental study [121] suggest that cholesterol affects membrane-water interaction by increasing the water penetration to the hydrophilic part of the membrane. Since the important role of the membrane-water interface in determining thermal conductivity of membrane has been emphasized in the literature, we investigate the hydration of lipid head groups in two of our model membranes: in the cholesterol-free membrane and in the membrane containing 50% cholesterol. We obtain the radial distribution function of water oxygen around the nitrogen atom of DPPC head groups (Figure 2-11). According to the results, we conclude that the hydration increased upon the inclusion of 50% cholesterol to the membrane.
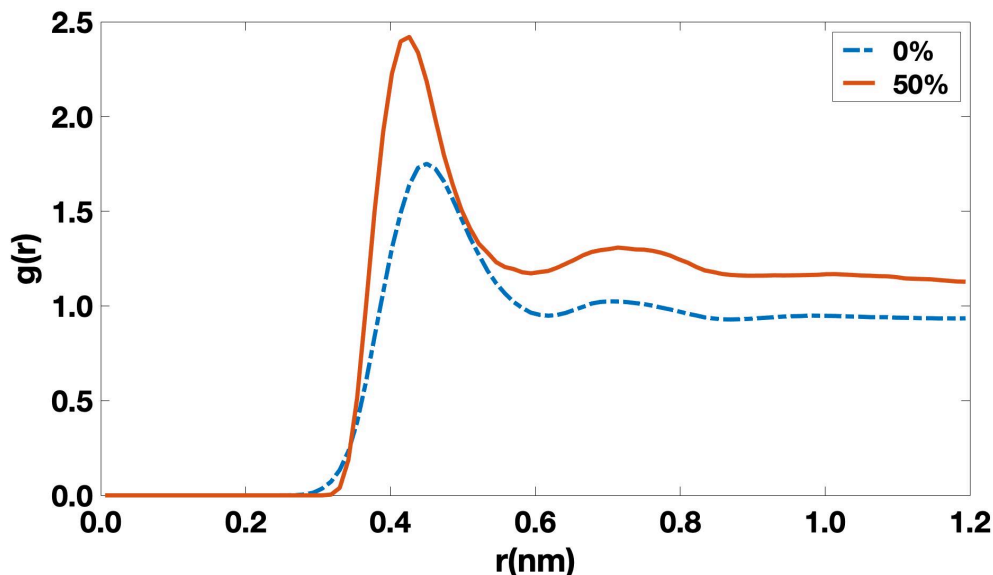
Figure 2-11: Radial distribution function (RDF) of water oxygens around the nitrogen atom of DPPC headgroups for two membranes: the cholesterol-free membrane (dashed blue curve) and the membrane containing 50% cholesterol (solid red line). A comparison between the peak values of the two RDFs reveals that the lipid head groups get more hydrated as a result of the incorporation of cholesterol into the membrane.

Thermal conductivity and rectification of a DPPC membrane with different concentrations of cholesterol in the upper and lower leaflets

The asymmetric concentration of cholesterol in the membrane leaflets has been discussed by many studies [122, 123]. To achieve more realistic results, this asymmetry should be taken into account in membrane models. In this study, we use a pre-equilibrated membrane with asymmetric cholesterol concentration in the two leaflets. Our model membrane contains 33.3% cholesterol in the outer leaflet and 2.7% cholesterol in the inner leaflet and the physiological salt concentration (0.15 M). We study the thermal conductivity of this model membrane in a forward and backward direction (Fig. 2-12).
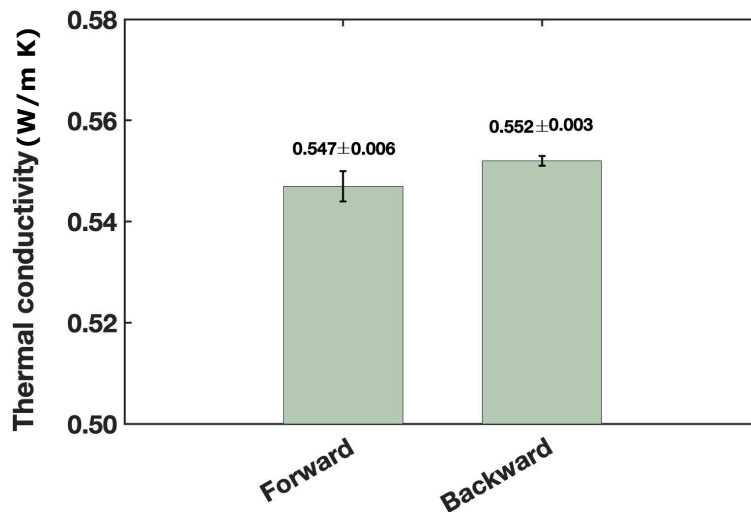
Figure 2-12: Thermal conductivity coefficients for a DPPC membrane whose upper and lower leaflets contain different numbers of cholesterol molecules. Thermal conductivity values are obtained for this model in the forward and backward directions.

The thermal conductivity coefficients obtained in both directions for this asymmetric model membrane are less than the values obtained for our aforementioned symmetric models. The asymmetry in the structure of the membrane leaflets might be the reason for the reduction in the thermal conductivity of the membrane. As a similar case, we refer to a previous computational study in which the thermal conductivity of the DPPC membranes was obtained at different temperature gradients. In the same study, the lowest value of thermal conductivity was reported for a membrane

whose leaflets were in two different temperatures, one below the phase transition temperature and the other above it [103]. One of the membrane leaflets in the gel phase and the other in the liquid crystalline phase reveal a form of asymmetry between the two membrane leaflets. Our asymmetric membrane has a rectification factor of 0.008 which is much lower than the previously reported values for archaeal membranes [9].

Besides normal asymmetry in the cholesterol content of the two membrane leaflets, a very recent study suggests that external thermal gradients can create asymmetric cholesterol distribution between the two membrane leaflets [124]. The results of the same study indicate that the flip-flop rate of cholesterol, which is a rather small and less polar molecule in comparison with other lipid molecules, is in the order of microseconds or milliseconds. Elsewhere, the cholesterol flip-flop rate is reported to be between 80 ns and 250 ns [123]. However, the timescale of our simulations was much lower (around 20 ns) than the reported values. Therefore, there is almost no chance to observe a cholesterol flip-flop in our simulations.

2.3.3 Effect of amyloid precursor protein on the thermal conductivity of DPPC membrane

To investigate the thermal conductivity of the membrane in the presence of APP, we consider two separate cases (Figure 2-13). In the first model (Figure 2-13(a)), the transmembrane domain of APP inserted into the membrane, and in the second one (Figure 2-13(b)), part of APP laid on the membrane. For both cases, we study thermal conductivity in the forward and backward directions. Our results suggest that in both cases, the thermal conductivity coefficients in the forward direction are different from the ones obtained in the backward direction (Figure 2-14). Table 2.3 represents the values of thermal conductivity coefficients and the rectification factors for both cases.

Table 2.3: Thermal conductivity coefficients (κ) and rectification factors (ϵ) are reported at specified temperature differences for the two illustrated models in Fig. 2-12. In the third and fourth columns, the standard deviations (SD) are specified inside the parenthesis.

System	Direction	ΔT (SD) K	κ (SD) W m^{-1} K^{-1}	ϵ
a	Forward	76.0 (1.5)	0.534 (0.005)	0.043
	Backward	74.9 (1.2)	0.512 (0.005)	
b	Forward	62.0 (1.1)	0.549 (0.005)	0.033
	Backward	62.5 (0.9)	0.568 (0.005)	
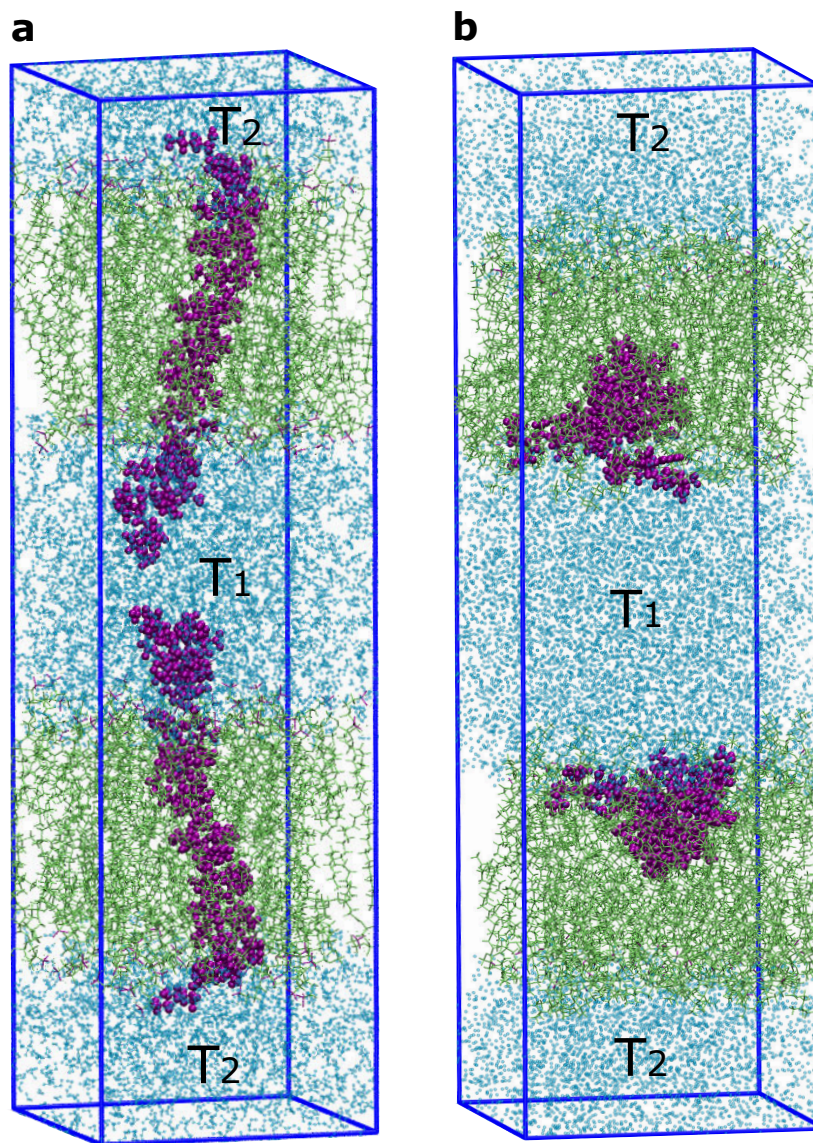
Figure 2-13: Two membrane-protein systems. In system a, the transmembrane domain of APP is packed with DPPC molecules. In system b, part of the APP laid down on the lipid membrane. Lipids, protein, and water molecules are colored in green, purple, and cyan, respectively.

2.3.4 Rectification in the thermal conductivity of the cell membrane as a result of membrane-protein interaction

We applied a t test to the values of thermal conductivity coefficients in the forward and backward directions for the two membrane-protein systems. According to the

results of this test (Table 2.4), the values of the thermal conductivity coefficients have a significant difference when measured in the forward direction than the backward direction. The rectification factors we obtain for the two membrane-protein systems are comparable with the previously reported rectification factors for other types of cell membranes (between 0.028 and 0.091) [9].

Table 2.4: Result of the T-test for thermal conductivity coefficients in the forward (F) and backward (B) directions for the two membrane-protein systems illustrated in Fig. 2-12.

Name	Mean diff.	Std. err diff.	t	df	Sig. (2-tailed)
System a (F,B)	0.022	0.002	11.299	28.0	$p < 0.05$
System b (F,B)	-0.019	0.001	-13.856	42.0	$p < 0.05$
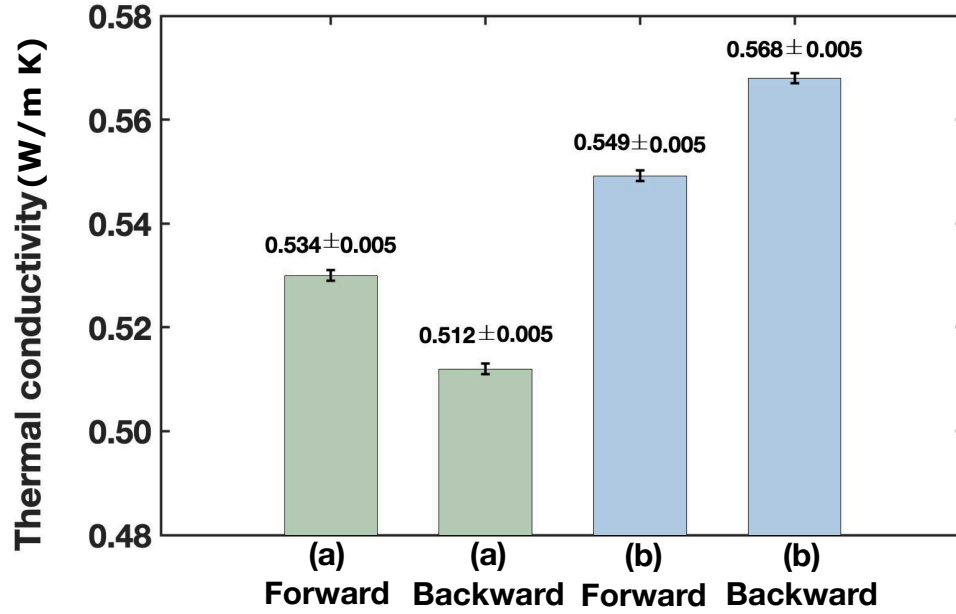
Figure 2-14: Thermal conductivity coefficients of the membranes with amyloid precursor protein in the forward and backward directions. The two leftmost columns show the value of thermal conductivity for system a in Figure 2-13) and the two rightmost columns show the value of thermal conductivity for system b in Figure 2-13)

2.4   Conclusion

In this part of our study, we applied a reverse nonequilibrium molecular dynamics approach to obtain the thermal conductivity of atomistic models of DPPC membrane with different compositions. We obtained the thermal conductivity of DPPC membrane at four different cholesterol levels. Our study finds a positive correlation between the concentration of cholesterol in the membrane and the membrane thermal conductivity. We relate the increase in the membrane thermal conductivity to the increased structural order in the membrane upon the addition of cholesterol. It is stated elsewhere that the hydrophobic effect of cholesterol is responsible for packing the hydrocarbon chains of lipids (hydrophobic part of lipid molecules) and therefore, increasing the order in the membrane [125]. The results obtained from our model membrane with an asymmetric distribution of cholesterol in the two membrane leaflets further support this idea. The lower value of thermal conductivity of the asymmetric membrane in comparison with the symmetric membranes indicates the close relationship between the structural order in the membrane and the membrane thermal conductivity. Furthermore, our simulations suggest that the inclusion of cholesterol to the membrane enhances the hydration of phospholipid headgroups. The increased density of water molecules at the lipid-water interface enhances the membrane-water interactions which can partly compensate the sharp drop in the local thermal conductivity profile at the lipid-water interface reported in a previous study [8].

It is also evident that cholesterol increases the van der Waals interactions between the hydrocarbon chains of lipids. The increased van der Waals interaction could be responsible for the increased thermal conductivity in the lipid membrane. This is analogous to the increased thermal conductivity of simple fluids at a high density which is mainly due to the repulsive intermolecular forces [126, 127].

For the membranes decorated with APP, we observe a significant difference between the thermal conductivity coefficients in the forward and backward directions. Consequently, there is a rectification effect when heat flows in opposite directions

through the membrane-protein system. Many believe that the rectification depends on the temperature difference across the membrane [9]. However, the rectification factors we obtain for the membrane-protein models are more comparable with the previously obtained values (between 0.028 and 0.091) for asymmetric archaeal membranes at ΔT=20 K [9] than the ones obtained (between 0.1 and 3.5) for carbon nanotubes at ΔT=100 K [128, 129]. We conclude that thermal rectification is more affected by the structure than the temperature gradient, but further studies are required to prove it.

The results of this study shed light on the selective treatment methods, such as photothermal cancer therapy [130]. According to what we report for the specific case of colorectal cells here, normal cells with a large ratio of $[CHL]_o/[CHL]_i$ and a high thermal resistance, can survive during the treatment process.

Chapter 3

Interaction between Aβ(16-23) and the amorphous silica surface

3.1 Introduction

Amyloid formation is known as a multilevel process starting with oligomerization or nucleation and continuing to fibril growth or elongation. Conventional experimental techniques such as X-Ray crystallography and nuclear magnetic resonance imaging are not able to characterize fibrils morphologically [131].

In this respect, MD simulation can help as a connection between the macroscopic experimental observations and the microscopic events. However, the sufficient sampling of large systems and slow processes (such as nucleation) at the experimentally-relevant timescales of microseconds and milliseconds is still a real challenge even with today computational facilities [132].

In this study, we are going to quantify the behavioral changes of a sequence of amyloid beta (1-42) peptide near the silica surface. This sequence is known to be the hydrophobic core of amyloid beta (1-42) peptide and therefore, seems to play an important role in amyloid formation. Our goal is thus to provide some insights into the changes in conformation that this small segment experiences near the surface of silica and also the specific binding modes that it can take. The results can be utilized for a better understanding of the underlying mechanisms of amyloid formation near the silica surface.

Investigating the binding of a sequence of amyloid beta (1-42) peptide (KLVFFAED)

to silica is motivated by recent experiments with transmission electron microscopy suggesting that silica nanoparticles can accelerate fibrillation of amyloid chains and this effect is sensitive to temperature [6].

3.2   Methods

We perform molecular dynamics simulations using the GROMACS 5.1 software [133, 134, 135, 136] on a segment of the amyloid beta peptide 16-23 (KLVFFAED) consisting of 8 amino acids in contact with the water amorphous silica interface. The size of the simulation box in our study is 6.56 nm by 6.57 nm in the x-y directions respectively and 8.70 nm in the z direction. The system consists of 7718 water molecules and counter ions (Na^+ and Cl^-) to create the 0.15 M salt concentration. The interaction potentials between the amyloid peptide and water were obtained using a combination of GROMOS43a1 [137, 138] and SPC/E [139] while the interaction potentials between the water and silica are adopted from a previous parametrization of the silica-water surface [64, 65] which was further extended to model biomolecules near the silica surface [1, 66]. In summary, the potential was calibrated to reproduce binding energies obtained from quantum chemistry calculations on molecular groups that are important for biomolecules. For more details on the form of the potential and how it was developed the reader is referred to the relevant papers.

To integrate the equations of motion of all atoms in the system, the leap-frog algorithm is chosen [140]. The Lennard-Jones cutoff distance is 1.0 nm for the van der Waals interactions and particle-mesh Ewald (PME) method with a grid spacing of 0.12 nm and a 4 [th] order spline interpolation is used to calculate electrostatic interactions in our systems [141, 142]. Periodic boundary conditions are also applied to all of the simulations. Simulations are done in the NVT ensemble and equilibrated at 300 K using the velocity-rescale thermostat [143].

As mentioned earlier, one of the goals of our study is to investigate how the silica surface can change the conformation of the amyloid-beta segment and to understand the underlying binding modes that occur when the peptide comes close to the surface. In order to understand these effects, we first simulated KLVFFAED in bulk water in

the absence of a silica surface using a periodic box with cell dimensions 5.47 nm by 5.47 nm by 5.47 nm. The total simulation time for the single peptide in water is 50 ns. We monitored the radius of gyration (R_g) throughout the trajectory (Figure 3-1). The R_g fluctuates between 0.5 nm and 0.8 nm. From the simulation of peptide in bulk water, we randomly choose 12 snapshots each with a different R_g.
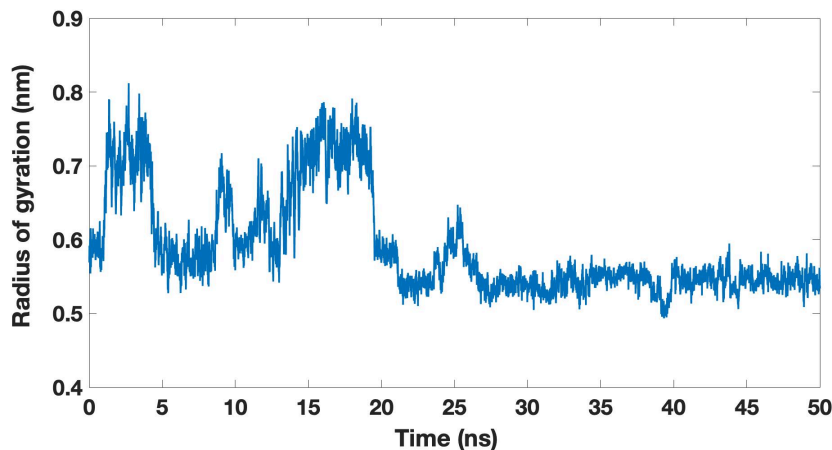
Figure 3-1: Radius of gyration of peptide throughout the trajectory.

The amorphous silica slab we simulated is characterized by a thickness of 3.4 nm containing a total of 11196 atoms (including 192 surface silanol groups, 40 geminal silanol groups and 72 dissociated silanol groups). The surface charge density is -0.82 e/nm^2 typical to neutral pH. In this study, we do not model the effect of pH. Therefore, all the simulations are done in neutral pH. Figure 3-2 shows peptide with its residues and also a top view of the silica slab. In this figure, different regions on the silica surface are specified.
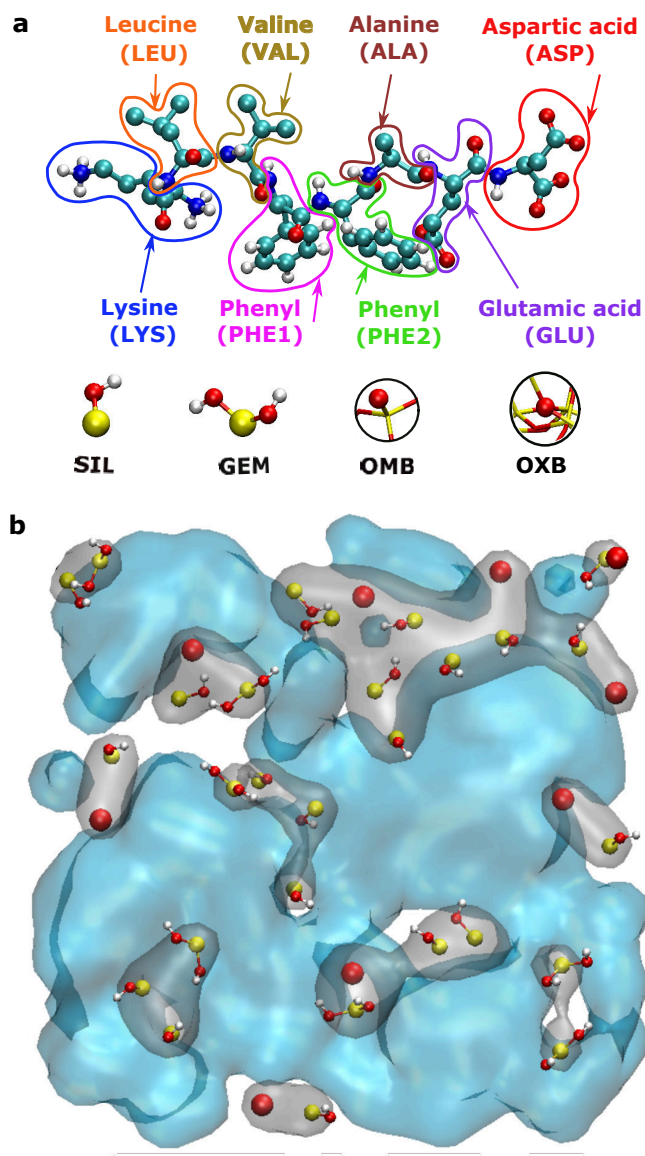
Figure 3-2: (a) The sequence of amyloid beta (1-42) peptide that we used with its 8 residues. Different colors distinguishes between different atoms. Carbon, nitrogen, oxygen, silicon, and hydrogen atoms are presented in cyan, dark blue, red, yellow, and white, respectively. Four groups of silica are illustrated below the peptide. Abbreviations are explained in the main text. (b) Top view of the surface of silica slab. Hydrophobic and hydrophilic regions are presented in blue and gray, respectively.

Besides considering different conformations, we also identify four chemical environments on the surface [Figure 3-2 (b)]: a zone rich in silanol groups (SIL), a zone rich in geminal silanols (GEM), and finally a zone with more oxygen atoms of the dissociated silanol groups (OMB) and a zone empty of charged groups in which siloxanes

(OXB) are the most available groups on the surface (hydrophobic zone). We prepare different initial configurations by placing each of the randomly oriented 12 peptide conformations above the four aforementioned zones within the Debye screening length of our system (which is approximately 0.5 nm for the chosen ion concentration). These simulations are conducted for a total of 50 ns each. Thus in total, 48 simulations were conducted yielding a wide assortment of different conformations and binding modes that the peptide takes on near the silica surface.

Visual inspections as well as the calculations of the end-to-end distance and the orientation of the peptide relative to the surface normal reveal conformational changes of peptide as it moves toward the surface. End-to-end distance has been widely used as an indicator of chain conformation and flexibility in several studies [144, 145]. The orientation of the peptide on the surface, provides information about the peptide mobility and is reported to be pH dependent [146].

We thus focused on using these two coordinates to catalog the different conformations that the peptide adopts near the surface using a hierarchical cluster analysis based on the Ward method [27].

3.3 Results

3.3.1 Conformations of peptide near the silica surface

In all but one of the 48 simulations conducted, the peptide moves to the surface and forms interactions with the different chemical groups at the interface. In the majority of our simulations, the peptide comes to the surface in the first 10 ns as is represented in Figure 3-3. Initial and final conformations of the peptide from 4 different simulations are illustrated in Figure 3-4.
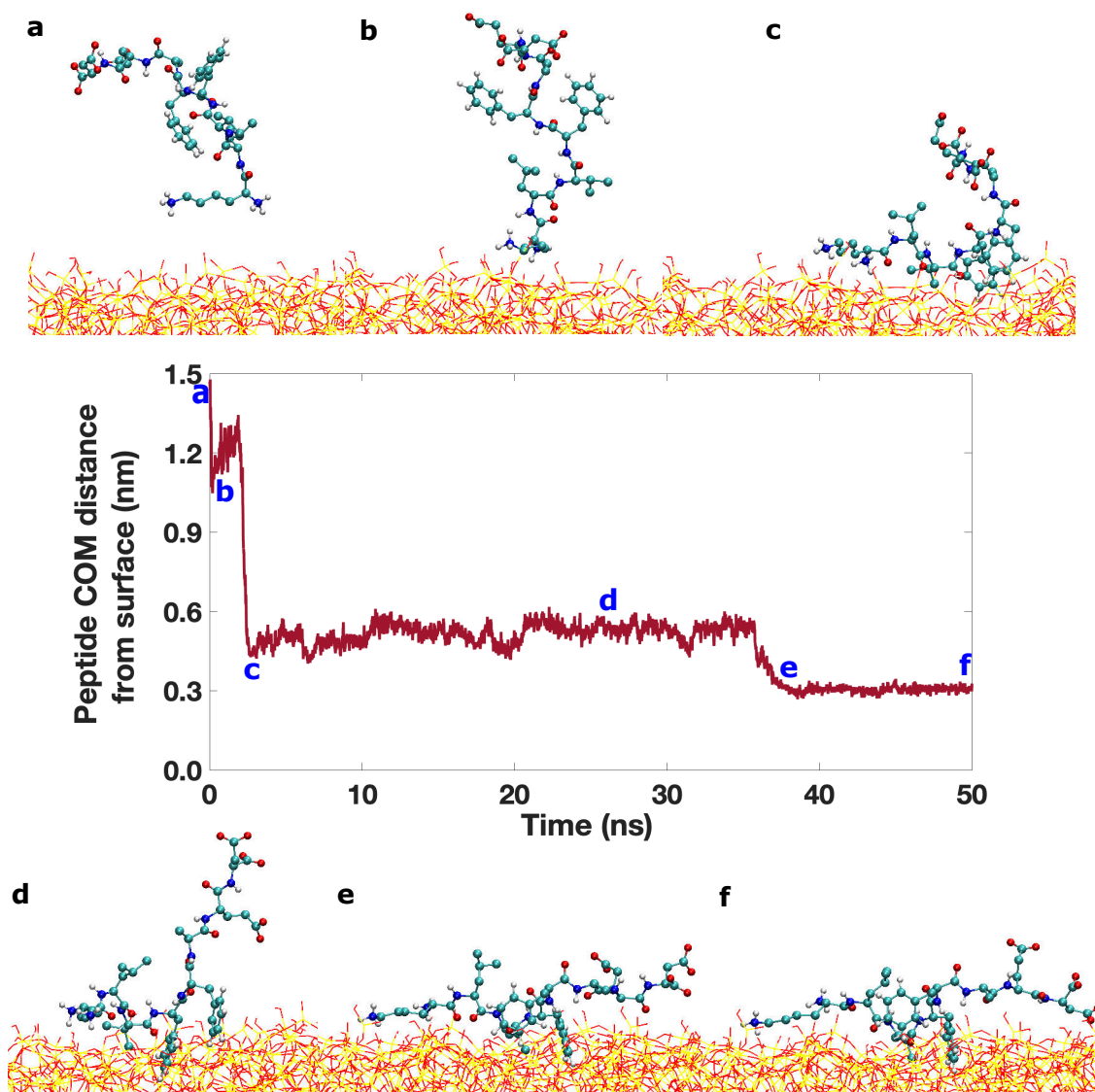
Figure 3-3: Peptide center of mass distance from the surface. Because of the surface roughness, the mean value of the z coordinates of silanol and geminal oxygen atoms is considered as the surface line. Snapshots (a) to (f) show the movement of the peptide toward the silica surface.
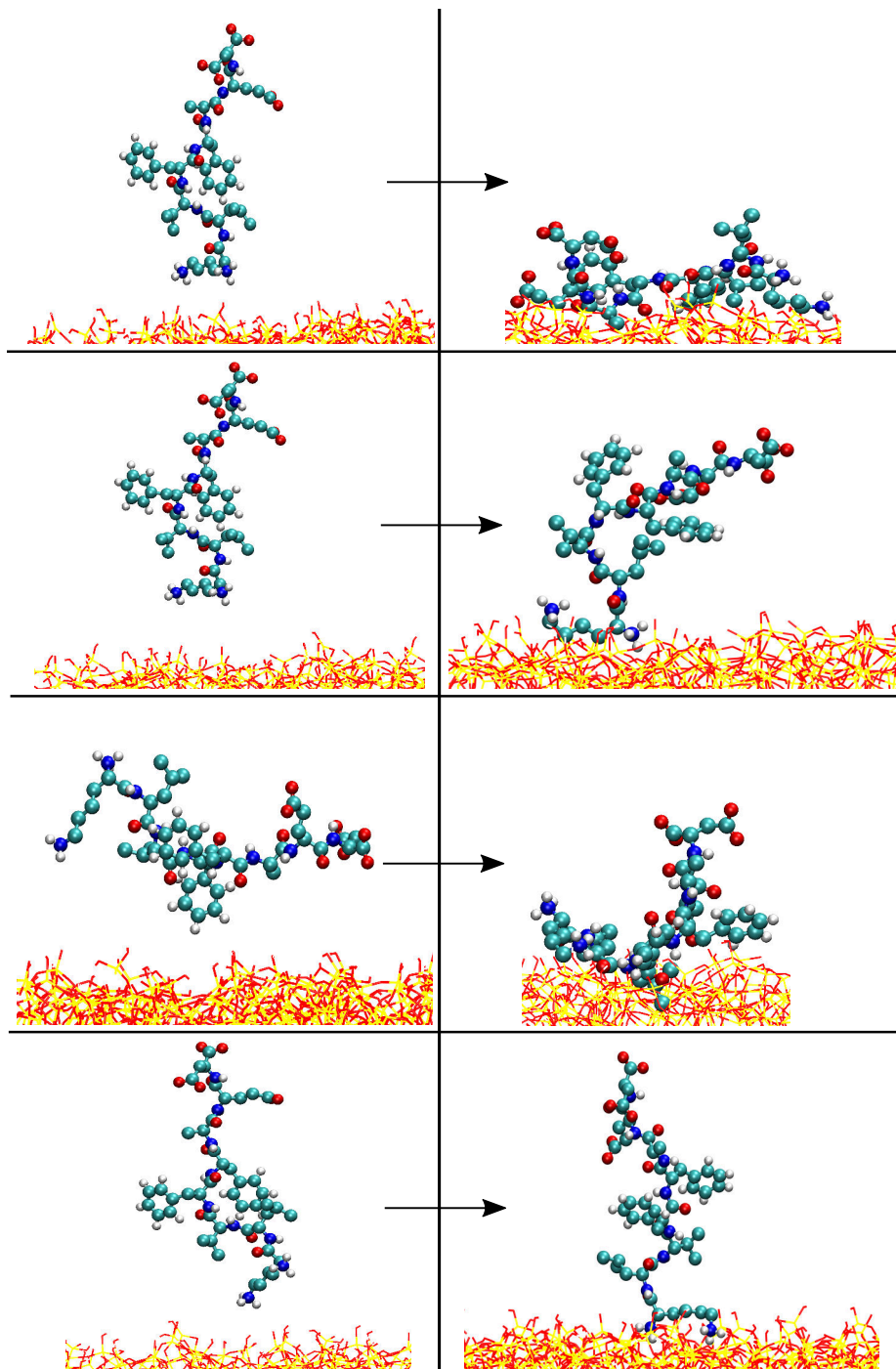
Figure 3-4: Initial (left hand side) and final (right hand side) conformations of the peptide in different simulations.

Figure 3-5 is the scree plot obtained after applying Ward's method to cluster our 48 systems based on two features of peptide conformation (end-to-end distance and the angle between surface normal and the vector associated with the N-C terminus

dipole). According to this plot, any number at which a sudden increase happens can be subtracted from the total number of cases to provide the appropriate number of clusters that should be chosen. Here, we see it happens at 45 which leads to three (48-45) clusters to be chosen. This is in agreement with what is inferred from dendrogram illustrated in Figure 3-6. This plot indicates that the largest between-cluster distance occurs when there were three different clusters.
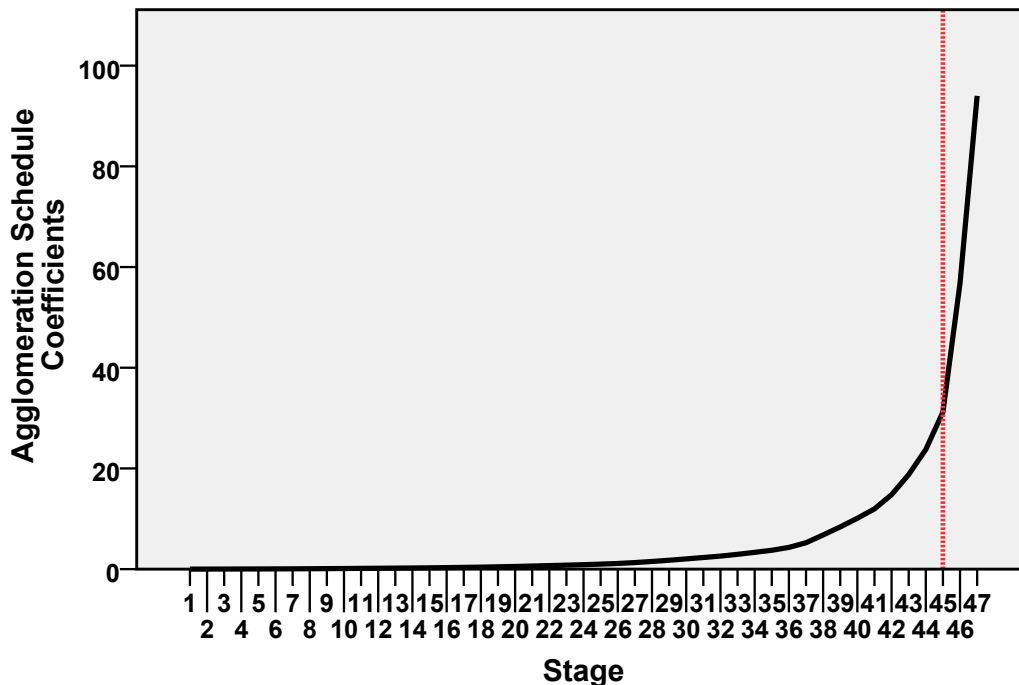
Figure 3-5: Scree plot

Broadly speaking the conformations associated with each of the three clusters are visually illustrated in Figure 3-7. In cluster (1), the peptide is bent; in cluster (2), it has an extended form, while finally in cluster (3), it is extended but with the C-terminus hanging into the solvent - essentially it is perpendicular to the surface. According to Figure 3-8, the relative percentage of the three clusters 1, 2 and 3 is 35.42%, 35.42%, and 29.17%, respectively.
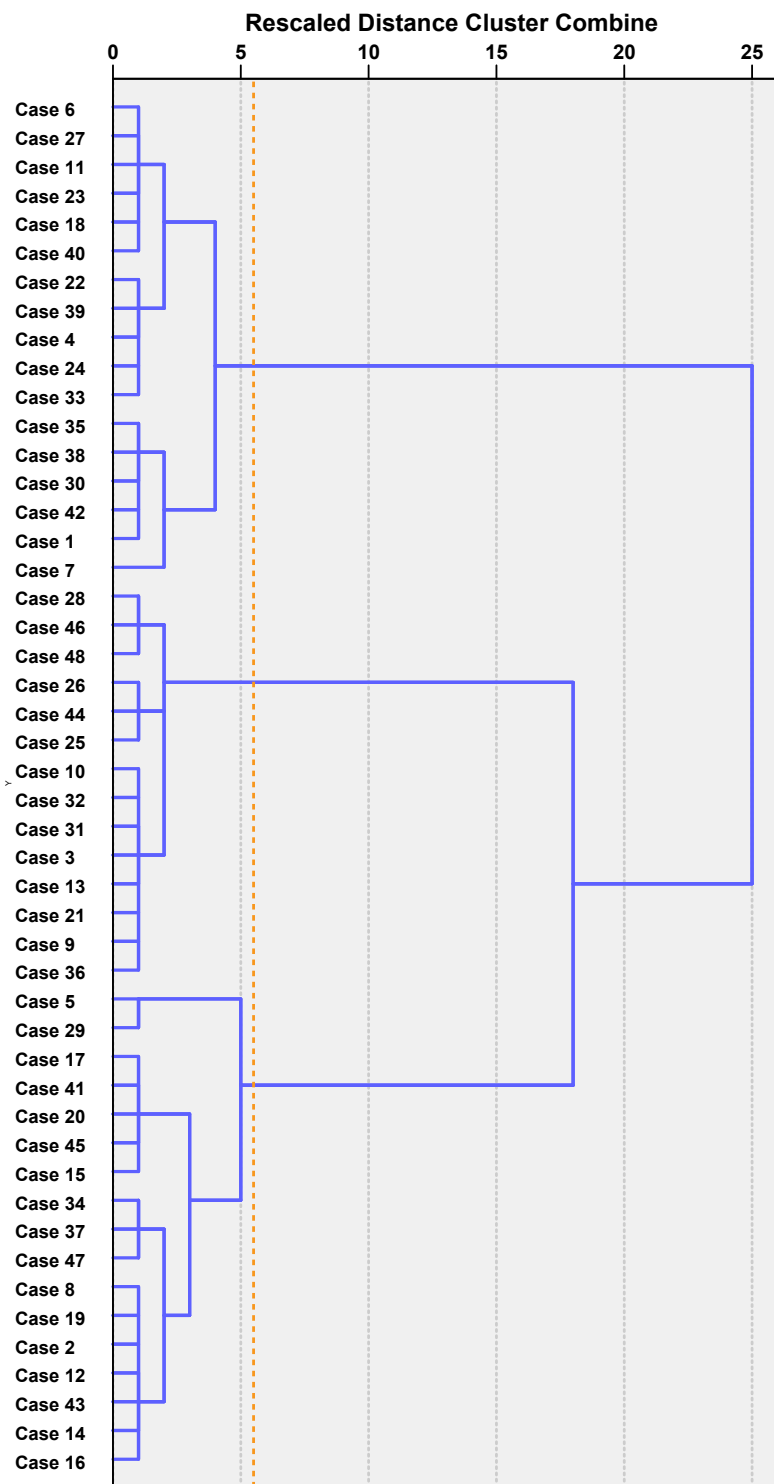
Figure 3-6: Dendrogram
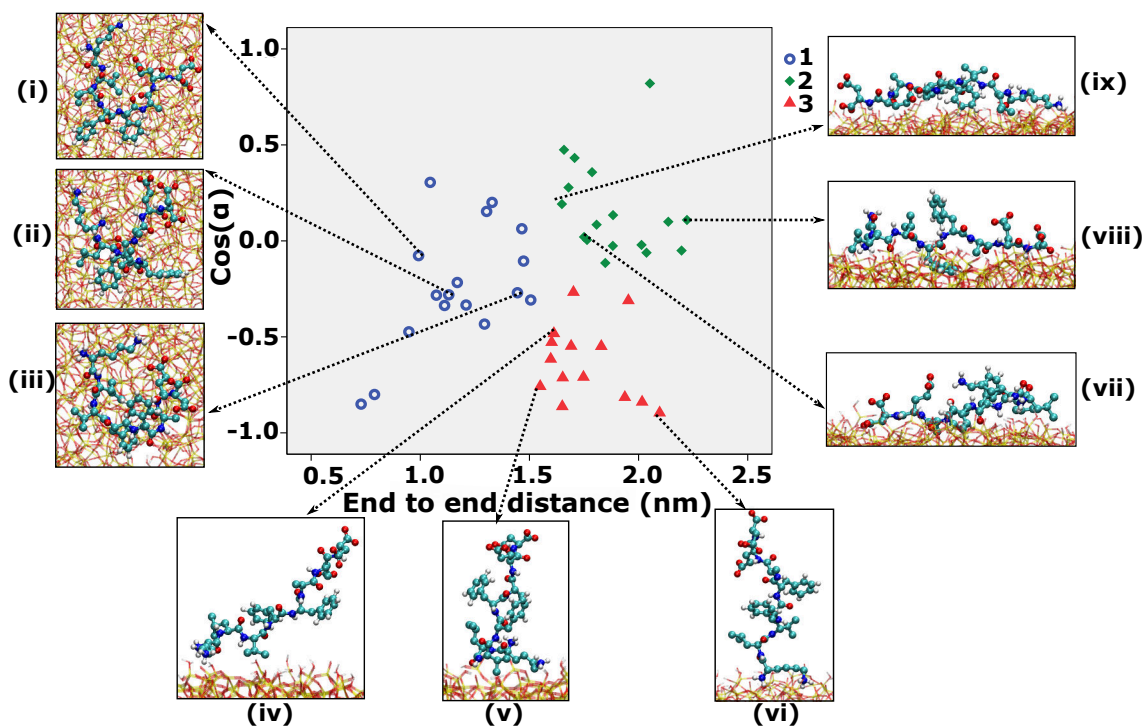
Figure 3-7: Final conformations of peptide are divided mainly into three clusters. Horizontal axis shows the peptide end-to-end distance and vertical axis is the angle between peptide N-C terminus dipole and z axis averaged over the last 10 ns of each simulation. Snapshots number (i), (ii), and (iii) are top-views of the peptide lying on the silica surface. Other snapshots show peptide from side view. Each point in this plot is related to one simulation.
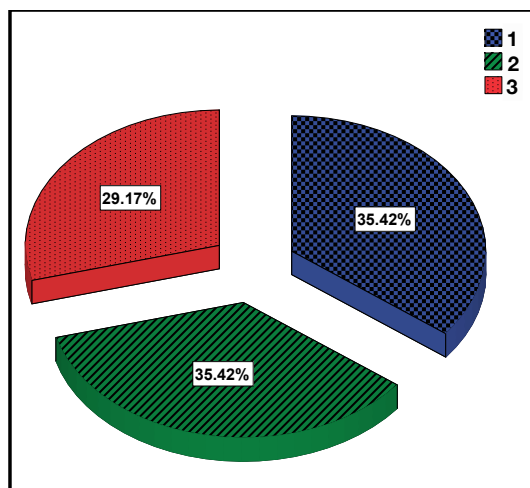
Figure 3-8: Pie plot indicating the percentages of conformations in each of the clusters in Figure 3-7.

The peptide is made up of several different chemical groups that can interact with the silica surface: the N-terminus consisting of an $NH3^+$ group, the hydrophobic phenylalanine rings, the side-chains of the lysine also consisting of $NH3^+$ groups and finally the negatively charged carboxylate (COO^-) groups. In order to determine the dominant binding modes on the silica surface, we calculate the radial distribution functions for the several groups of the peptide and the silica surface.

3.3.2   Binding modes of peptide

The peptide can bind to the different chemical groups on the silica surface shown earlier in Figure 3-2 in various different ways. In order to better quantify the relative proportion of the different binding modes on the surface, we calculated RDFs for the chemical groups of the peptide and the silica surface. Figures 3-9, 3-10, and 3-11 show the radial distribution functions of interaction neighbors involving different residues of the peptide and silica groups for a selection of final conformations of the peptide (represented in figure 3-7) in each cluster. RDFs reported here are averaged over the last 20 nanoseconds of the simulation time. Figure 3-9 show that in all three members of cluster 1, the lysine residue in the peptide N-terminal mostly binds to the silanol and geminal groups and to a less extent to the OMB groups. This can be due to the fact that in our model surface, the number of OMB groups are less than the number of silanol or geminal groups. In all three members of cluster 1, the binding of glutamic and aspartic residues (in the peptide C-terminal) to surface silanol groups is interesting but non-trivial. Moreover, in all three cluster members, at least one of the phenyl groups comes in close contact with the siloxanes. Therefore, a very nice combination of electrostatic and hydrophobic interactions are at work in binding of the peptide to the surface in cluster 1.
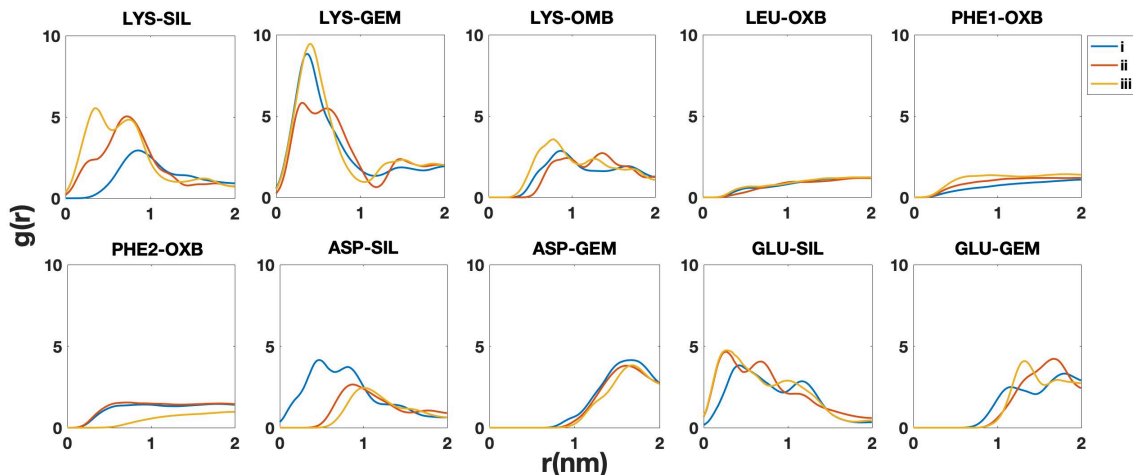
Figure 3-9: Radial distribution functions for different residues of the peptide being near the specific groups on the silica surface. In this figure, RDFs with different colors are calculated for the selected conformations in Cluster 1. To find the abbreviations of residue names and surface groups refer to Figure 3-2 and to find the selected conformations in each cluster see Figure 3-7.

for the members of cluster 2, not only N-terminal and C-terminal of the peptide make contact with polar and charged surface groups, surface geminals can bind to aspartic and glutamic residues. This is the case specifically for member (ix) in cluster 2.
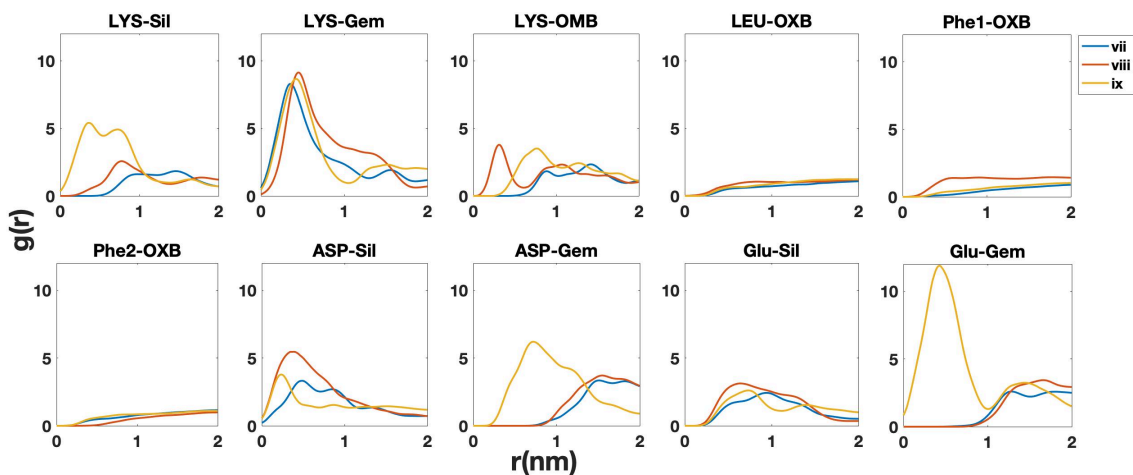
Figure 3-10: Radial distribution functions for different residues of the peptide being near the specific groups on the silica surface. In this figure, RDFs with different colors are calculated for the selected conformations in Cluster 2. To find the abbreviations of residue names and surface groups refer to Figure 3-2 and to find the selected conformations in each cluster see Figure 3-7.

In comparison with clusters 1 and 2, fewer residues are found in close contact with silica groups in cluster 3. for all the three members of cluster 3, peptide make contacts via its N-terminal lysine with (at least one of) the silanol, geminal, and dissociated silanol groups. In this case, hydrophobic residues as well as the C-terminal of the peptide have a negligible contribution in binding.
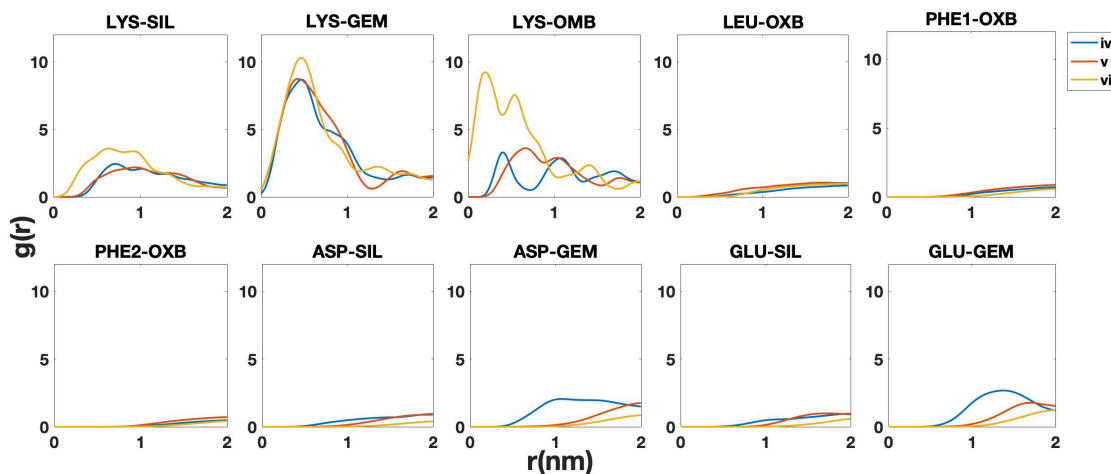
Figure 3-11: Radial distribution functions for different residues of the peptide being near the specific groups on the silica surface. In this figure, RDFs with different colors are calculated for the selected conformations in Cluster 3. To find the abbreviations of residue names and surface groups refer to Figure 3-2 and to find the selected conformations in each cluster see Figure 3-7.
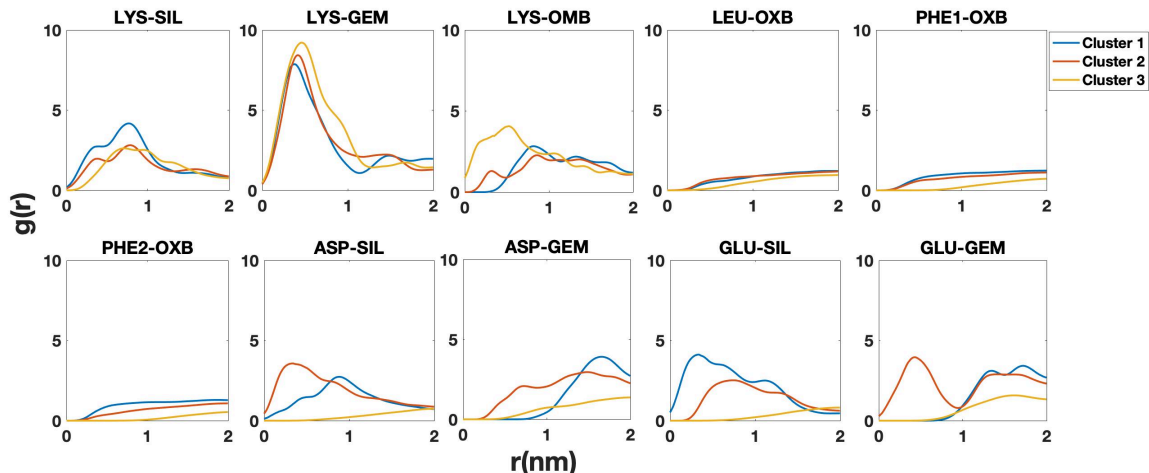
Figure 3-12: Radial distribution functions for different residues of the peptide being near the specific groups on the silica surface. In this figure, RDFs with different colors are averages of the RDFs for the selected conformations in each Cluster. To find the abbreviations of residue names and surface groups refer to Figure 3-2 and to find the selected conformations in each cluster see Figure 3-7.

Figure 3-12 shows the same RDFs which are averaged over the selected three conformations in each cluster. These results are rather interesting since they point to the important role of electrostatic and hydrophobic interactions in binding in clusters 1 and 2, with an enhanced contribution of electrostatic interactions at the peptide C-terminus in cluster 2. On the other hand, electrostatic interactions at the N-terminus of the peptide are the main drive for binding in cluster 3. In addition, hydrophobic contacts are formed mostly in clusters 1 and 2. We also observe that the hydrophobic phenylalanine groups can be buried in hydrophobic regions of the silica surface.

Interestingly, the positively charged lysine groups tend to form more contacts with the hydroxyl groups (OH in both SIL and GEM groups) rather than with the deprotonated (OMB) ones. This may originate in part by the constraints that the peptide conformation takes on at the interface. To a less extent, we also observe interactions involving the negatively charged aspartic and glutamic acid groups. Similar to previous studies, we also find that the binding of bimolecules to the surface of silica involves a complex mix of hydrophobic and electrostatic interactions [1]. This is consistent with recent experimental results showing that the adsorption mechanism of

77

intrinsically disordered p53TAD onto silica nanoparticles involves the combination of both electrostatic and hydrophobic interactions [31].

The preceding results seem to indicate that peptide binds to the silica surface as a result of electrostatic and hydrophobic interactions. However, the RDF calculations do not provide any insight into the strength of the interactions. To this end, one should calculate the energy of binding using Steered-MD or experimental methods namely adsorption isotherms.

Role of water in hydrophobic interactions

The orientation and hydrogen-bonding network of water near the surfaces with variable charge and hydrophobicity was reported to be different from those of bulk water [10]. Near the surfaces, the ideal orientation for water molecules is the one increasing the possibility of forming hydrogen bonds with both surface and bulk water, while decreasing the probability of unfavorable dipole-dipole interactions. The commonly used order parameter to evaluate the orientation of water near the surface is the tilt angle of water with respect to the surface which is defined as the angle between the axis of symmetry of water molecule and the normal to the surface (Figure 3-13). The advantage of using this order parameter is that the average value of the cosine of tilt angle can be assessed by the sum-frequency generation (SFG) experiments.
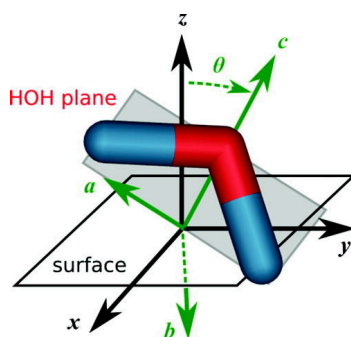
Figure 3-13: Tilt angle of water molecule is the angle between the water symmetry axis and the surface normal. This figure is adopted from reference [10].

The results of a previous study show that in the presence of peptide, the interfacial water molecules (i.e. the water molecules between the peptide and the surface) are

ordered differently, depending on the hydrophobicity of the surface [10]. Moreover, it was revealed that a highly ordered interfacial water layer is formed near the hydrophilic surfaces while interfacial water molecules near the hydrophobic surfaces are highly excluded.

Results of the same study indicate that water molecules near the hydrophilic surfaces are oriented such that their oxygen atoms are upward, pointing toward the peptide, and their hydrogen atoms are downward to the surface. Interestingly, the water molecules beneath the peptide and very close to it have the same orientation (i.e. water oxygen points toward the peptide and hydrogen atoms point to the surface). The authors believe that the similarity between the orientation of water molecules beneath the peptide and above the hydrophilic surface has a positive impact on the peptide-surface interaction because water molecules do not have to change their orientation when peptide comes to the surface. In this case, peptide usually form indirect contacts with the surface through the ordered interfacial water layer.

The same study indicated that above the hydrophobic surfaces, the water molecules are highly excluded and their orientation are different from the orientation of water molecules beneath the peptide. Therefore, the peptide and surface compete for reorienting the interfacial water molecules. This was mentioned as a possible reason for the exclusion of water from this region [10]. Consequently, the peptide comes very close to a hydrophobic surface and makes direct contacts with it.

In our study, we obtained the distribution of the number of water molecules forming closed rings in bulk water (Figure 3-14), in a 5 Å distance from the hydrophobic (Figure 3-14a) and hydrophilic residues of the peptide, and in a 5 Å distance from the silica surface (Figure 3-15b). Our results reveal that in bulk water, the closed water rings mostly consist of 6 water molecules while those formed near a hydrophilic residue (ASP) consist of 4 water molecules and those formed near a hydrophobic (PHE) residue consists of 5 water molecules. Since the closed water rings near the silica surface also consist of 5 water molecules, we can conclude that the interaction of phenyl with the surface is favorable since it dictates no essential change in the structure of water rings near the surface.
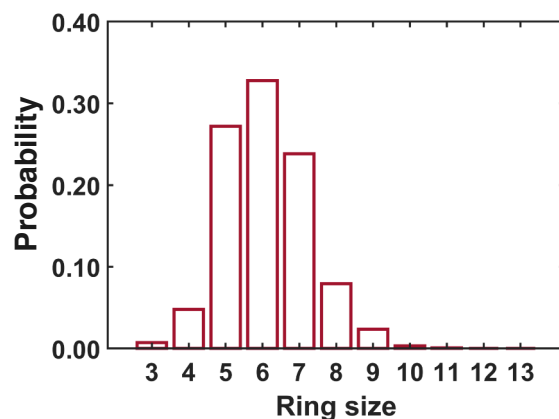
Figure 3-14: Ring analysis of bulk water in the absence of peptide and surface. This figure reveals that the number of water molecules forming a closed ring in bulk water is mostly 6.
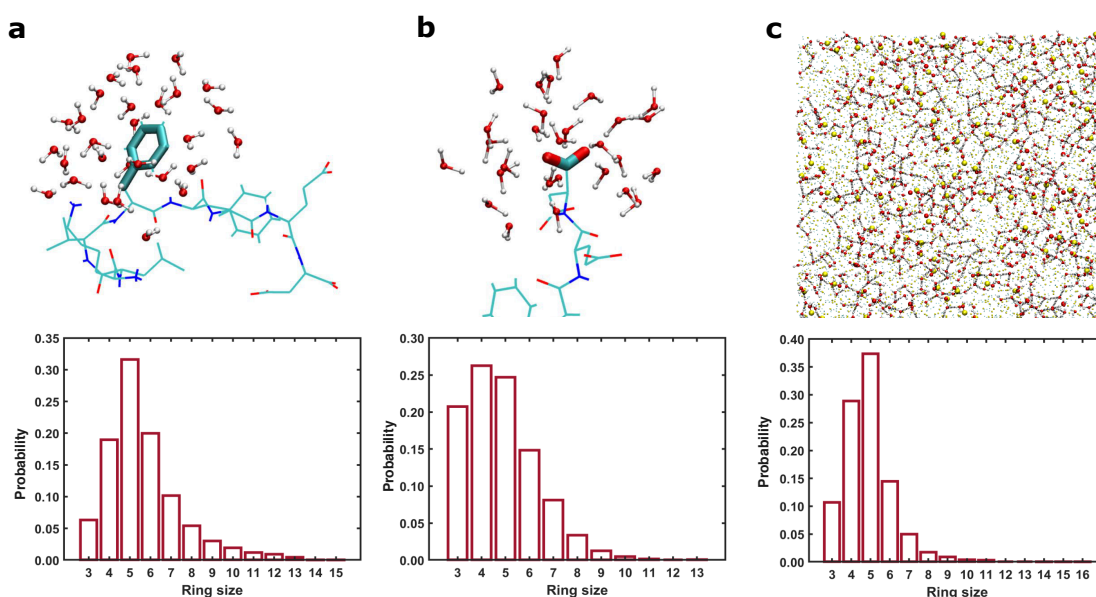
Figure 3-15: Results of the ring analysis reveal that the number of water molecules forming a closed ring is different near the (a) hydrophobic residues, (b) hydrophilic residues, and (c) above the silica surface.

Role of peptide in the structural differences of interfacial water molecules near the hydrophobic and hydrophilic surfaces

To understand the role of peptide in the structure of interfacial water molecules, Krause et al. evaluated the trapped water molecules under the hydrophobic and hy-

drophilic residues of KLα14 peptide and found similar behaviors. The authors argued that even a hydrophilic residue such as lysine consists of hydrophobic atoms. In accordance with the idea of Kapcha et al. [147], the authors assessed the trapped water molecules under the hydrophobic and hydrophilic atoms. By convention, they considered a nitrogen, an oxygen, or a hydrogen atom connected to an oxygen or a nitrogen atom as a hydrophilic atom and a hydrogen or a carbon atom connected to a carbon atom as a hydrophobic atom. Their results reveal a high density of water between the surface and hydrophilic atoms of the peptide while no water molecule exists between the surface and hydrophobic atoms. Therefore, the peptide takes advantage of the water molecules beneath the hydrophilic atoms to make contact with a hydrophilic surface while it binds directly to the hydrophobic surfaces via its hydrophobic atoms.

In this study, we observe a combination of direct and indirect contacts between the peptide and the silica surface which is mainly due to the variety of hydrophobic and hydrophilic regions on the silica surface. Figure 3-16 represents the indirect contacts between the hydroxyl groups (hydrophilic atoms) of the surface and hydrophilic atoms (hydrogen atoms of lysine residue) of the peptide. However, in this study we only quantify the number of direct contacts between the silica and peptide atoms.
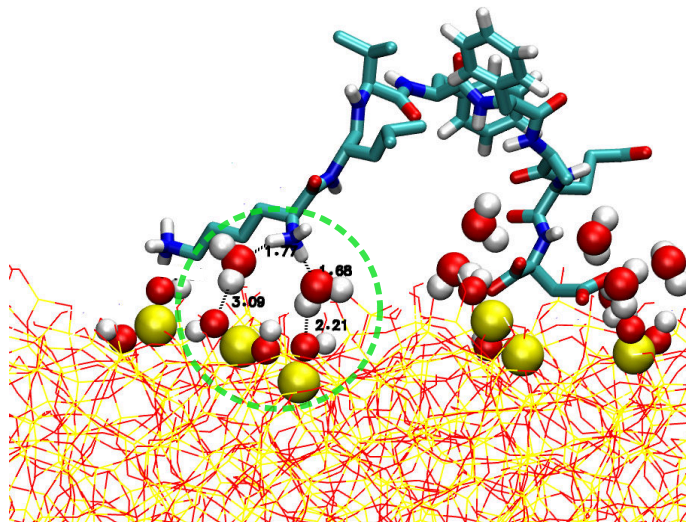
Figure 3-16: Indirect contacts between hydrophilic atoms of the peptide and hydrophilic atoms of the silica surface are indicated by dashed circle. An indirect contact is formed when a water molecule is within 3 Å distance of atoms of the silica and the peptide.

Another form of indirect contacts have also been reported elsewhere [57]. In a previous study, divalent cations shield the negative charge of DNA or silica surface by making indirect bonds either with DNA backbone or with silanol groups on the silica surface [148]. Another study revealed that water molecules binding to the silanol groups play a shielding role in DNA association to the silica gel [149].

Peptide-Solvent interaction

There have been numerous experimental and theoretical studies in the literature examining the role of the coupling between protein and solvent fluctuations, as well [150]. In particular, it is well known that protein and solvent degrees of freedom can compete with each other to stabilize various types of interactions. To this end, we obtained interaction energies between peptide and solvent as a function of center of mass (COM) distance for conformations (v) and (viii). The density plots associated with the interaction energy of the peptide with water is represented in Figure 3-17. As expected, since conformation (v) is more exposed to the solvent, it is characterized by more stronger interactions with the solvent, while the enhancement of the interactions between the peptide and silica surface in conformation (viii) results in

a decrease in its solvent exposure and therefore the magnitude of the interactions it forms with surrounding water molecules.
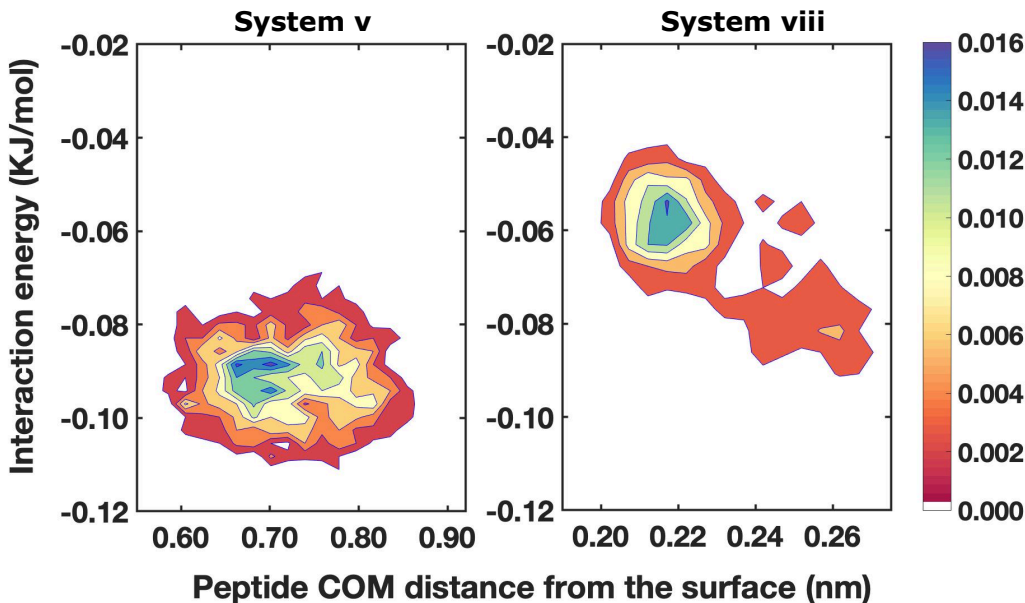
Figure 3-17: Density plot of total interaction energy (Electrostatic+van der Waals) between protein and water vs. COM distance from silica surface. Left and right figures corresponds to the conformations (v), and (viii) as specified in Figure 3-7, respectively. Energies are averaged over the last 30 ns of the simulations.

3.3.3 Re-orientational dynamics

In the preceding discussions, we have focused our efforts on examining how the silica surface affects the static properties of the peptide with particular emphasis on the binding modes and the relative importance of hydrophobic and electrostatic interactions. Given the strong interactions, we can already expect that this will have some significant effects on the dynamical fluctuations of the peptide. This in turn, would have important implications on the kinetics of amyloid aggregation.

Figure 3-18 compares the re-orientational dynamics of all the 48 configurations belonging to three different clusters. The re-orientational dynamics was examined by computing autocorrelation functions of the angle between the surface normal and the vector associated with the N-C terminus dipole, as illustrated in Figure 3-19. In addition, as mentioned earlier in the Methods section, we also examined the re-orientational relaxation associated with the peptide in bulk water.

Interestingly, we see that peptides associated with three different conformations and binding modes at the interface, are characterized by rather different rotational dynamics. In particular, cluster 2 which involves the peptide extended on the silica surface, appears to have the slowest dynamics which occurs on a nanosecond timescale. In some sense, the creation of many hydrophobic and polar contacts results in a more drastic immobilization of the peptide. This is in accordance with the previous experimental results showing limited degrees of freedom of peptide on surfaces [151]. Cluster 1 which takes on a more bent like structure appears to fluctuate slightly slower than the peptide in the bulk without the surface.
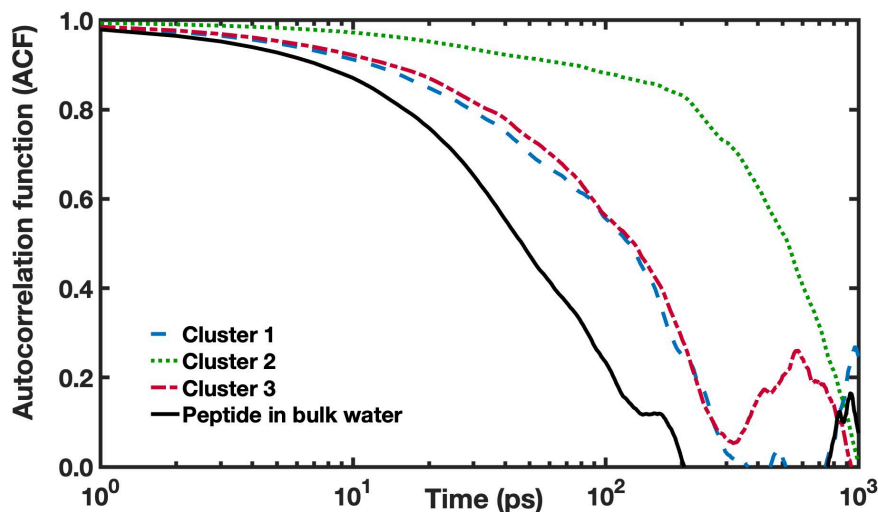
Figure 3-18: Autocorrelation function (ACF) of cosine of the the angle between N-C terminus dipole and z axis. The last 30 ns of the simulations are used for the calculation of ACF.
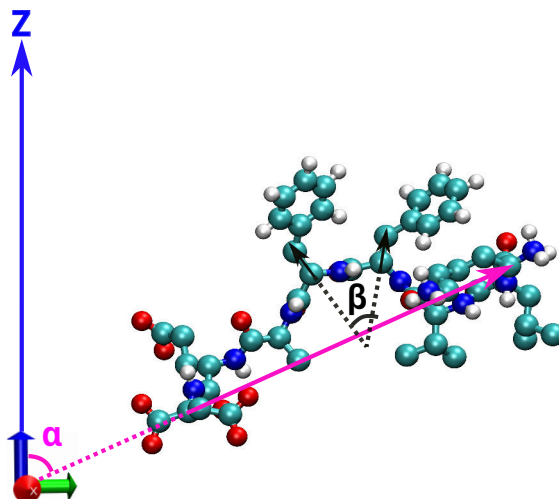
Figure 3-19: Angle α, used in the reorientational dynamics calculations, is the angle between the surface normal and the vector associated with the N-C terminus dipole.

In addition, we investigated the re-orientational dynamics of the two phenyl residues with respect to each other by calculating the autocorrelation functions of the cosine of angle between the two phenyl dipoles (the vector connecting atom CA to atom CB) as is indicated with β in Figure 3-19. According to the results (Figure 3-20), the slowest and fastest dynamics belong to the peptide conformations in cluster 1 and 2, respectively. However, the difference between the autocorrelation functions for this coordinate is not so significant. A magnified image of the shaded region in Figure 3-20a is represented in Figure 3-20b representing an initial sharp decrease of the autocorrelation functions.

a

b
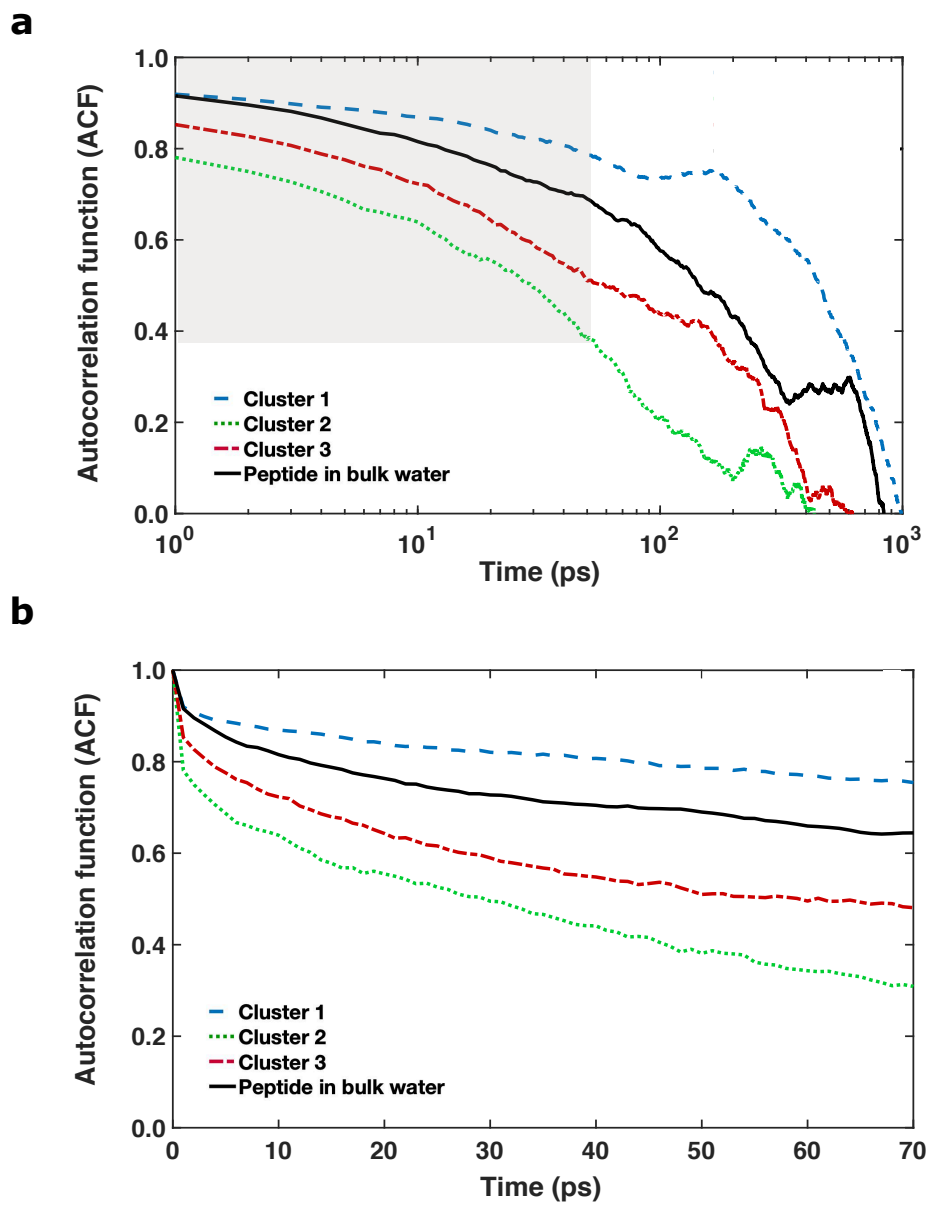
Figure 3-20: Autocorrelation function of cosine of the the angle between two phenyl dipoles in logarithmic (a) and linear scale (b). Panel (b) is a magnified image of the shaded region in panel (a). The last 30 ns of the simulations are used for the calculation of ACF.

3.4 Conclusions and implications on amyloid aggregation

In conclusion, we find that the amyloid beta segment 16-23 exhibits binds irreversibly on the timescale of 10s of nanoseconds to the silica surface. Our study confirms previous findings showing that the binding of the peptide chain to the surface is driven by a combination of both hydrophobic and electrostatic interactions. The binding modes involve a combination of both hydrophobic interactions of the phenylalanine groups as well as polar interactions between the charged parts of the amino acids and the silica surface. We also show that there are a wide diversity of peptide conformations: perpendicular to the surface; bent; and extended flat-on conformation on the surface. Hence, the amorphous silica-water interface alters the conformation of the peptide in a manner that will likely alter processes involving amyloid aggregation.

In this study, we did not look at the aggregation thermodynamics and kinetics near the surface of amorphous silica. However, our single-peptide simulations provide some qualitative insights into the possible mechanisms that might occur. Specifically, whether the single peptide orientation is parallel (conformation viii) or perpendicular to the surface (conformation v), might play an important role in the initial steps of the nucleation process. In Figure 3-21 we show a schematic of the possible effects that these two initial conformations may have on the eventual formation of the fibrils. In the case of conformation (v) shown in the left panel (a,c), we can speculate that this will predominantly lead to parallel beta sheets in the first layer in contact with the silica surface. This is due to the fact that it costs a lot of energy to stabilize the negatively charged termini close to the surface which is required to create an anti parallel beta sheet. On the other hand, for conformation (viii) which lies parallel to the surface, the aggregates in the first layer can involve both parallel and anti-parallel beta sheets. However, the free energy of adsorption should be evaluated and compared for each conformation accordingly. Umbrella sampling and steered MD have already been utilized for this purpose in a similar study [68]. Moreover, the same study used experimental adsorption isotherms to calculate peptide binding constants

and free energy of binding from experiments.

Considering the fact that the aggregation process is computationally expensive, the stability or possible conformational changes of fibrillar aggregates near the silica surface can be further evaluated using the already-formed dimers, tetrameters, octamers, etc. of the same peptide that we used here.

At this point, these ideas remain a conjecture which would be interesting to explore in future simulations and experiments.
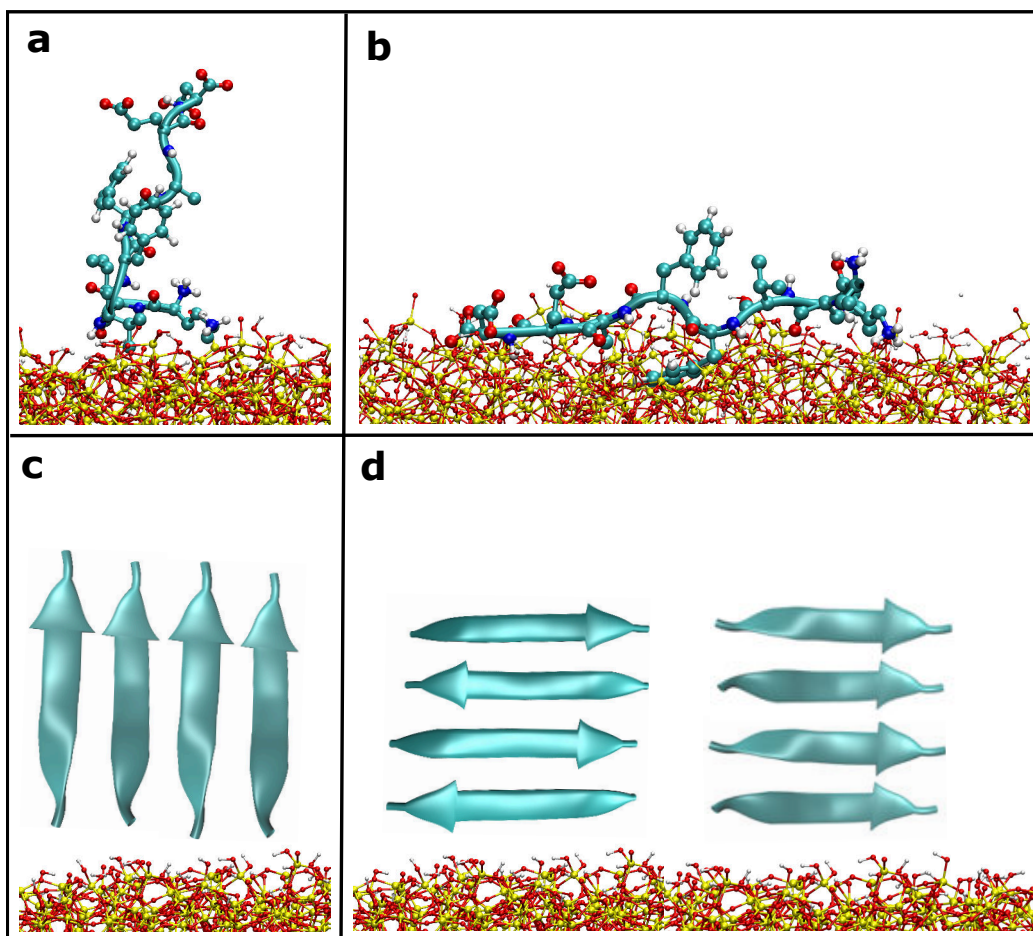
Figure 3-21: (a) Conformation of a monomer corresponding to system (v) (b) Conformation of a monomer corresponding to system (viii) (c) The most likely conformation for vertically aligned peptide aggregations is the parallel beta-sheets. (d) Horizontally aligned peptide aggregations can occur in both parallel and anti parallel beta-sheet forms.

Chapter 4

Conclusions and Suggestions

In this thesis, we applied molecular dynamics simulation to study the interaction of specific biomolecules with two different surfaces: firstly, the interaction of cholesterol and amyloid precursor protein with the cell membrane; secondly, the interaction of the hydrophobic core of amyloid beta peptide with the amorphous silica surface.

In the first part of this thesis, the thermal conductivity of DPPC membrane containing cholesterol at different concentrations and in the presence of amyloid protein was studied. To the best of our knowledge, thermal conductivity values of cholesterol and APP had not been studied so far and there was almost no information about how these components influence heat conduction within the membrane. This study utilized Müller-Plathe reverse nonequilibrium molecular dynamics approach to calculate thermal conductivity of membranes containing cholesterol and APP.

Our results show that the membranes composed of more cholesterol molecules have smaller cross sectional areas than those containing less cholesterol molecules. On the other hand, thermal conductivity is positively correlated with the concentration of cholesterol in the membrane. Therefore, the higher the level of order and molecular packing in the structure of lipid bilayers, the higher the thermal conductivity of the membrane [152]. To find other possible reasons for the enhanced thermal conductivity in membranes containing more cholesterol, we focused on the hydration of phospholipid headgroups in two of our model membranes: one composed of 100% DPPC, and the other composed of 50% DPPC and 50% cholesterol molecules. Radial distribution functions of water molecules near the lipid head groups suggest that the phospholipid

headgroups are more hydrated in the membrane contained 50% cholesterol. The high density of water molecules at the lipid-water interface increases the membrane-water interactions, which can partially compensate for the steep decrease in the local thermal conductivity profile at the lipid-water interface [8].

Furthermore, we extended our model to the membranes with an asymmetric distribution of cholesterol between the two membrane leaflets. According to our results, the thermal conductivity of asymmetric membranes is lower than that of symmetric ones. The asymmetric membranes also revealed a small rectification effect. However, our simulations did not reveal the flip-flop motion of cholesterol molecules between the membrane leaflets, which is reported in the literature. The reason is that the length of our simulations was shorter than the required time to capture a cholesterol flip-flop. To this end, simulations up to some hundreds of nanoseconds are recommended for future work. However, long simulations of large systems rely strongly on the available computational facilities.

Moreover, our simulations with the membranes decorated with amyloid precursor protein show a statistically significant difference between the thermal conductivity coefficients in the forward and backward directions. This leads to a rectification effect when heat flows in opposite directions through the membrane-protein system. We believe that thermal rectification is highly affected by the structure rather than the temperature gradient. However, more studies are needed to support this idea. Therefore, performing simulations at different conditions (at different temperatures) is highly recommended for future work. Furthermore, membrane models with compositions similar to real membranes could provide more realistic results. However, simulations with more complex structures do not necessarily provide better results.

In this study, we did not investigate the finite size effect on the value of thermal conductivity mainly because of the limitation in time and computer resources. It is highly recommended to study the thermal conductivity of bilayers with different sizes as well.

In the second part of this thesis, we studied the behavioral changes of the hydrophobic core of amyloid beta peptide interacting with a silica surface using molecu-

lar dynamics simulations. Our results reveal that in the 10s of nanosecond time scale, the peptide binds to the silica surface and does not detach from the surface during the 50 ns of our simulations.

We found that a combination of hydrophobic interactions of the phenylalanine groups and polar interactions between the charged groups of peptide and the silica surface define the binding modes. Our simulations were carried out at neutral pH in which the silica surface has a moderate surface ionization. According to the previous reports, charged peptides show different behaviors near the silica surfaces with different levels of surface ionization. Therefore, it is highly recommended to repeat the simulation at different levels of surface ionization for future work.

Another recommendation for the future work is to verify the dominant conformation of the peptide on the surface at different salt concentrations which is a determining factor in the adsorption of peptide to the surface. We only considered the physiological pH and salt concentration in all of our simulations, mainly because of the constraints in time and computational facilities. To study the system at different pH values and therefore different surface ionization levels, it is required to apply different salt concentrations to make the whole system neutral. According to the previous studies, at low pH, less dissociated silanol groups are on the silica surface and therefore, a lower salt concentration is required to neutralize the system. This leads to a lower concentration of cations on the silica surface and hence affects the adsorption of the charged peptide.

In this study, we achieved a wide range of peptide conformations, some of which are perpendicular to the surface, some are bent, and some are in an extended form such that the peptide is lying on the surface. The amorphous silica-water interface, thus, changes the peptide's conformation in a way that is likely to modify processes involving amyloid aggregation. Since an adequate sampling of the fibrillation process, which is a slow process and happens in a large system, is still a real challenge at the experimentally relevant timescales of microseconds and milliseconds, it is proposed that future simulations of multimers (starting from a dimer, tetramer, etc.) be carried out to measure the potential structural and dynamical changes in these structures and

to verify their stability near the silica surface.

Bibliography

[1] Bobo Shi, Yun Kyung Shin, Ali A Hassanali, and Sherwin J Singer. DNA binding to the silica surface. *The Journal of Physical Chemistry B*, 119(34):11030–11040, 2015.

[2] Philip L Yeagle. *The membranes of cells*. Academic Press, 2016.

[3] Yifei Qi, Helgi I Ingólfsson, Xi Cheng, Jumin Lee, Siewert J Marrink, and Wonpil Im. CHARMM-GUI martini maker for coarse-grained simulations with the martini force field. *Journal of chemical theory and computation*, 11(9):4486–4494, 2015.

[4] Stuart Humphries. A physical explanation of the temperature dependence of physiological processes mediated by cilia.

[5] Anna B Neuheimer. The pace of life: Time, temperature, and a biological theory of relativity. *bioRxiv*, page 609446, 2019.

[6] Mahdi Ghavami, Meisam Rezaei, Reza Ejtehadi, Mina Lotfi, Mohammad A Shokrgozar, Baharak Abd Emamy, Jens Raush, and Morteza Mahmoudi. Physiological temperature has a crucial role in amyloid beta in the absence and presence of hydrophobic and hydrophilic nanoparticles. *ACS chemical neuroscience*, 4(3):375–378, 2012.

[7] Ana RN Bastos, Carlos DS Brites, Paola A Rojas-Gutierrez, Christine DeWolf, Rute AS Ferreira, John A Capobianco, and Luís D Carlos. Thermal properties of lipid bilayers determined using upconversion nanothermometry. *Advanced Functional Materials*, 29(48):1905474, 2019.

[8] Thomas J Müller and Florian Müller-Plathe. Heat transport through a biological membrane—an asymmetric property? technical issues of nonequilibrium molecular dynamics methods. *International Journal of Quantum Chemistry*, 111(7-8):1403–1418, 2011.

[9] Sina Youssefian, Nima Rahbar, and Steven Van Dessel. Thermal conductivity and rectification in asymmetric archaeal lipid membranes. *The Journal of chemical physics*, 148(17):174901, 2018.

[10] Katherine D Krause, Sandra Roy, and Dennis K Hore. Interplay between adsorbed peptide structure, trapped water, and surface hydrophobicity. *Biointerphases*, 12(2):02D407, 2017.

[11] Li Shi, Deyu Li, Choongho Yu, Wanyoung Jang, Dohyung Kim, Zhen Yao, Philip Kim, and Arunava Majumdar. Measuring thermal and thermoelectric properties of one-dimensional nanostructures using a microfabricated device. *J. Heat Transfer*, 125(5):881–888, 2003.

[12] Clayton R Otey, Wah Tung Lau, Shanhui Fan, et al. Thermal rectification through vacuum. *Physical Review Letters*, 104(15):154301, 2010.

[13] Michael P Allen et al. Introduction to molecular dynamics simulation. *Computational soft matter: from synthetic polymers to proteins*, 23(1):1–28, 2004.

[14] Mohammad Alaghemandi, Elena Algaer, Michael C Böhm, and Florian Müller-Plathe. The thermal conductivity and thermal rectification of carbon nanotubes studied using reverse non-equilibrium molecular dynamics simulations. *Nanotechnology*, 20(11):115704, 2009.

[15] Norbert Attig, Kurt Binder, Helmut Grubmuller, and Kurt Kremer. Computational soft matter: from synthetic polymers to proteins. *NIC Lecture Notes*, 23, 2004.

[16] Sumit Sharma, Pramod Kumar, and Rakesh Chandra. Introduction to molecular dynamics. In *Molecular Dynamics Simulation of Nanocomposites Using BIOVIA Materials Studio, Lammps and Gromacs*, pages 1–38. Elsevier, 2019.

[17] Mark Tuckerman. *Statistical mechanics: theory and molecular simulation*. Oxford university press, 2010.

[18] Herman JC Berendsen, JPM van Postma, Wilfred F van Gunsteren, ARHJ DiNola, and Jan R Haak. Molecular dynamics with coupling to an external bath. *The Journal of chemical physics*, 81(8):3684–3690, 1984.

[19] Shuichi Nosé. A unified formulation of the constant temperature molecular dynamics methods. *The Journal of chemical physics*, 81(1):511–519, 1984.

[20] William G Hoover. Canonical dynamics: Equilibrium phase-space distributions. *Physical review A*, 31(3):1695, 1985.

[21] Richard W Pastor, Bernard R Brooks, and Attila Szabo. An analysis of the accuracy of langevin and molecular dynamics algorithms. *Molecular Physics*, 65(6):1409–1419, 1988.

[22] Michael P Allen and Dominic J Tildesley. *Computer simulation of liquids*. Oxford university press, 2017.

[23] DJ Evans and GP Morriss. Computer phys. rep. 1, 297 (1984). 25 dj evans and gp morris. *Statistical Mechanics of Nonequilibrium Liquids*, 1990.

[24] Billy D Todd and Peter J Daivis. *Nonequilibrium molecular dynamics: theory, algorithms and applications.* Cambridge University Press, 2017.

[25] Florian Müller-Plathe. A simple nonequilibrium molecular dynamics method for calculating the thermal conductivity. *The Journal of chemical physics*, 106(14):6082–6085, 1997.

[26] Alvin C Rencher and MG Schimek. Methods of multivariate analysis. *Computational Statistics*, 12(4):422–422, 1997.

[27] Joe H Ward Jr. Hierarchical grouping to optimize an objective function. *Journal of the American statistical association*, 58(301):236–244, 1963.

[28] David Wishart. 256. note: An algorithm for hierarchical classifications. *Biometrics*, pages 165–170, 1969.

[29] Iseult Lynch and Kenneth A Dawson. Protein-nanoparticle interactions. *Nano today*, 3(1-2):40–47, 2008.

[30] Iseult Lynch, Anna Salvati, and Kenneth A Dawson. Protein-nanoparticle interactions: what does the cell see? *Nature nanotechnology*, 4(9):546, 2009.

[31] Mouzhe Xie, Alexandar L Hansen, Jiaqi Yuan, and Rafael Brüschweiler. Residue-specific interactions of an intrinsically disordered protein with silica nanoparticles and their quantitative prediction. *The Journal of Physical Chemistry C*, 120(42):24463–24468, 2016.

[32] Marion J Limo, Anna Sola-Rabada, Estefania Boix, Veeranjaneyulu Thota, Zayd C Westcott, Valeria Puddu, and Carole C Perry. Interactions between metal oxides and biomolecules: from fundamental understanding to applications. *Chemical reviews*, 118(22):11118–11193, 2018.

[33] Andre E Nel, Lutz Mädler, Darrell Velegol, Tian Xia, Eric MV Hoek, Ponisseril Somasundaran, Fred Klaessig, Vince Castranova, and Mike Thompson. Understanding biophysicochemical interactions at the nano–bio interface. *Nature materials*, 8(7):543, 2009.

[34] Morteza Mahmoudi, Abuelmagd M Abdelmonem, Shahed Behzadi, Joachim H Clement, Silvio Dutz, Mohammad R Ejtehadi, Raimo Hartmann, Karsten Kantner, Uwe Linne, Pauline Maffre, et al. Temperature: the "ignored" factor at the nanobio interface. *ACS nano*, 7(8):6555–6562, 2013.

[35] Mrinmoy De, Partha S Ghosh, and Vincent M Rotello. Applications of nanoparticles in biology. *Advanced Materials*, 20(22):4225–4241, 2008.

[36] Stephen PA Fodor, Richard P Rava, Xiaohua C Huang, Ann C Pease, Christopher P Holmes, and Cynthia L Adams. Multiplexed biochemical assays with biological chips. *Nature*, 364(6437):555–556, 1993.

[37] Bohuslav Rittich and Alena Španová. Spe and purification of DNA using magnetic particles. *Journal of separation science*, 36(15):2472–2485, 2013.

[38] David J Lockhart and Elizabeth A Winzeler. Genomics, gene expression and DNA arrays. *Nature*, 405(6788):827, 2000.

[39] Francois Torney, Brian G Trewyn, Victor S-Y Lin, and Kan Wang. Mesoporous silica nanoparticles deliver DNA and chemicals into plants. *Nature nanotechnology*, 2(5):295, 2007.

[40] Tian Xia, Michael Kovochich, Monty Liong, Huan Meng, Sanaz Kabehie, Saji George, Jeffrey I Zink, and Andre E Nel. Polyethyleneimine coating enhances the cellular uptake of mesoporous silica nanoparticles and allows safe delivery of siRNA and DNA constructs. *ACS nano*, 3(10):3273–3286, 2009.

[41] Yi Xiao, Arica A Lubin, Alan J Heeger, and Kevin W Plaxco. Label-free electronic detection of thrombin in blood serum by using an aptamer-based sensor. *Angewandte Chemie International Edition*, 44(34):5456–5459, 2005.

[42] Carlota Auría-Soro, Tabata Nesma, Pablo Juanes-Velasco, Alicia Landeira-Viñuela, Helena Fidalgo-Gomez, Vanessa Acebes-Fernandez, Rafael Gongora, María Jesus Almendral Parra, Raúl Manzano-Roman, and Manuel Fuentes. Interactions of nanoparticles and biosystems: microenvironment of nanoparticles and biomolecules in nanomedicine. *Nanomaterials*, 9(10):1365, 2019.

[43] Saeed Sadigh-Eteghad, Babak Sabermarouf, Alireza Majdi, Mahnaz Talebi, Mehdi Farhoudi, and Javad Mahmoudi. Amyloid-beta: a crucial factor in alzheimer's disease. *Medical Principles and Practice*, 24(1):1–10, 2015.

[44] Vladimir N Uversky and Yuri Lyubchenko. *Bio-nanoimaging: protein misfolding and aggregation.* Academic Press, 2013.

[45] Luca Bellucci, Albert Ardèvol, Michele Parrinello, Helmut Lutz, Hao Lu, Tobias Weidner, and Stefano Corni. The interaction with gold suppresses fiber-like conformations of the amyloid β (16–22) peptide. *Nanoscale*, 8(16):8737–8748, 2016.

[46] Mahiuddin Ahmed, Judianne Davis, Darryl Aucoin, Takeshi Sato, Shivani Ahuja, Saburo Aimoto, James I Elliott, William E Van Nostrand, and Steven O Smith. Structural conversion of neurotoxic amyloid-β 1–42 oligomers to fibrils. *Nature structural & molecular biology*, 17(5):561, 2010.

[47] Nasrollah Rezaei-Ghaleh, Mehriar Amininasab, Sathish Kumar, Jochen Walter, and Markus Zweckstetter. Phosphorylation modifies the molecular stability of β-amyloid deposits. *Nature communications*, 7:11359, 2016.

[48] Bertrand Morel, Lorena Varela, and Francisco Conejero-Lara. The thermodynamic stability of amyloid fibrils studied by differential scanning calorimetry. *The Journal of Physical Chemistry B*, 114(11):4010–4019, 2010.

[49] Thomas J Paul, Zachary Hoffmann, Congzhou Wang, Maruda Shanmugasundaram, Jason DeJoannis, Alexander Shekhtman, Igor K Lednev, Vamsi K Yadavalli, and Rajeev Prabhakar. Structural and mechanical properties of amyloid beta fibrils: a combined experimental and theoretical approach. *The journal of physical chemistry letters*, 7(14):2758–2764, 2016.

[50] Matthew R Elkins, Tuo Wang, Mimi Nick, Hyunil Jo, Thomas Lemmin, Stanley B Prusiner, William F DeGrado, Jan Stöhr, and Mei Hong. Structural polymorphism of alzheimer's β-amyloid fibrils as controlled by an e22 switch: A solid-state nmr study. *Journal of the American Chemical Society*, 138(31):9840–9852, 2016.

[51] Mouli Konar, Ashwin Mathew, and Swagata Dasgupta. Effect of silica nanoparticles on the amyloid fibrillation of lysozyme. *ACS omega*, 4(1):1015–1026, 2019.

[52] Jarek Dabrowski et al. *Silicon surfaces and formation of interfaces: basic science in the industrial world*. World Scientific, 2000.

[53] Bo Zhang, Mouzhe Xie, Lei Bruschweiler-Li, and Rafael Brüschweiler. Nanoparticle-assisted removal of protein in human serum for metabolomics studies. *Analytical chemistry*, 88(1):1003–1007, 2015.

[54] Alexandre Albanese, Peter S Tang, and Warren CW Chan. The effect of nanoparticle size, shape, and surface chemistry on biological systems. *Annual review of biomedical engineering*, 14:1–16, 2012.

[55] Himadri S Mandal and Heinz-Bernhard Kraatz. Effect of the surface curvature on the secondary structure of peptides adsorbed on nanoparticles. *Journal of the American Chemical Society*, 129(20):6356–6357, 2007.

[56] Carl D Walkey, Jonathan B Olsen, Hongbo Guo, Andrew Emili, and Warren CW Chan. Nanoparticle size and surface chemistry determine serum protein adsorption and macrophage uptake. *Journal of the American Chemical Society*, 134(4):2139–2147, 2012.

[57] Jun Wu, Hongliang Wang, Anna Zhu, and Feng Long. Adsorption kinetics of single-stranded DNA on functional silica surfaces and its influence factors: an evanescent-wave biosensor study. *ACS omega*, 3(5):5605–5614, 2018.

[58] Valeria Puddu and Carole C Perry. Peptide adsorption on silica nanoparticles: evidence of hydrophobic interactions. *ACS nano*, 6(7):6356–6363, 2012.

[59] Kento Imai, Kazunori Shimizu, Mitsuhiro Kamimura, and Hiroyuki Honda. Interaction between porous silica gel microcarriers and peptides for oral administration of functional peptides. *Scientific reports*, 8(1):10971, 2018.

[60] Bhuvnesh Bharti, Jens Meissner, Sabine HL Klapp, and Gerhard H Findenegg. Bridging interactions of proteins with silica nanoparticles: The influence of pH, ionic strength and protein concentration. *Soft Matter*, 10(5):718–728, 2014.

[61] Yajing Kan, Qiyan Tan, Gensheng Wu, Wei Si, and Yunfei Chen. Study of DNA adsorption on mica surfaces using a surface force apparatus. *Scientific reports*, 5:8442, 2015.

[62] Peter E Vandeventer, Jessica S Lin, Theodore J Zwang, Ali Nadim, Malkiat S Johal, and Angelika Niemz. Multiphasic DNA adsorption to silica surfaces under varying buffer, ph, and ionic strength conditions. *The Journal of Physical Chemistry B*, 116(19):5661–5670, 2012.

[63] Siddharth V Patwardhan, Fateme S Emami, Rajiv J Berry, Sharon E Jones, Rajesh R Naik, Olivier Deschaume, Hendrik Heinz, and Carole C Perry. Chemistry of aqueous silica nanoparticle surfaces and the mechanism of selective peptide adsorption. *Journal of the American Chemical Society*, 134(14):6244–6256, 2012.

[64] Ali A Hassanali and Sherwin J Singer. Model for the water- amorphous silica interface: The undissociated surface. *The Journal of Physical Chemistry B*, 111(38):11181–11193, 2007.

[65] Ali A Hassanali, Hui Zhang, Chris Knight, Yun Kyung Shin, and Sherwin J Singer. The dissociated amorphous silica surface: Model development and evaluation. *Journal of chemical theory and computation*, 6(11):3456–3471, 2010.

[66] Bobo Shi, Yun Kyung Shin, Ali A Hassanali, and Sherwin J Singer. Biomolecules at the amorphous silica/water interface: Binding and fluorescence anisotropy of peptides. *Colloids and Surfaces B: Biointerfaces*, 157:83–92, 2017.

[67] Fateme S Emami, Valeria Puddu, Rajiv J Berry, Vikas Varshney, Siddharth V Patwardhan, Carole C Perry, and Hendrik Heinz. Force field and a surface model database for silica to simulate interfacial properties in atomic resolution. *Chemistry of Materials*, 26(8):2647–2658, 2014.

[68] Fateme S Emami, Valeria Puddu, Rajiv J Berry, Vikas Varshney, Siddharth V Patwardhan, Carole C Perry, and Hendrik Heinz. Prediction of specific biomolecule adsorption on silica surfaces as a function of pH and particle size. *Chemistry of Materials*, 26(19):5725–5734, 2014.

[69] Takeshi Harayama and Howard Riezman. Understanding the diversity of membrane lipid composition. *Nature Ecology & Evolution*, pages 1–18, 2018.

[70] Bruce Alberts, Alexander Johnson, Julian Lewis, Martin Raff, Keith Roberts, and Peter Walter. *Molecular Biology of the Cell*, volume 91. Garland Science, New York, 4 edition, 2002.

[71] Harvey Lodish, Arnold Berk, S Lawrence Zipursky, Paul Matsudaira, David Baltimore, and James Darnell. *Molecular cell biology 4th edition*. Freeman & Co., New York, 2000.

[72] Geoffer M Cooper. The cell: a molecular approach 2nd edition, 2000.

[73] Shu-Lin Liu, Ren Sheng, Jae Hun Jung, Li Wang, Ewa Stec, Matthew J O'Connor, Seohyoen Song, Rama Kamesh Bikkavilli, Robert A Winn, Dae-sung Lee, et al. Orthogonal lipid sensors identify transbilayer asymmetry of plasma membrane cholesterol. *Nature chemical biology*, 13(3):268, 2017.

[74] Anna CV Johansson and Erik Lindahl. Protein contents in biological membranes can explain abnormal solvation of charged and polar residues. *Proceedings of the National Academy of Sciences*, 106(37):15684–15689, 2009.

[75] Justin A Lemkul and David R Bevan. A comparative molecular dynamics analysis of the amyloid β-peptide in a lipid bilayer. *Archives of biochemistry and biophysics*, 470(1):54–63, 2008.

[76] Anne M Brown and David R Bevan. Molecular dynamics simulations of amyloid β-peptide (1-42): Tetramer formation and membrane interactions. *Biophysical journal*, 111(5):937–949, 2016.

[77] KD Nadezhdin, OV Bocharova, EV Bocharov, and AS Arseniev. Structural and dynamic study of the transmembrane domain of the amyloid precursor protein. *Acta Naturae*, 3(1 (8)), 2011.

[78] Alexander M Smondyrev and Max L Berkowitz. Structure of dipalmitoylphosphatidylcholine/cholesterol bilayer at low and high cholesterol concentrations: molecular dynamics simulation. *Biophysical Journal*, 77(4):2075–2089, 1999.

[79] Frédérick de Meyer and Berend Smit. Effect of cholesterol on the structure of a phospholipid bilayer. *Proceedings of the National Academy of Sciences*, 106(10):3654–3658, 2009.

[80] Gora M'Baye, Yves Mély, Guy Duportail, and Andrey S Klymchenko. Liquid ordered and gel phases of lipid bilayers: fluorescent probes reveal close fluidity but different hydration. *Biophysical journal*, 95(3):1217–1225, 2008.

[81] Thomas D Pollard, William C Earnshaw, Jennifer Lippincott-Schwartz, and Graham Johnson. *Cell Biology E-Book*. Elsevier Health Sciences, 2016.

[82] Yvonne Lange and James M Slayton. Interaction of cholesterol and lysophosphatidylcholine in determining red cell shape. *Journal of lipid research*, 23(8):1121–1127, 1982.

[83] Meimei Zhang, Enrico Lussetti, Luís ES de Souza, and Florian Müller-Plathe. Thermal conductivities of molecular liquids by reverse nonequilibrium molecular dynamics. *The Journal of Physical Chemistry B*, 109(31):15060–15067, 2005.

[84] Svend-Age Biehs, Philippe Ben-Abdallah, and FS Rosa. Nanoscale radiative heat transfer and its applications. *Infrared Radiation*, pages 1–26, 2012.

[85] Liang Zhu. Heat transfer applications in biological systems. *Biomedical engineering & design handbook*, 1:2–33, 2009.

[86] ME Bravo, P De Jesús Sánchez, RO Vargas Aguilar, and AE Chávez. Heat transfer in biological tissues. In *Selected Topics of Computational and Experimental Fluid Mechanics*, pages 313–320. Springer, 2015.

[87] Byoung Kyoo Park, Namwoo Yi, Jaesung Park, and Dongsik Kim. Thermal conductivity of single biological cells and relation with cell viability. *Applied Physics Letters*, 102(20):203702, 2013.

[88] Rami T ElAfandy, Ayman F AbuElela, Pawan Mishra, Bilal Janjua, Hassan M Oubei, Ulrich Büttner, Mohammed A Majid, Tien Khee Ng, Jasmeen S Merzaban, and Boon S Ooi. Nanomembrane-based, thermal-transport biosensor for living cells. *Small*, 13(7):1603080, 2017.

[89] Byoung Kyoo Park, Yunho Woo, Dayeong Jeong, Jaesung Park, Tae-Youl Choi, Denise Perry Simmons, Jeonghong Ha, and Dongsik Kim. Thermal conductivity of biological cells at cellular level and correlation with disease state. *Journal of Applied Physics*, 119(22):224701, 2016.

[90] Takahiro Okabe, Taku Fujimura, Junnosuke Okajima, Yumi Kambayashi, Setsuya Aiba, and Shigenao Maruyama. First-in-human clinical study of novel technique to diagnose malignant melanoma via thermal conductivity measurements. *Scientific reports*, 9(1):1–7, 2019.

[91] Guillaume Baffou and Romain Quidant. Thermo-plasmonics: using metallic nanostructures as nano-sources of heat. *Laser & Photonics Reviews*, 7(2):171–187, 2013.

[92] Takeo Nakano, Gota Kikugawa, and Taku Ohara. A molecular dynamics study on heat conduction characteristics in DPPC lipid bilayer. *The Journal of chemical physics*, 133(15):154705, 2010.

[93] Takeo Nakano, Gota Kikugawa, and Taku Ohara. Molecular heat transfer in lipid bilayers with symmetric and asymmetric tail chains. *Journal of Heat Transfer*, 135(6):061301, 2013.

[94] Dipti Potdar and Maria Sammalkorpi. Asymmetric heat transfer from nanoparticles in lipid bilayers. *Chemical Physics*, 463:22–29, 2015.

[95] Chih Wei Chang, D Okawa, A Majumdar, and A Zettl. Solid-state thermal rectifier. *Science*, 314(5802):1121–1124, 2006.

[96] Nick A Roberts and DG Walker. A review of thermal rectification observations and models in solid materials. *International Journal of Thermal Sciences*, 50(5):648–662, 2011.

[97] Teng Zhang and Tengfei Luo. Giant thermal rectification from polyethylene nanofiber thermal diodes. *Small*, 11(36):4657–4665, 2015.

[98] Chauncey Starr. The copper oxide rectifier. *Physics*, 7(1):15–19, 1936.

[99] Mikhail A Lomize, Andrei L Lomize, Irina D Pogozheva, and Henry I Mosberg. OPM: orientations of proteins in membranes database. *Bioinformatics*, 22(5):623–625, 2006.

[100] Thomas H Schmidt and Christian Kandt. LAMBADA and InflateGRO2: efficient membrane alignment and insertion of membrane proteins for molecular dynamics simulations. *Journal of chemical information and modeling*, 52(10):2657–2669, 2012.

[101] Sunhwan Jo, Taehoon Kim, and Wonpil Im. Automated builder and database of protein/membrane complexes for molecular dynamics simulations. *PloS one*, 2(9):e880, 2007.

[102] Sunhwan Jo, Taehoon Kim, Vidyashankara G Iyer, and Wonpil Im. CHARMM-GUI: a web-based graphical user interface for CHARMM. *Journal of computational chemistry*, 29(11):1859–1865, 2008.

[103] Sina Youssefian, Nima Rahbar, Christopher R Lambert, and Steven Van Dessel. Variation of thermal conductivity of DPPC lipid bilayer membranes around the phase transition temperature. *Journal of the Royal Society Interface*, 14(130):20170127, 2017.

[104] S Phimpton. Fast parallel algorithms for short-range molecular dynamics [J]. *Journal of Computational Physics*, 117(1):1–19, 1995.

[105] Alex D MacKerell Jr, Donald Bashford, MLDR Bellott, Roland Leslie Dunbrack Jr, Jeffrey D Evanseck, Martin J Field, Stefan Fischer, Jiali Gao, H Guo, Sookhee Ha, et al. All-atom empirical potential for molecular modeling and dynamics studies of proteins. *The journal of physical chemistry B*, 102(18):3586–3616, 1998.

[106] Robert B Best, Xiao Zhu, Jihyun Shim, Pedro EM Lopes, Jeetain Mittal, Michael Feig, and Alexander D MacKerell Jr. Optimization of the additive CHARMM all-atom protein force field targeting improved sampling of the backbone ϕ, ψ and side-chain $\chi 1$ and $\chi 2$ dihedral angles. *Journal of chemical theory and computation*, 8(9):3257–3273, 2012.

[107] William L Jorgensen, Jayaraman Chandrasekhar, Jeffry D Madura, Roger W Impey, and Michael L Klein. Comparison of simple potential functions for simulating liquid water. *The Journal of chemical physics*, 79(2):926–935, 1983.

[108] Yijin Mao and Yuwen Zhang. Thermal conductivity, shear viscosity and specific heat of rigid water models. *Chemical Physics Letters*, 542:37–41, 2012.

[109] Paul J Barrett, Yuanli Song, Wade D Van Horn, Eric J Hustedt, Johanna M Schafer, Arina Hadziselimovic, Andrew J Beel, and Charles R Sanders. The amyloid precursor protein has a flexible transmembrane domain and binds cholesterol. *Science*, 336(6085):1168–1171, 2012.

[110] Helen M Berman, John Westbrook, Zukang Feng, Gary Gilliland, Talapady N Bhat, Helge Weissig, Ilya N Shindyalov, and Philip E Bourne. The protein data bank. *Nucleic acids research*, 28(1):235–242, 2000.

[111] Helen Berman, Kim Henrick, and Haruki Nakamura. Announcing the worldwide protein data bank. *Nature Structural & Molecular Biology*, 10(12):980, 2003.

[112] Mikhail A Lomize, Irina D Pogozheva, Hyeon Joo, Henry I Mosberg, and Andrei L Lomize. OPM database and PPM web server: resources for positioning of proteins in membranes. *Nucleic acids research*, 40(D1):D370–D376, 2011.

[113] Andrew I Jewett, Zhuoyun Zhuang, and Joan-Emma Shea. Moltemplate a coarse-grained model assembly tool. *Biophysical Journal*, 104(2):169a, 2013.

[114] John R Silvius. Thermotropic phase transitions of pure lipids in model membranes and their modifications by membrane proteins. *Lipid-protein interactions*, 2:239–281, 1982.

[115] Glenn J Martyna, Michael L Klein, and Mark Tuckerman. Nosé–hoover chains: The canonical ensemble via continuous dynamics. *The Journal of chemical physics*, 97(4):2635–2643, 1992.

[116] Alan Grossfield and Daniel M Zuckerman. Quantifying uncertainty and sampling quality in biomolecular simulations. *Annual reports in computational chemistry*, 5:23–48, 2009.

[117] Henrik Flyvbjerg and Henrik Gordon Petersen. Error estimates on averages of correlated data. *The Journal of Chemical Physics*, 91(1):461–466, 1989.

[118] Harden M McConnell and Arun Radhakrishnan. Condensed complexes of cholesterol and phospholipids. *Biochimica et Biophysica Acta (BBA)-Biomembranes*, 1610(2):159–173, 2003.

[119] Gerald W Stockton and Ian CP Smith. A deuterium nuclear magnetic resonance study of the condensing effect of cholesterol on egg phosphatidylcholine bilayer membranes. i. perdeuterated fatty acid probes. *Chemistry and physics of lipids*, 17(2-3):251–263, 1976.

[120] Frank A Nezil and Myer Bloom. Combined influence of cholesterol and synthetic amphiphillic peptides upon bilayer thickness in model membranes. *Biophysical journal*, 61(5):1176–1183, 1992.

[121] Akihiro Kusumi, Witold K Subczynski, Marta Pasenkiewicz-Gierula, James S Hyde, and Hellmut Merkle. Spin-label studies on phosphatidylcholine-cholesterol membranes: effects of alkyl chain length and unsaturation in the fluid phase. *Biochimica et Biophysica Acta (BBA)-Biomembranes*, 854(2):307–317, 1986.

[122] Helgi I Ingólfsson, Manuel N Melo, Floris J Van Eerden, Clement Arnarez, Cesar A Lopez, Tsjerk A Wassenaar, Xavier Periole, Alex H De Vries, D Peter Tieleman, and Siewert J Marrink. Lipid organization of the plasma membrane. *Journal of the american chemical society*, 136(41):14554–14559, 2014.

[123] Semen O Yesylevskyy and Alexander P Demchenko. How cholesterol is distributed between monolayers in asymmetric lipid membranes. *European biophysics journal*, 41(12):1043–1054, 2012.

[124] James W Carter, Miguel Angel Gonzalez, Nicholas Jan Brooks, John Seddon, and Fernando Bresme. Flip-flop asymmetry of cholesterol in model membranes induced by thermal gradients. *Soft Matter*, 2020.

[125] Santanu Bhattacharya and Saubhik Haldar. Interactions between cholesterol and lipids in bilayer membranes. role of lipid headgroup and hydrocarbon chain–backbone linkage. *Biochimica et Biophysica Acta (BBA)-Biomembranes*, 1467(1):39–53, 2000.

[126] Yoshiki Ishii, Keisuke Sato, Mathieu Salanne, Paul A Madden, and Norikazu Ohtori. Thermal conductivity of simple liquids: Origin of temperature and packing fraction dependences. *The Journal of Chemical Physics*, 140(11):114502, 2014.

[127] John D Weeks, David Chandler, and Hans C Andersen. Role of repulsive forces in determining the equilibrium structure of simple liquids. *The Journal of chemical physics*, 54(12):5237–5247, 1971.

[128] Jiuning Hu, Xiulin Ruan, and Yong P Chen. Thermal conductivity and thermal rectification in graphene nanoribbons: a molecular dynamics study. *Nano letters*, 9(7):2730–2735, 2009.

[129] GC Loh, Edwin Hang Tong Teo, and Beng Kang Tay. Thermal rectification reversal in carbon nanotubes. *Journal of Applied Physics*, 112(10):103515, 2012.

[130] Görkem Eskiizmir, Yasemin Baskın, and Kerim Yapıcı. Graphene-based nanomaterials in cancer treatment and diagnosis. In *Fullerens, Graphenes and Nanotubes*, pages 331–374. Elsevier, 2018.

[131] Jiaojiao Hu, Huiyong Sun, Haiping Hao, and Qiuling Zheng. Prediction of fibril formation by early-stage amyloid peptide aggregation. *Journal of pharmaceutical analysis*, 10(2):194–199, 2020.

[132] Gianvito Grasso and Andrea Danani. Molecular simulations of amyloid beta assemblies. *Advances in Physics: X*, 5(1):1770627, 2020.

[133] H Bekker, HJC Berendsen, EW DIJKSTRA, S Achterop, Rudi van Drunen, D der Spoel, H BEKKER, EJ Dijkstra, D Van Der Spoel, A Sijbers, et al. Gromacs: A parallel computer for molecular dynamics simulations. 1993.

[134] Herman JC Berendsen, David van der Spoel, and Rudi van Drunen. GRO-MACS: a message-passing parallel molecular dynamics implementation. *Computer physics communications*, 91(1-3):43–56, 1995.

[135] Erik Lindahl, Berk Hess, and David Van Der Spoel. GROMACS 3.0: a package for molecular simulation and trajectory analysis. *Molecular modeling annual*, 7(8):306–317, 2001.

[136] David Van Der Spoel, Erik Lindahl, Berk Hess, Gerrit Groenhof, Alan E Mark, and Herman JC Berendsen. GROMACS: fast, flexible, and free. *Journal of computational chemistry*, 26(16):1701–1718, 2005.

[137] WF Van Gunsteren, SR Billeter, AA Eising, PH Hunenberger, PKHC Krüger, AE Mark, WRP Scott, IG Tironi, PH Hünenberger, PH Huenenberger, et al. The GROMOS96 manual and user guide. 1996.

[138] Xavier Daura, Alan E Mark, and Wilfred F Van Gunsteren. Parametrization of aliphatic chn united atoms of GROMOS96 force field. *Journal of computational chemistry*, 19(5):535–547, 1998.

[139] HJC Berendsen, JR Grigera, and TP Straatsma. The missing term in effective pair potentials. *Journal of Physical Chemistry*, 91(24):6269–6271, 1987.

[140] RW Hockney, SP Goel, and JW Eastwood. Quiet high-resolution computer models of a plasma. *Journal of Computational Physics*, 14(2):148–158, 1974.

[141] Tom Darden, Darrin York, and Lee Pedersen. Particle mesh ewald: An n· log (n) method for ewald sums in large systems. *The Journal of chemical physics*, 98(12):10089–10092, 1993.

[142] Ulrich Essmann, Lalith Perera, Max L Berkowitz, Tom Darden, Hsing Lee, and Lee G Pedersen. A smooth particle mesh ewald method. *The Journal of chemical physics*, 103(19):8577–8593, 1995.

[143] Giovanni Bussi, Davide Donadio, and Michele Parrinello. Canonical sampling through velocity rescaling. *The Journal of chemical physics*, 126(1):014101, 2007.

[144] Kusai A Merchant, Robert B Best, John M Louis, Irina V Gopich, and William A Eaton. Characterizing the unfolded states of proteins using single-molecule fret spectroscopy and molecular simulations. *Proceedings of the National Academy of Sciences*, 104(5):1528–1533, 2007.

[145] Nicholas Sherck, Thomas Webber, Dennis Robinson Brown, Timothy Keller, Mikayla Barry, Audra DeStefano, Sally Jiao, Rachel A Segalman, Glenn H Fredrickson, M Scott Shell, et al. End-to-end distance probability distributions of dilute poly (ethylene oxide) in aqueous solution. *Journal of the American Chemical Society*, 142(46):19631–19641, 2020.

[146] Lewis J Martin, Behnam Akhavan, and Marcela MM Bilek. Electric fields control the orientation of peptides irreversibly immobilized on radical-functionalized surfaces. *Nature communications*, 9(1):1–11, 2018.

[147] Lauren H Kapcha and Peter J Rossky. A simple atomic-level hydrophobicity scale reveals protein interfacial structure. *Journal of molecular biology*, 426(2):484–498, 2014.

[148] Fujian Huang and Haojun Liang. Adsorption behaviors of DNA/cation complexes on amino and silica chip surfaces: a dual polarization interferometry study. *ACS applied materials & interfaces*, 5(11):5025–5033, 2013.

[149] Derya Kapusuz and Caner Durucan. Exploring encapsulation mechanism of DNA and mononucleotides in sol-gel derived silica. *Journal of biomaterials applications*, 32(1):114–125, 2017.

[150] Ali A. Hassanali, Tanping Li, Dongping Zhong, and Sherwin J. Singer. A molecular dynamics study of lys-trp-lys: structure and dynamics in solution following photoexcitation. *The Journal of Physical Chemistry B*, 110(21):10497–10508, 2006. PMID: 16722759.

[151] Bradley Moores, Elizabeth Drolle, Simon J Attwood, Janet Simons, and Zoya Leonenko. Effect of surfaces on amyloid fibril formation. *PLoS One*, 6(10), 2011.

[152] Neda Rafieiolhosseini and Mohammad Reza Ejtehadi. Thermal conductivity of the cell membrane in the presence of cholesterol and amyloid precursor protein. *Physical Review E*, 102(4):042401, 2020.

Appendix A

Computational Part 1

Simulations of membrane and membrane-protein systems were performed on a system with 24 MPI threads with the benchmark time of 0.75 ns per day.

LAMMPS Run Input File:

———

```
timestep 1
neighbor 2 bin
neigh_modify delay 5 every 1
velocity all zero linear
compute ke all ke/atom
variable temp atom c_ke/1.5/0.0019858775
compute layers all chunk/atom bin/1d z lower 0.01 units reduced
fix 1 all nve
fix 2 all ave/chunk 10 100 1000 layers v_temp density/mass file tmpdens.profile
fix 3 all thermal/conductivity 100 z 100
variable tdiff equal f_2[51][3]-f_2[1][3]
thermo 1000
thermo_style custom step time temp xlo xhi ylo yhi zlo zhi epair etotal pe ke ebond
eangle edihed eimp evdwl ecoul elong vol press density f_3 v_tdiff
thermo_modify flush yes
dump 1 all dcd 10000 nemd.dcd
dump_modify 1 unwrap yes
dump 2 all custom 10000 nemd.dump id type x y z vx vy vz ix iy iz
dump_modify 2 append yes
write_data nemd.data
run 20000000
```

Appendix B

Computational Part 2

Simulations of silica-peptide system were performed on a system with 48 nodes and the benchmark time of 8.88 ns per day.

GROMACS Run Input File:

———

constraints = none

constraint_algorithm = LINCS

lincs_order = 4

lincs_iter = 1

lincs_warnangle = 30

integrator = md

emstep = 0.0001

emtol = 50.0

comm_mode = none;

comm_grps = system;

nstcomm = 10

dt = 0.001 nsteps = 50000000

nstxout = 10000

nstvout = 10000

nstfout = 0

nstlog = 10000

nstenergy = 10000

nstxtcout = 10000

cutoff-scheme = group

nstlist = 10

ns_type = grid

pbc = xyz

periodic_molecules = no

rlist = 1
rlistlong = 1
rcoulomb = 1
coulombtype = PME
epsilon_r = 1
vdwtype = user
rvdw = 1
DispCorr = no
energygrps = LYS LEU VAL PHE1 PHE2 ALA GLU ASP NaB ClB OXB OSil OGem
OMB SIB SiSil SiGem HSil HGem OW HW
energygrp_table = NaB OXB NaB OSil NaB OGem NaB OMB OMB OW OW SIB
OW SiSil OW SiGem OW HSil OW HGem HW OMB HW OXB OW OSil OW OGem
HW OSil HW OGem OXB OW
freezegrps = SIB OXB OMB SiSil OSil SiGem OGem
freezedim = Y Y Y Y Y Y Y Y Y Y Y Y Y Y Y Y Y Y Y Y Y Y Y
Tcoupl = v-rescale
tau_t = 0.3
tc-grps = System
ref_t = 300.0
Pcoupl = no
tau_p = 4
pcoupltype = anisotropic
compressibility = 10.e-5 10.e-5 10.e-5 0.0 0.0 0.0
ref_p = 1.0 1.0 1.0 0.0 0.0 0.0
gen_vel = yes
gen_temp = 300.0
gen_seed = 173529

به نام خدا

پژوهشگاه دانش های بنیادی

(مرکز تحقیقات فیزیک نظری و ریاضیات)

پژوهشکده علوم نانو

پایان نامه دکتری

مطالعه هدایت گرمایی آمیلویید بتا در سطوح آلی به روش شبیه‌سازی دینامیک مولکولی

نویسنده
ندا رفیعی الحسینی

استاد راهنما
پروفسور محمدرضا اجتهادی

استاد مشاور
دکتر علی حسنعلی

بهمن ۱۳۹۹

مقدمه

برهم‌کنش مولکول‌های زیستی و سطوح به علت کاربردهای فراوان همواره مورد توجه بسیاری قرار گرفته است. نیاز روزافزون به استفاده از نانوذرات در صنعت و پزشکی از دلایل توجه به این موضوع می‌باشد [۳۵-۴۱]. در این مطالعه رفتار مولکول‌های زیستی را در مجاورت دو نمونه از سطوح آلی و غیرآلی بررسی می‌کنیم. ابتدا پروتیین آمیلویید را در تعامل با غشای سلولی و سپس در مجاورت سطح سیلیکا قرار می‌دهیم. در ادامه به اختصار به معرفی هر یک از این سیستم‌ها می‌پردازیم.

برهم‌کنش پروتیین‌ها و غشای سلولی

نمونه‌ای از اثر متقابل سطوح آلی و مولکول‌های زیستی را می‌توان در برهم‌کنش بین غشای سلول و پروتیین‌ها مشاهده نمود. پروتیین‌های موجود در غشای سلول به شیوه‌های متعددی با غشا در تعامل هستند. آن‌ها از یک سو می‌توانند باعث بروز ناهنجاری‌هایی در غشا شوند و از سوی دیگر از غشا تاثیر می‌پذیرند. به عنوان مثال، ساختار پروتیین‌های موجود در غشا تحت تاثیر ضخامت غشا تغییر می‌کند. پروتیین‌های موجود در غشا به دو دسته‌ی اصلی تقسیم می‌شوند: پروتیین‌های محیطی (peripheral membrane proteins) که بر روی سطح غشا قرار گرفته و پروتیین‌های جدایی‌ناپذیر (integral membrane proteins) که در عرض غشا جای دارند [۲و۷۱و۷۴] . پروتیین پیش ساز آمیلویید (amyloid precursor protein) نمونه‌ای از این پروتیین‌ها است [۷۵و ۷۶]. بیش از نیمی از جهش‌های مربوط به بیماری آلزایمر در بخشی از این پروتیین رخ می‌دهد که در عرض غشا قرار می‌گیرد [۷۷].

پروتیین آمیلویید بتا

پروتیین آمیلویید بتا که از ۴۲ اسید آمینه تشکیل شده است دارای یک هسته‌ی آب‌گریز (اسیدهای آمینه شماره‌ی ۱۶ تا ۲۳) می‌باشد و در ایجاد توده‌ی آمیلویید بتا نقش مهمی ایفا می‌کند [۶و ۴۵]. آمیلویید بتا به شکل‌های ساختاری متفاوتی ظاهر می‌شود که هر یک از نظر پایداری و میزان سمیت با دیگری متفاوت است. از آن بین می‌توان به الیگومرها (oligomers)، پروتوفیبریل‌ها (protofibrils) و فیبریل‌ها (fibrils) اشاره کرد [۴۴و ۴۶و۴۷]. فیبریل‌های آمیلویید در اثر تجمع نوعی پروتیین به شکل ساختارهای صفحه‌ای بتا (beta sheets) به وجود می‌آیند و مشخصه‌ی بسیاری از بیماری‌های زوال مغز از جمله آلزایمر

(Alzheimer) و بیماری هانتینگتن (Huntington) می‌باشند [۴۴]. الیگومرها که در فرآیند تشکیل فیبریل در محلول پدید می‌آیند، نیز سمی هستند و به غشای سلول‌ها آسیب می‌رسانند.

غشای سلول

غشای سلول که فضای داخل سلولی را از فضای خارج آن جدا می‌کند، علاوه بر کنترل ورود و خروج مواد و تنظیم سوخت و ساز سلول، نقش مهمی در انتقال گرما بین بخش‌های داخلی و خارجی سلول نیز بر عهده دارد. اجزای اصلی تشکیل دهنده‌ی غشای سلول که عمدتا لیپیدها و پروتیین‌ها هستند از طریق نیروهای غیرکوالانسی در کنار یکدیگر قرار گرفته و غشایی انعطاف‌پذیر را به وجود آورده‌اند [۲]. اگرچه همه‌ی غشاهای سلولی یک لایه‌ی متشکل از لیپیدها، پروتیین‌ها و کربوهیدرات‌ها هستند، درصد هر یک از این اجزا در غشای سلول‌های مختلف متفاوت است [۷۰]. اگرچه غشا از سه نوع لیپید مختلف شامل فسفولیپید (phospholipid)، گلیکولیپید (glycolipid) و استرول (sterol) تشکیل شده‌است، بخش عمده‌ی بسیاری از غشاها را فسفولیپیدها تشکیل می‌دهند [۷۱]. فسفولیپیدها از یک مولکول گلیسرول، دو رشته‌ی غیرقطبی (اسیدهای چرب) در انتها و یک سر قطبی شامل گروه فسفات با بار منفی تشکیل شده‌اند. شکل ۱ ساختار شیمیایی یک فسفولیپید به نام فسفاتیدیل کولین (phosphatidylcholine) را نشان می‌دهد. به علت آبدوست بودن سر و آبگریز بودن دم فسفولیپیدها، این مولکول‌ها در محیط‌های آبی تشکیل مایسل (micell) می‌دهند. در غشای سلول‌های حیوانی، چهار نوع فسفولیپید مختلف به نام‌های فسفاتیدیل‌کولین (phosphatidylcholine)، فسفاتیدیل اتانول آمین (phosphatidylethanolamine)، فسفاتیدیل سرین (phosphatidylserine) و اسفینگومایلین (sphingomyelin) یافت می‌شود. توزیع فسفولیپیدها در دو لایه‌ی داخلی و خارجی غشا یکسان نیست.
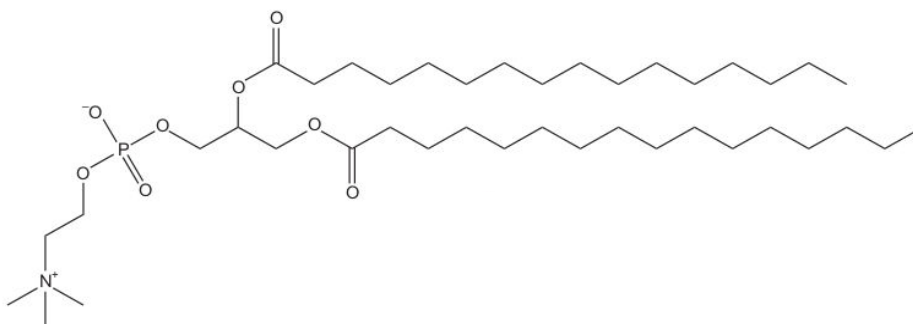

شکل ۱: ساختار شیمیایی فسفاتیدیل کولین (اتخاذ شده از مرجع ۲)

همان‌طور که شکل۲ نشان می‌دهد، فسفاتیدیل اتانول آمین و فسفاتیدیل سرین عمدتا در لایه‌ی داخلی غشا یافت می‌شوند، در حالی که میزان فسفاتیدیل کولین و اسفینگومایلین در لایه‌ی خارجی غشا بیشتر از لایه‌ی داخلی است. این شکل نشان می‌دهد که در بسیاری از غشاها میزان کلسترول در هر دو لایه‌ی غشا تقریبا برابر است. کلسترول که متداول‌ترین استرول موجود در سلول‌های حیوانی است نیز همانند بسیاری از لیپیدها دارای یک سر آب دوست و یک سر آب گریز می‌باشد. همان طور که شکل ۳ نشان می‌دهد، کلسترول از یک گروه هیدروکسیل (که سر قطبی آن را تشکیل می‌دهد)، یک بدنه شامل چهار حلقه‌ی به هم چسبیده و یک زنجیره‌ی هیدروکربنی (که دم آب‌گریز آن محسوب می‌شود) تشکیل می‌شود.
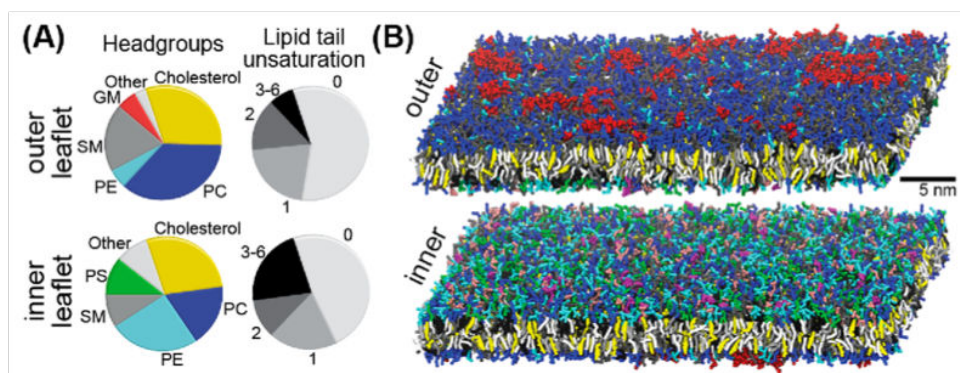
شکل ۲: توزیع نامتقارن لیپیدها در دو لایه‌ی غشا (اتخاذ شده از مرجع ۳)
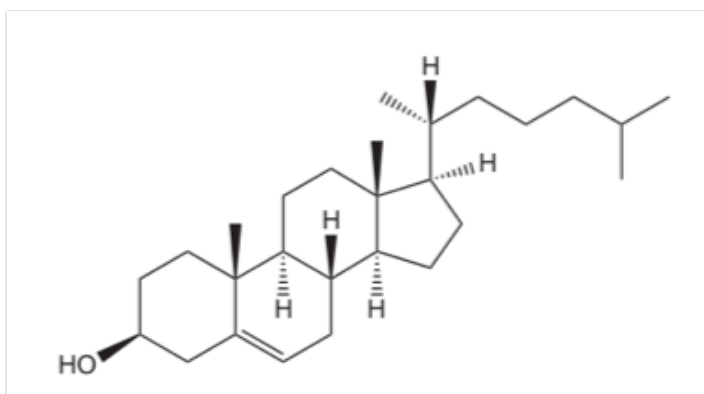
شکل ۳: ساختار شیمیایی مولکول کلسترول (اتخاذ شده از مرجع ۲)

برهم‌کنش بین مولکول‌های زیستی و غشای سلول می‌تواند منجر به تغییر برخی ویژگی‌های غشا گردد. به عنوان مثال، سختی (rigidity) غشا به غلظت کلسترول موجود در آن وابسته است. مطالعات بسیاری نیز به اثر سخت‌شدگی غشای سلول (condensation effect) در اثر افزایش کلسترول در آن اشاره کرده‌اند [۷۸و۷۹]. سخت‌شدگی به مفهوم کاهش سطح مقطع غشا به میزانی کمتر از مقدار میانگین وزن‌دار سطح مقطع هر یک از اجزا می‌باشد [۷۹]. دلیل اصلی این موضوع را می‌توان برهم‌کنش کلسترول با لیپیدها و

تشکیل پیوندهای هیدروژنی با آنها دانست که در نتیجهی آن فضای خالی بین لیپیدها در غشای سلول پر میشود. کلسترول همچنین باعث کاهش نفوذپذیری غشا و انعطافپذیری ساختاری پروتیینهای موجود در آن میشود [۸۰]. حضور کلسترول در غشا سبب اختلال در گذار فاز فسفولیپیدهای اشباع شده نیز میگردد [۸۱]. اگر غلظت کلسترول در غشا کمتر از ۲۵٪ باشد، غشا در یکی از فازهای بینظم (liquid-disordered) و یا منظم (solid-ordered) یافت میشود؛ اما در غلظتهای بالاتر کلسترول، غشا همواره در یک فاز بوده و گذار فازی وجود ندارد. بر اساس شواهد موجود، تاثیر کلسترول بر غشای سلول وابسته به دما است. در دماهای بالاتر از دمای گذار فاز لیپید، افزایش کلسترول در غشا سبب افزایش نظم موجود در آن میشود. این در حالی است که اگر لیپیدهای غشا در دمای پایینتر از دمای گذار فاز خود باشند، افزایش کلسترول سبب از بین رفتن نظم موجود در غشا میگردد.

از دیگر ویژگیهای مهم غشا میتوان به هدایت گرمایی آن اشاره کرد که به دلیل کاربردهای تشخیصی فراوان، مورد توجه بسیاری قرار گرفته است. در یکی از مطالعات انجام شده در این زمینه، هدایت گرمایی دو نوع سلول به روش تجربی اندازهگیری شده است [۸۷]. درهمان مطالعه، هدایت گرمایی سلولهای مرده (صرف نظر از نوع سلول) حدود ۶٪ تا ۱۳٪ بیشتر از هدایت گرمایی سلولهای زنده گزارش شده است. مطالعهی دیگری نیز نشان میدهد که اختلاف ضرایب هدایت گرمایی در سلولهای سالم و بیمار از نظر آماری معنیدار بوده است [۸۹]. نتایج به دست آمده از مطالعات دیگر نشان میدهند که هدایت گرمایی غشا میتواند در تشخیص زودهنگام سرطان پوست مفید واقع شود [۹۰]. همچنین، برای تولید موادی از قبیل نانوذرات مورد استفاده در روشهای درمانی جدید به درک درستی از هدایت گرمایی غشا نیاز است. به عنوان مثال، در یکی از روشهای انتخابی درمان سرطان از نوعی نانوذرهی فلزی استفاده میشود که پس از قرار گرفتن در معرض تابش در داخل بافت گرما تولید میکند. گرمای تولید شده از طریق غشای سلولی به سلولهای مجاور انتقال مییابد [۹۱]. به منظور تنظیم پارامترهای منبع تابشی و برای دستیابی به بازدهی مناسب، به درک درستی از رسانایی و مقاومت گرمایی غشای سلول نیاز است. بنابر اطلاع نویسنده، هدایت گرمایی غشای سلول تا قبل از سال ۲۰۱۹ به روش تجربی اندازهگیری نشده بود. در یکی از مطالعات اخیر، آزمایشگرها هدایت گرمایی غشا را با استفاده از روش گرماسنجی لومینسانس(luminescence thermometry) اندازهگیری کردند [۷]. بدین ترتیب که نانوذرات پوشیده شده با غشای سلول در یک محیط آبی غوطه ور میشوند. دمای محیط آبی نیز توسط یک دماسنج اندازه گیری میشود. سپس با استفاده ازاختلاف دمای بین نانوذرات و محیط آبی، هدایت گرمایی غشای واسط محاسبه میگردد. اگرچه تا قبل از مطالعهی نام برده، هدایت گرمایی غشای سلول به روش تجربی اندازهگیری نشده بود، روشهای محاسباتی متعددی برای محاسبهی این ویژگی توسعه یافته و مورد استفاده قرار گرفته بود. الگوریتمی که اولین بار توسط مولر (Müller) توسعه یافت [۲۵]، در محاسبهی هدایت گرمایی غشای سلول به روش شبیهسازی دینامیک مولکولی غیرتعادلی (nonequilibrium

molecular dynamics) به کار رفت [۸]. نتایج حاصل از مطالعهی مولر نشان میدهد که پروفایل هدایت گرمایی غشا نامتقارن بوده و هدایت گرمایی در ناحیهی بین دو لایهی غشا به مقدار کمینهی خود میرسد. علت مقاومت گرمایی در این ناحیه را میتوان عدم وجود پیوندهای کوالانسی دانست [۹۲]. مطالعات دیگر نیز عدم تقارن در هدایت گرمایی غشا و گسستگی آن در ناحیهی بین دو لایهی غشا را تایید کردهاند [۹۳ و۹۴]. در مطالعهی دیگری نیز از شبیهسازی دینامیک مولکولی غیرتعادلی برای محاسبهی هدایت گرمایی و یکسوسازی آن در غشای نامتقارن آرکائیالها (archaeal) استفاده شده است [۹].

سیلیکا و ویژگیهای آن

در بین نانوذرات گوناگون، سیلیکا (دی اکسید سیلیکون) به دلیل ویژگیهای خاصی همچون قیمت پایین، سمیت کم و زیست سازگاری بالا مورد توجه بسیاری قرار گرفته است. مطالعات پیشین نشان میدهند که نانوذرات سیلیکا میتوانند رفتار ملکولهای زیستی اطراف خود را تحت تاثیر قرار دهند. این تاثیر بسته به سایز نانوذرات، میزان انحنا، بار سطحی، ساختار شیمیایی سطح و همچنین نوع گروههای موجود روی سطح آنها متفاوت میباشد. نتایج یکی از مطالعات تجربی بر روی لیزوزومهای (lysozyme) موجود در سفیدهی تخم مرغ نشان میدهد که الیگومرهای سمی در مجاورت سطح سیلیکا تشکیل نمیشوند. علت این موضوع، تسریع فرآیند تشکیل فیبریل در حضور سیلیکا شناخته شده است [۵۱]. همچنین، فیبریلهای تشکیل شده در مجاورت سیلیکا عمدتا دارای ساختار صفحهای هستند، در حالی که در عدم حضور سیلیکا غالبا شکل کروی دارند. علت جذب پپتید به نانوذرات سیلیکا نیز در سالهای اخیر مورد توجه بسیاری قرار گرفته است. مواردی همچون آب دوستی و آبگریزی سطح، غلظت پپتید در محلول، غلظت نمک و اسیدیتهی محلول نیز بر میزان جذب پپتید به نانوذرات سیلیکا موثر هستند [۵۸]. نتایج حاصل از یک مطالعهی تجربی بر روی برهمکنش بیست اسید آمینهی موجود در طبیعت با سطح سیلیکا نشان میدهد که برهمکنشهای الکترواستاتیکی و آبگریزی در جذب اسیدهای آمینه به سطح نقش مهمی ایفا میکنند [۵]. یکی از مطالعات تجربی اخیر نیز نشان میدهد که ترکیبی از برهمکنشهای الکترواستاتیکی و آبگریزی مسئول پیوند پپتید به سطح سیلیکا است [۳۱].

اگرچه رفتار ملکولهای زیستی در مجاورت سطح سیلیکا در آزمایشهای تجربی قابل مشاهده است، بررسی جزییات در سطح مولکولی در آزمایشگاه ممکن نیست. بنابراین، مطالعات نظری بسیاری به بررسی رفتار انواع ملکولهای زیستی با سطوح مختلف میپردازند. به عنوان مثال، امامی و همکارانش تاثیر اسیدیته و اندازهی نانوذرات سیلیکا بر میزان جذب پپتید را مورد بررسی قرار دادند [۶۸]. آنها همچنین با استفاده از روش شبیهسازی دینامیک مولکولی قدرت جذب پپتید و پیوند انتخابی رزیجوهای (residue) مختلف را بهدست آورده و به نقش مهم برهمکنشهای آبگریزی در جذب پپتید به سطح اشاره کردهاند [۶۸].

در بخش اول این مطالعه، با استفاده از یک روش محاسباتی به بررسی هدایت گرمایی غشای سلولی با دو ترکیب مختلف می‌پردازیم. ابتدا، یک مدل غشای سلولی حاوی غلظت‌های مختلف کلسترول را بررسی می‌کنیم و سپس، به بررسی مدل غشای حاوی پروتیین آمیلویید می‌پردازیم. انگیزه‌ی اصلی از این بررسی از یک طرف وابستگی هدایت گرمایی به ساختار و از طرف دیگر رابطه‌ی بین ساختار غشا و غلظت‌های مختلف کلسترول در آن است [۷۹ و ۸۱].

همچنین، برای به دست آوردن هدایت گرمایی در غشاهای نامتقارن، مدل را به غشایی بسط می‌دهیم که در آن نسبت کلسترول در لایه‌ی خارجی به لایه‌ی داخلی برابر با ۱۲ می‌باشد. نمونه‌ی این غشا را می‌توان در سلول‌های سالم جداره‌ی روده‌ی بزرگ یافت. انگیزه‌ی اصلی برای بررسی این نوع غشا پس از مطالعه‌ی یکی از مقالات اخیر ایجاد شد که به بررسی هدایت گرمایی و یکسوسازی آن در غشای نامتقارن آرکائیال‌ها پرداخته بود [۹]. مطالعه‌ی دیگری نیز نشان داده است که تغییر کوچکی در دما می‌تواند برهم‌کنش پروتیین آمیلویید با سطوح آب‌دوست و آب‌گریز را تحت تاثیر قرار دهد [۳۴]. با توجه به حساسیت این پروتیین به دما سوالات بسیاری مطرح می‌شوند، از جمله این که واکنش این پروتیین به یک گرادیان دمایی چیست و یا پروفایل دما در حضور این پروتیین چگونه تغییر می‌کند. در ادامه به مطالعه‌ی یک مدل غشای حاوی بخشی از پروتیین آمیلویید می‌پردازیم. علاوه بر این، برای چنین مدلی ضریب یکسوسازی هدایت گرمایی را به دست می‌آوریم. لازم به ذکر است که این ضریب معیاری از اختلاف ضریب هدایت گرمایی در جهت مستقیم و معکوس می‌باشد.

در بخش دوم از این مطالعه، به بررسی برهم‌کنش پپتید آمیلویید و سطح سیلیکای آمورف می‌پردازیم. برای بررسی نقش سیلیکا در تشکیل توده‌های آمیلوییدی ابتدا باید دانست که چگونه یک تک‌پپتید با سطح سیلیکا پیوند برقرار می‌کند. انگیزه‌ی اصلی از این بررسی یکی از مطالعات تجربی گذشته است که تاثیر نانوذرات سیلیکا بر سرعت‌دهی به تشکیل توده‌ی آمیلوییدی را بررسی می‌کند. در آن مطالعه، نویسندگان بر این باورند که دما نقش مهمی بر چگونگی این اثر دارد [۶]. در این مطالعه، هسته‌ی آب‌گریز آمیلویید بتا را انتخاب کرده‌ایم. بسیاری معتقدند که این هسته در فرآیند تشکیل توده‌ی آمیلوییدی نقش مهمی ایفا می‌کند. آنچه که در مورد این بخش از آمیلویید بتا درمی‌یابیم قطعاً برای فهم سیستم‌های دیگر مفید خواهد بود. هدف این بخش از مطالعه، یافتن مدهای پیوندی و تغییرات ساختاری پپتید آمیلویید در مجاورت سطح سیلیکا می‌باشد.

روش

در بخش اول از این مطالعه، مدل‌های تمام اتم غشای دی پالمیتویل فسفاتیدیل کولین حاوی غلظت‌های مختلف کلسترول را با استفاده از CHARMM-GUI به دست می‌آوریم (شکل ۴). در این مدل‌ها، هر یک

از لایه‌های داخلی و خارجی غشا از ۳۶ مولکول لیپید تشکیل شده‌اند که بسته به غلظت مورد نظر برای کلسترول، بعضی از این تعداد را مولکول‌های کلسترول تشکیل می‌دهند. در این مدل‌ها غلظت کلسترول در لایه‌ی داخلی و خارجی غشا یکسان است. اگرچه ضریب هدایت گرمایی غشای دی پالمیتویل فسفاتیدیل کولین در مطالعات قبلی به دست آمده است [۸ و ۱۰۳] در اینجا این محاسبه را تکرار می‌کنیم تا هم تکرارپذیری محاسبات را ارزیابی کنیم و هم معیاری برای مقایسه‌ی هدایت گرمایی غشاهای حاوی کلسترول داشته باشیم.
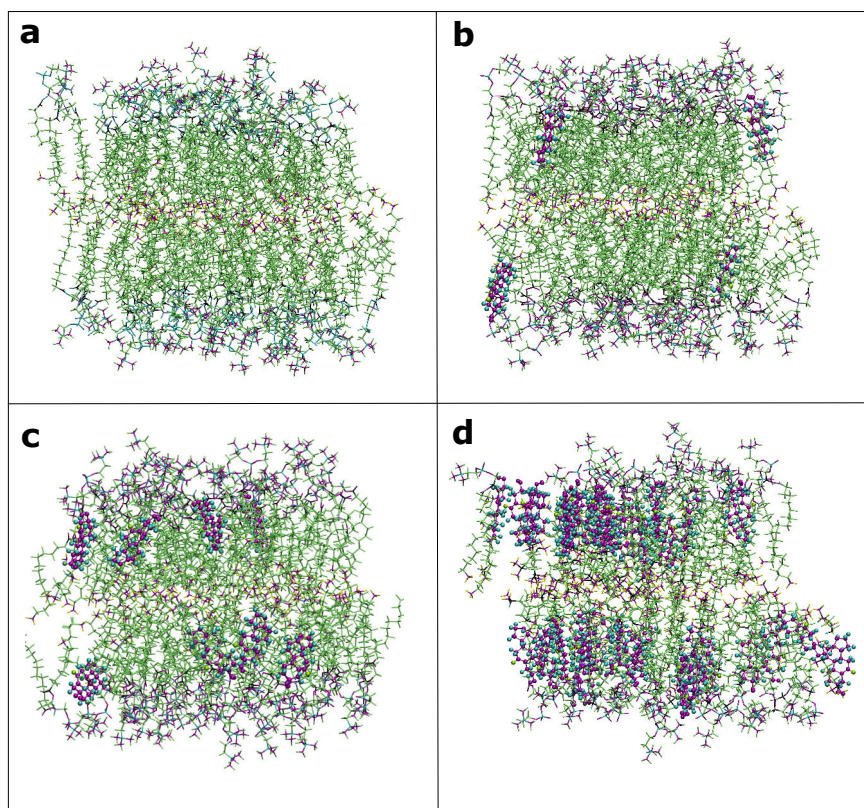
شکل ۴: مدل‌های غشای استفاده شده در این مطالعه با چهار غلظت مختلف کلسترول (۰٪ و ۵٪ و ۱۱٪ و ۵۰٪). همه غشاها از ۳۶ مولکول لیپید تشکیل شده اند. مولکول‌های کلسترول و لیپید به ترتیب با رنگ بنفش و سبز نشان داده شده اند.

برای ساخت مدل غشای حاوی پروتیین می‌توان از دو روش استفاده کرد. در روش اول پروتیین و مولکول‌های لیپید به طور تصادفی در جعبه‌ی شبیه‌سازی قرار داده می‌شوند و انرژی کل سیستم کمینه می‌گردد. چنین سیستمی به طور خود به خودی به شکل یک غشای دو لایه که پروتیین را در برگرفته سازمان می‌یابد. این فرایند به ویژه برای سیستم‌های بزرگ بسیار زمان‌بر است. روش دیگر آن است که پروتیین وارد یک غشای در حال تعادل شود. در این روش باید نکات بسیاری از جمله جهت‌گیری پروتیین در غشا و پایداری ساختار نهایی مد نظر قرار گیرند. نشاندن پروتیین‌ها در غشای لیپیدی از اهمیت خاصی برخوردار است چرا که تعیین کننده‌ی فعالیت زیستی، برهم‌کنش‌های بین مولکولی و پایداری می‌باشد [۹۹]. به دلیل محدودیت داده‌های آزمایشگاهی همچون پراکندگی پرتو ایکس، رزونانس مغناطیسی

هسته‌ای، طیف سنجی مادون قرمز، محاسبات بسیاری در جهت یافتن محل دقیق قرارگیری پروتیین‌ها در غشا انجام گرفته است [۷۴]. علاوه بر این، پایگاه‌های داده همچون OPM جهت قرارگیری صحیح پروتیین‌ها در غشای سلول را به کاربران ارایه می‌دهند [۱۰۰]. سرویس‌دهندگان اینترنتی بسیاری نیز مدل‌های تمام اتم (atomistic) و درشت دانه (coarse-grained) را برای آماده‌سازی ساختار اولیه‌ی انواع غشا در اختیار کاربران قرار می‌دهند. همچنین امکان وارد کردن پروتیین در غشا فراهم شده است [۱۰۱]. از آن جمله می‌توان به CHARMM-GUI و MemBuilder اشاره کرد [۱۰۲]. در این مطالعه، ابتدا ساختار اولیه‌ی پروتیین‌ها را از بانک داده‌ی پروتیین‌ها (protein data bank) به دست آوردیم [۷۷ و۱۰۹]. سپس این ساختارها را به پایگاه داده‌یOPM دادیم تا جهت‌گیری پروتیین نسبت به غشا به دست آید [۱۱۲]. سپس ساختار به دست آمده برای پروتیین را با استفاده از رابط گرافیکی کاربر CHARMM با مولکول‌های لیپید احاطه کردیم. سرانجام از Moltemplate برای قرار دادن غشای حاوی پروتیین در جعبه‌ی شبیه‌سازی و پرکردن فضای اطراف با مولکول‌های آب و یون استفاده کردیم [۱۱۳].

اولین گام در شبیه‌سازی‌ها به تعادل رساندن غشاهایی است که از CHARMM-GUI به دست آمده‌اند. برای انجام تمام شبیه‌سازی‌های این بخش از مطالعه از پکیج لمپس (LAMMPS) و برای به دست آوردن برهمکنش‌های لیپید - لیپید، پروتیین - لیپید و آب – لیپید از میدان نیروی CHARMM36 استفاده می‌کنیم [۱۰۴-۱۰۶]. همچنین مدل TIP3P را برای مدل کردن مولکول های آب به کار می‌بریم [۱۰۷]. تمام شبیه‌سازی‌های این بخش را در دو مرحله انجام می‌دهیم. در قسمت اول، از شبیه‌سازی دینامیک مولکولی تعادلی استفاده می‌کنیم و در بخش دوم، روش دینامیک مولکولی غیر تعادلی را برای محاسبه‌ی ضریب هدایت گرمایی را به کار می‌بریم.

ابتدا هر یک از سیستم‌ها را تحت فرایندکمینه‌سازی انرژی قرار داده و به تعادل می‌رسانیم. به منظور کاهش نیروهای بسیار بزرگ ناشی از برخورد اتم‌ها، فرآیند کمینه‌سازی انرژی را برای هر سیستم با استفاده از روش گرادیان مزدوج (conjugate gradient) و تا ۱۰۰۰۰ گام انجام می‌دهیم. علاوه بر این، به منظور پایدارسازی ساختارها، تمام غشاها را با استفاده از دینامیک لانژوین در دما و فشار بالا (فشار ۱۷۰ بار و دمای ۴۵۰ کلوین) به تعادل می‌رسانیم. در این مرحله از به تعادل‌رسانی با تعداد ۱۰۰۰ گام و طول گام ۰/۰۱ فمتوثانیه شروع کرده و به تدریج تعداد گام‌ها را به ۱۰۰۰۰۰ گام و طول آن‌ها را به یک فمتوثانیه می‌رسانیم. سپس فرآیند به تعادل‌رسانی تحت فشار و دمای ثابت (فشار یک بار و دمای ۳۳۰ کلوین) را به مدت یک نانوثانیه انجام می‌دهیم.

پس از پایان مرحله‌ی به تعادل‌رسانی، سطح مقطع غشا را به دست آورده و با مقادیر گزارش شده در مطالعات قبلی تطبیق می‌دهیم [۷۸]. سیستم‌ها را در دمای ۳۳۰ کلوین (بالاتر از دمای گذار فاز غشای

دی پالمیتویل فســفاتیدیل کولین که برابر با ۳۱۴ کلوین اســت) نگه میداریم [۱۱۴]. همچنین، فشــار سیستمها را با استفاده از فشارسنج Nose-Hoover حول مقدار یک بار تنظیم میکنیم [۱۱۵].

برای داشــتن جعبهی شـبیهسـازی مناسـب برای پیادهسـازی الگوریتم دینامیک مولکولی غیرتعادلی و همچنین داشـتن شرایط مرزی صحیح، غشـای سـلولی را موازی تصویر آینهای آن در راسـتای محور z در جعبه قرار داده و سپس فضاهای خالی اطراف را با تعداد مناسبی از مولکولهای آب پر میکنیم. در نهایت، سیستم را یک بار دیگر البته این بار به مدت کمتر (در حدود چند صد پیکو ثانیه) به تعادل میرسانیم.

در این مطالعه، به منظور پیادهسـازی الگوریتم دینامیک مولکولی غیرتعادلی وارون از روش مولر (-Müller Plathe) اسـتفاده میکنیم [۲۵]. در این روش، جعبهی شبیهسازی به لایههای متعدد تقسیم میگردد. در هر یک یا چند گام شــبیهسـازی، سـرعت گرمترین ذره در اولین لایه از جعبهی شـبیهسـازی با سـرعت سردترین ذره در لایهی میانی جعبه تعویض میگردد. بنابراین، پس از مدتی لایههای اول و میانی جعبه به ترتیب به سـردترین و گرمترین لایههای جعبهی شـبیهسـازی تبدیل میشـوند و درون جعبه یک شـارش گرمایی فیزیکی ازقسمت گرم به قسمت سرد شکل میگیرد. پس از آن که سیستم به حالت پایدار رسید، میتوان گرادیان دمایی را اندازه گیری کرد و ضریب هدایت گرمایی را از رابطهی فوریه (Fourier) محاسبه نمود. تعویض سرعتها با نرخ مشخصی انجام میشود و پارامتری است که توسط کاربر تنظیم میگردد. برای پایستگی تکانهی کل، لازم است تنها سرعت ذرات دارای جرم برابر تعویض شوند.

برای پیادهسـازی روش مولر، جعبهی شــبیهسـازی را به صــد لایه تقسـیم میکنیم (شـکل ۵). در شـبیهسـازیهای این قسـمت، بسـته به ارتفاع جعبه، ضـخامت یک لایه در حدود ۱/۸ تا ۱/۹ آنگسـتروم میباشد.

تعویض سرعت برای ذرات موجود در لایهی اول و وسط انجام میشود. طبق قرارداد، جهت مستقیم شارش گرما را از لایهی میانی جعبه (گرمترین لایه) به سمت دو انتهای جعبه (سردترین لایهها) در نظر میگیریم. از طرف دیگر هنگامی که لایهی میانی جعبه تبدیل به سردترین لایه و اولین لایه تبدیل به گرم ترین لایه شـود، گرما از دو انتهای جعبه به سـمت وسط آن شارش مییابد. در اینجا سـرعتها را هر ۰/۱ پیکوثانیه یکبار تعویض میکنیم. بنابراین، همواره در رژیم پاسـخ خطی هسـتیم و بدین ترتیب، میتوانیم ضـریب هدایت گرمایی را با استفاده از معادلهی زیر محاسبه کنیم.

$$\kappa = -\frac{J}{\nabla T} = -\frac{1}{2}\left(\frac{\frac{dQ}{Adt}}{\frac{dT}{dz}}\right)$$
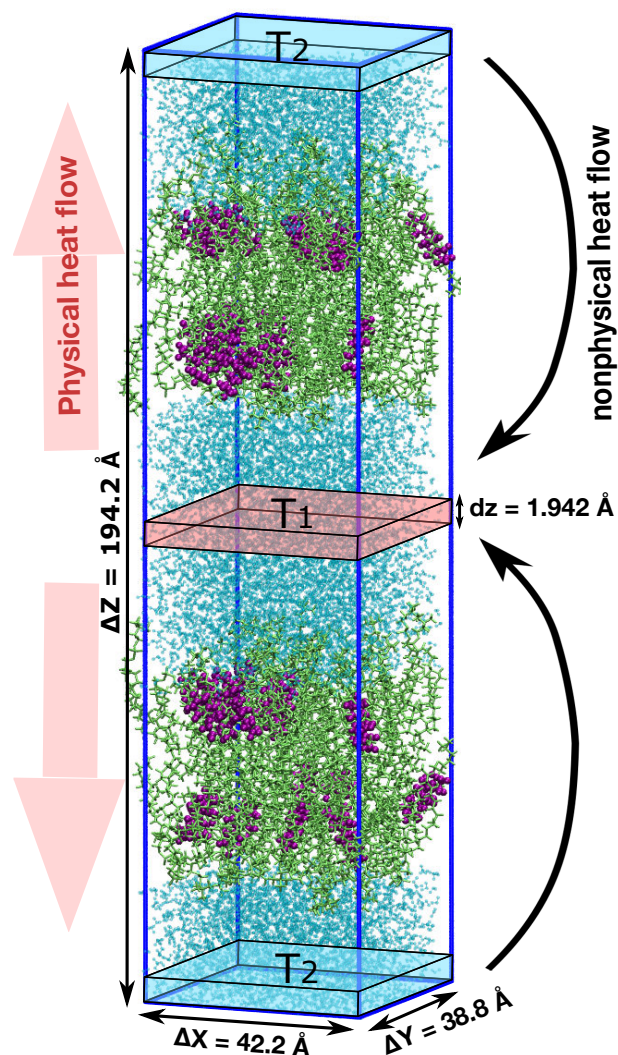
شکل ۵: شارش گرما در عرض غشا که سبب شکل‌گیری گرادیان دمایی در دوسمت غشا می‌گردد. گرمترین و سردترین لایه‌ها در جعبه به ترتیب با رنگ‌های قرمز و آبی روشن نشان داده شده اند.

در نتیجه‌ی تعویض سرعت‌ها، در هر گام شبیه‌سازی مقدار مشخصی انرژی جنبشی انباشته می‌گردد. در صورتی که تعویض سرعت‌ها به اندازه‌ی کافی آهسته انجام می‌پذیرد می‌توان گفت انرژی جنبشی انباشته شده تابعی خطی و اکیدا صعودی از زمان خواهد بود. در غیر این صورت، سیستم هرگز به حالت پایدار نخواهد رسید. شیب این تابع نیز نرخ شارش گرما را به دست می‌دهد.

پیاده‌سازی الگوریتم مولر به ایجاد لایه‌های گرم و سرد در دو طرف غشای سلول می‌انجامد. در مدت زمان چند صد پیکو ثانیه، دمای لایه‌های گرم و سرد به حالت پایا (steady state) می‌رسد (شکل ۶). در این مطالعه، تمام محاسبات را بر روی داده‌هایی انجام می‌دهیم که پس از گذشت یک نانو ثانیه از ابتدای شبیه‌سازی غیرتعادلی به دست آورده‌ایم. در اینجا کل مدت زمان شبیه‌سازی را به بلوک‌های به طول یک نانو ثانیه تقسیم‌بندی کرده و ضریب هدایت گرمایی را در هر بلوک محاسبه می‌کنیم. ضریب هدایت گرمایی کل برابر با میانگین ضرایب هدایت گرمایی بلوک‌ها خواهد بود.

۱۰
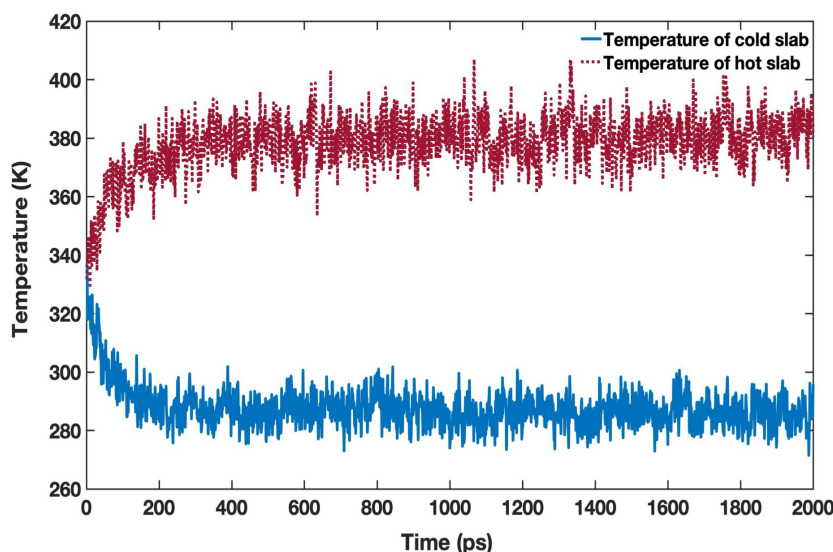
شکل ۶: پیاده‌سازی الگوریتم مولر منجر به تشکیل لایه‌های سرد و گرم در جعبه شبیه‌سازی می‌شود. طبق این شکل، با تعویض سرعت‌ها هر ۰/۱ پیکوثانیه یکبار، سیستم پس از چند صد پیکوثانیه از ابتدای شبیه‌سازی به حالت پایا می‌رسد.

طبق معادله زیر، ضرایب هدایت گرمایی به‌دست آمده در جهت‌های مستقیم و معکوس را می‌توان برای محاسبه‌ی ضریب یکسوسازی هدایت گرمایی به کار برد.

$$\varepsilon = \frac{|\kappa_f - \kappa_b|}{\kappa_b}$$

در بخش دوم از این مطالعه، برای شبیه‌سازی بخشی از پپتید آمیلویید بتا متشکل از ۸ اسید آمینه (KLVFFAED) در حضور آب و سیلیکا از پکیج شبیه سازی دینامیک مولکولی گرومکس (GROMACS) استفاده می‌کنیم [۱۳۳ - ۱۳۶] . طول و عرض جعبه‌ی شبیه‌سازی برابر با ۶/۵۶ و ۶/۵۷ نانومتر و ارتفاع آن برابر با ۸/۷ نانومتر می‌باشد. سیستم از ۷۷۱۸ مولکول آب به همراه یون‌های سدیم و کلر (متناسب با غلظت فیزیولوژیکی ۱۵۰ میلی‌مولار) تشکیل شده‌است. پتانسیل برهم‌کنش بین پپتید آمیلویید و مولکول‌های آب را از ترکیب میدان نیروی GROMOS43a1 و SPC/E به دست آورده‌ایم [۱۳۷ - ۱۳۹]. پارامترهای مربوط به برهم‌کنش آب و سطح سیلیکا که در یکی از مطالعات قبلی محاسبه شده‌است را در این مطالعه مورد استفاده قرار می‌دهیم [۶۴ و ۶۵]. پتانسیل به گونه‌ای کالیبره شده است که بتوان انرژی‌های پیوندی به دست آمده از محاسبات کوانتوم شیمی را بازتولید کرد [۱ و ۶۶]. برای یافتن جزئیات بیشتر درباره‌ی شکل پتانسیل و چگونگی توسعه‌ی آن، خواننده به مقالات مربوطه ارجاع داده می‌شود.

برای انتگرال‌گیری از معادلات حرکت سیستم از الگوریتم leap-frog استفاده می‌کنیم [۱۴۰]. برای برهم‌کنش‌های واندروالس، شعاع قطع لنارد جونز را یک نانومتر در نظر گرفته و برای محاسبه‌ی برهم‌کنش‌های الکترواستاتیکی در سیستم، از روش PME با فاصله‌ی گرید ۰/۱۲ نانومتر و برون‌یابی

مرتبه‌ی چهار استفاده می‌کنیم [۱۴۱ و ۱۴۲]. همچنین، شرایط مرزی متناوب را به تمام شبیه‌سازی‌ها اعمال می‌کنیم. شبیه‌سازی‌ها را در آنسامبل NVT انجام می‌دهیم و در دمای ۳۰۰ کلوین به تعادل می‌رسانیم.

همان‌طور که پیش‌تر توضیح داده شد، هدف ما از این مطالعه بررسی چگونگی تغییر شکل ساختاری آمیلویید بتا توسط سیلیکا و یافتن مدهای پیوندی بین پپتید و سطح می‌باشد. بدین منظور، ابتدا بخش مورد نظر پپتید آمیلویید بتا را در محیط آبی و بدون حضور سیلیکا شبیه‌سازی می‌کنیم. کل زمان شبیه‌سازی برای یک پپتید در آب ۵۰ نانوثانیه می‌باشد. در طول شبیه‌سازی مقدار شعاع ژیراسیون (radius of gyration) پپتید را محاسبه می‌نماییم که عددی در بازه‌ی (۰/۷۹ و۰/۵۶) می‌باشد. از این شبیه‌سازی، ۱۲ کنفورماسیون (conformation) پپتید با شعاع‌های ژیراسیون مختلف را استخراج کرده و به عنوان ساختار اولیه برای شروع شبیه‌سازی‌ها استفاده می‌نماییم. قطعه‌ای از سیلیکای آمورف که در این شبیه‌سازی‌ها استفاده شد دارای ۱۱۱۹۶ اتم، ضخامت ۳/۴ نانومتر و چگالی بار سطحی ۰/۸۲- الکترون بر نانومتر مربع می‌باشد. شکل ۷ پپتید و اسیدهای آمینه‌ی تشکیل‌دهنده‌ی آن و همچنین نمای فوقانی سطح سیلیکا را نشان می‌دهد.
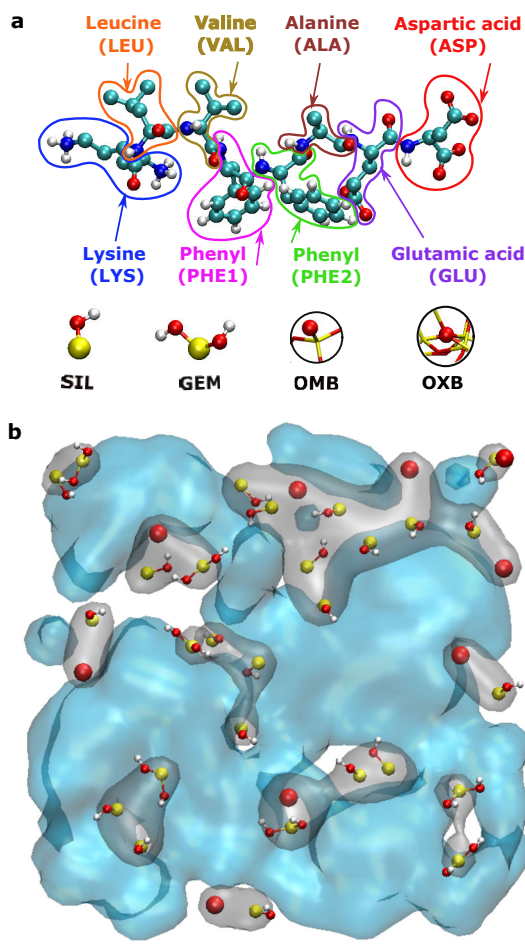
شکل ۷: پپتید و اسیدهای آمینه تشکیل دهنده‌ی آن در بالا و گروه‌های موجود روی سطح به همراه نمای فوقانی سطح در قسمت پایین نمایش داده شده اند.

گروه‌های شیمیایی مختلف بر روی سطح سیلیکا را به چهار دسته تقسیم‌بندی و در شکل ۷ به صورت نواحی جداگانه بر روی سطح مشخص کرده‌ایم. برای یافتن جزئیات بیشتر در رابطه با این چهار ناحیه به متن اصلی ارجاع داده می‌شود. جهت آماده‌سازی ساختارهای اولیه برای شبیه‌سازی، هر یک از ۱۲ کنفورماسیون تصادفی را در بالای چهار ناحیه‌ی نامبرده و در فاصله‌ای کمتر از طول دیبای سیستم (که در غلظت یونی مورد استفاده حدود ۰/۵ نانومتر می‌باشد) قرار می‌دهیم. بدین ترتیب، در مجموع ۴۸ شبیه‌سازی داریم که هر یک را به مدت ۵۰ نانو ثانیه اجرا می‌کنیم.

کنفورماسیون‌های مختلف پپتید، دارای فاصله‌های سر به سر (end-to-end distance) و جهت‌گیری‌های متفاوتی نسبت به بردار عمود بر سطح سیلیکا می‌باشند. به همین جهت، از این مولفه‌ها و روش خوشه‌بندی سلسله مراتبی بر مبنای روش وارد (Ward) برای دسته‌بندی کنفورماسیون‌های مختلف پپتید در نزدیک سطح سیلیکا استفاده می‌کنیم [۲۷].

نتایج

بخش اول

به منظور بررسی اثر کلسترول بر روی ساختار غشای دی پالمیتویل فسفاتیدیل کولین، سطح مقطع غشا را پس از به تعادل‌رسانی به دست می‌آوریم. طبق نتایج به دست آمده (شکل ۸)، افزایش کلسترول در غشا سبب کاهش سطح مقطع غشا می‌گردد که با نتایج گزارش شده از مطالعات گذشته منطبق می‌باشد [۷۹ و ۱۱۸].
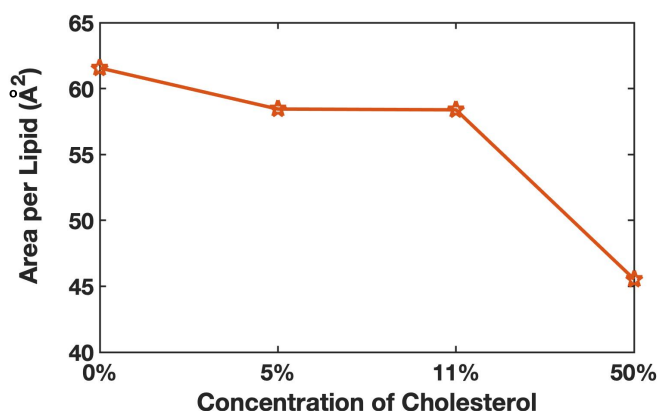
شکل ۸: کاهش سطح مقطع غشا در نتیجه‌ی افزایش غلظت کلسترول در آن

از مقایسه‌ی پروفایل دما و چگالی سیستم در راستای محور z می‌توان فهمید که در گرم‌ترین و سردترین لایه‌های جعبه تنها مولکول‌های آب یافت می‌شوند. باید به این نکته توجه داشت که دو پرش موجود در پروفایل دما (شکل ۹)، که یکی در ناحیه‌ی بین لایه‌های شماره‌ی ۲۰ و ۳۰ و دیگری بین لایه‌های شماره‌ی ۷۰ و ۸۰ رخ می‌دهند، دقیقاً منطبق بر مقادیر کمینه‌ی چگالی هستند. این مقادیر کمینه در محل به هم رسیدن لیپیدهای دو لایه‌ی داخلی و خارجی غشا اتفاق می‌افتند [۸].
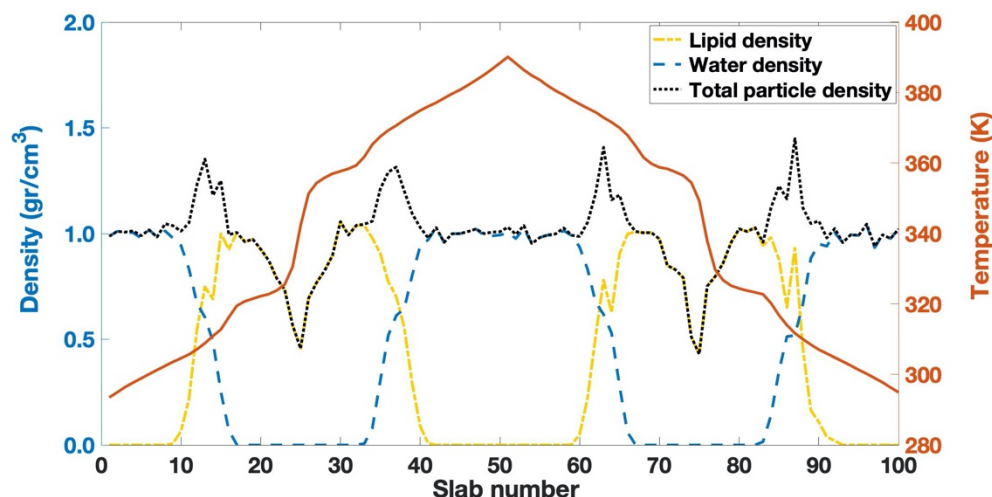
شکل ۹: پروفایل چگالی و دمای سیستم

پروفایل‌های چگالی نشــان داده شــده در شــکل ۹ قبل از اعمال الگوریتم دینامیک مولکولی غیرتعادلی به سیســتم به دســت آمده اند. پس از اعمال این الگوریتم تغییر ناچیزی در چگالی آب رخ می‌دهد به این ترتیب که در ناحیه‌ی گرم‌تر چگالی اندکی کمتر و در ناحیه‌ی سردتر چگالی اندکی بیشتر است. در چگالی لیپیدها تغییری رخ نمی‌دهد.

در این مطالعه، مقدار ضــریب هدایت گرمایی غشــای دی پالمیتویل فسـفاتیدیل کولین را در اختلاف دمای ۷۴ کلوین برابر با ۰/۰۱ ± ۰/۵۷ به دست آوردیم. این مقدار با مقادیر به دسـت آمده توسـط یوسـفیان و همکـارانش بـه خوبی مطـابقـت دارد (۰/۰۴ ± ۰/۵۱ در اختلاف دمـای ۷۵ کلوین) [۱۰۳]. در یکی از مطالعات تجربی اخیر، هدایت گرمایی غشــا در اختلاف دمای ۲۰ کلوین ۰/۰۲ ± ۰/۲ گزارش شــد[۷] و بنابر اطلاع نویسنده از معدود مواردی است که به صورت آزمایشگاهی اندازه‌گیری شده است.

تفاوت در مقادیر گزارش شده برای هدایت گرمایی غشا نه تنها ناشی از تفاوت‌های ساختاری بلکه به علت تفاوت در گرادیان‌های دمایی اعمال شــده به دو طرف غشـا می‌باشــد [۷ و۱۰۳]. به عنوان مثال، یکی از مطالعات محاسباتی گذشته هدایت گرمایی مدلی از غشا را ۰/۲۵ در اختلاف دمای۱۲ کلوین گزارش کرده است [۹۲].

نتایج به دست آمده از آزمون تی (t test) نشـان می‌دهد که حضور کلسترول در غشا به ویژه در غلظت‌های زیاد، سـبب افزایش هدایت گرمایی غشــای لیپیدی می‌شــود (شــکل ۱۰). علت این امر را می‌توان نقش کلسـترول در افزایش نظم ساختاری غشای سلول دانست [۸۱]. طبق این نتایج، هدایت گرمایی مدل‌های غشا با سطوح مختلف کلسترول متفاوت است و این تفاوت در تمام موارد به جز یکی از آن‌ها (غشای دارای ۵٪ و ۱۱٪ کلسـترول) از نظر آماری معنی‌دار (با سطح معنی‌داری ۰/۰۵) می‌باشد. دلیل این امر را می‌توان در تاثیر کلسترول بر برهم‌کنش مولکول‌های آب و غشای سلول جستجو کرد [۱۲۱].

۱۵
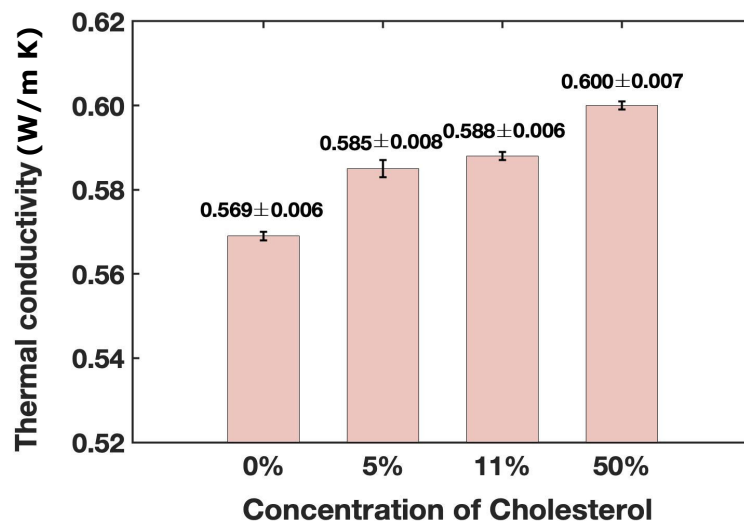
شکل ۱۰: هدایت گرمایی غشاهای حاوی غلظت‌های مختلف کلسترول

طبق این نتایج، کلسترول سبب افزایش نفوذ مولکول‌های آب به قسمت آب‌دوست غشا می‌گردد. از آن‌جا که مطالعات بسیاری برهم‌کنش‌های غشا و مولکول‌های آب را عاملی تعیین کننده در هدایت گرمایی غشا دانسته‌اند، در این قسمت به بررسی هیدراتاسیون (hydration) سرهای لیپیدها در دو مدل غشای بدون کلسترول و غشای حاوی ۵۰٪ کلسترول می‌پردازیم. بدین ترتیب، تابع توزیع شعاعی اکسیژن موجود در مولکول‌های آب را که در شعاع معینی از نیتروژن موجود در سر لیپیدها قرار دارند، به دست می‌آوریم (شکل ۱۱). نتایج به دست آمده نشان می‌دهند که هیدراتاسیون در غشای حاوی ۵۰٪ کلسترول افزایش یافته است.
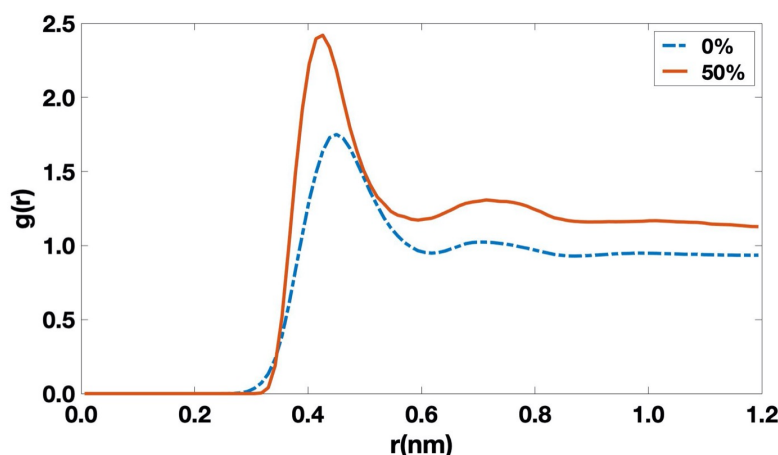
شکل ۱۱: تابع توزیع شعاعی اتم‌های اکسیژن آب که در اطراف اتم‌های نیتروژن موجود در سرهای فسفولیپیدها یافت می‌شوند برای دو مدل غشای بدون کلسترول و غشای حاوی ۵۰٪ کلسترول رسم شده است.

همان‌طور که پیش‌تر اشاره کردیم، مطالعات بسیاری به بررسی غلظت نامتقارن کلسترول در لایه‌های داخلی و خارجی غشا پرداخته‌اند [۱۲۲ و ۱۲۳]. به منظور دستیابی به نتایج واقعی‌تر باید این عدم تقارن

را در مدل‌های غشـا وارد کرد. در این مطالعه، از یک مدل غشـای رسـیده به تعادل رسـیده با غلظت‌های نابرابر کلسترول در دو لایه‌ی خارجی و داخلی غشا استفاده می‌کنیم. در مدل غشای مورد استفاده در این مطالعه ۳۳/۳٪ از لایه‌ی خارجی و ۲/۷٪ از لایه‌ی داخلی از کلسـترول تشکیل شده‌است. هدایت گرمایی این مدل غشا را در دو جهت مستقیم و معکوس به دست می‌آوریم (شکل ۱۲).
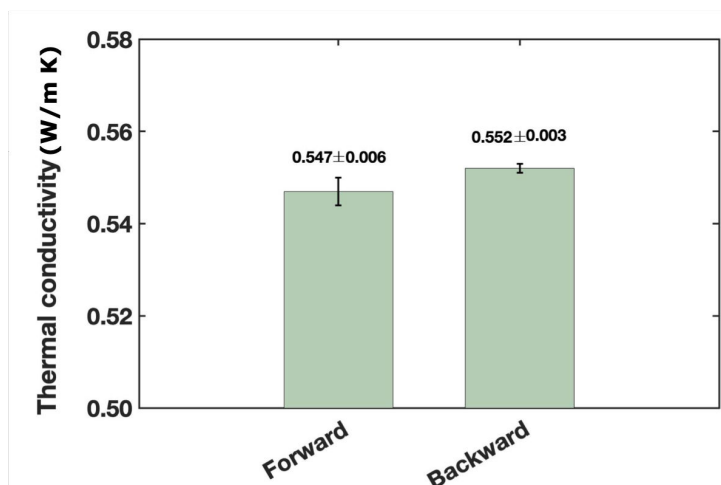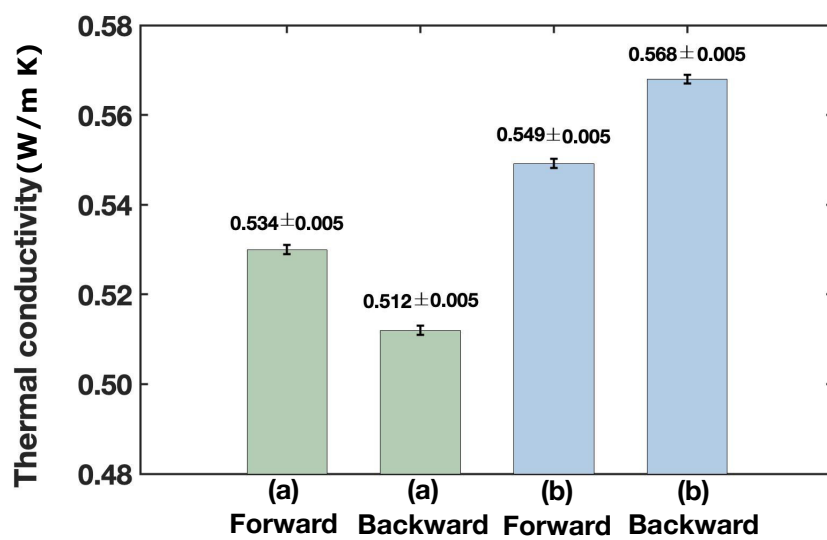

شکل ۱۲: ضرایب هدایت گرمایی در جهت مستقیم و معکوس برای غشای نامتقارن

طبق نتایج به دسـت آمده از این مطالعه، ضـریب هدایت گرمایی در غشـاهای نامتقارن کمتر از غشـاهای متقارن اسـت. عدم تقارن در سـاختار لایه‌های غشـای نامتقارن دلیلی بر کاهش هدایت گرمایی غشا اسـت. نمونه‌ی دیگری از عدم تقارن غشـا و تاثیر آن بر هدایت گرمایی را می‌توان در یکی از مطالعات گذشته دید که در آن یکی از لایه‌های غشـا در دمای بالاتر از دمای گذار لیپید (در فاز ژل) و دیگری در دمای پایین‌تر از دمای گذار لیپید (در فاز کریسـتال مایع) می‌باشـد و همین عدم تقارن سـبب کاهش هدایت گرمایی در آن غشا شده است [۱۰۳]. در این مطالعه، فاکتور یکسوسازی هدایت گرمایی را برای غشای نامتقارن برابر با ۰/۰۰۸ به دست آوردیم که بسـیار کمتر از مقدار متناظر برای غشای آرکائیال‌ها است [۹].

به منظور بررسـی هدایت گرمایی غشـا در حضـور پروتیین آمیلویید دو حالت متفاوت را در نظر می‌گیریم (شکل ۱۳). در حالت اول، قسـمتی از پروتیین که در عرض غشا قرار می‌گیرد و در حالت دوم، قسـمتی از آن که روی سطح غشا قرار دارد را مورد بررسی قرار می دهیم. برای هر دو حالت، ضرایب هدایت گرمایی را در جهت‌های مسـتقیم و معکوس به دسـت می‌آوریم. نتایج نشـان می‌دهند که در هر دو مدل، ضـرایب هدایت گرمایی در جهت‌های مستقیم و معکوس متفاوت هستند (شکل ۱۴).

۱۷
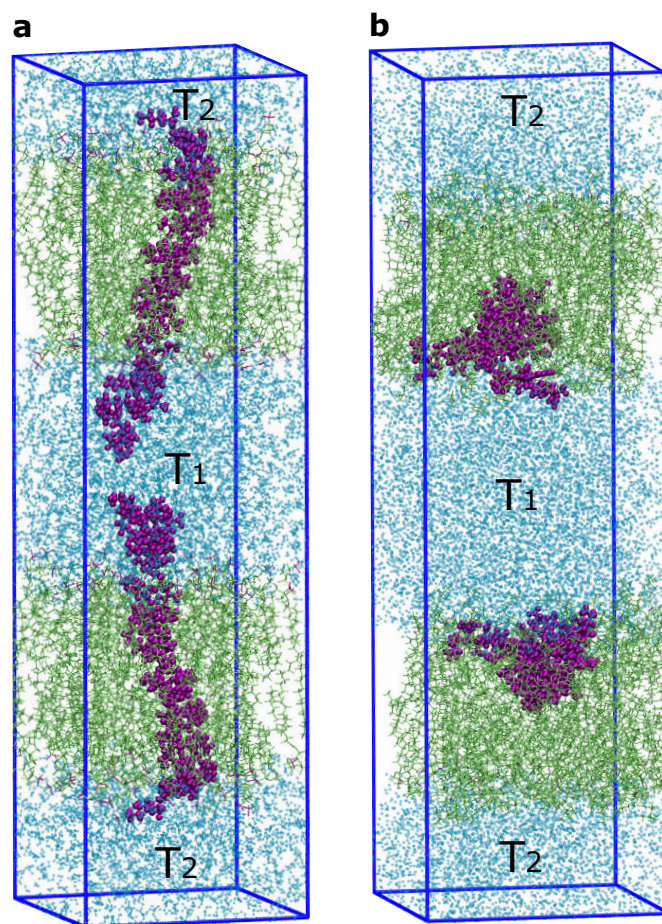
شکل ۱۳: دو مدل غشای حاوی پروتیین آمیلویید. لیپید و پروتیین به ترتیب با رنگ‌های سبز و بنفش نشان داده شده‌اند.


شکل ۱۴: ضرایب هدایت گرمایی غشاهای حاوی پروتیین آمیلویید

برای مقایسه‌ی ضرایب هدایت گرمایی غشاهای حاوی پروتیین در جهات مستقیم و معکوس از آزمون تی استفاده می‌کنیم. نتایج این آزمون تفاوت معنی‌داری را بین ضرایب هدایت گرمایی به دست آمده در دو جهت نشان می‌دهد. ضرایب یکسوسازی که برای غشاهای حاوی پروتیین به دست آورده‌ایم با مقادیر گزارش شده برای غشای سلول‌های دیگر هم‌خوانی دارد [۹].

بخش دوم

کنفورماسیون‌های مختلف پپتید در نزدیکی سطح سیلیکا

در تمام شبیه‌سازی‌ها به جز یکی از آن‌ها، پس از گذشت حدود ۱۰ نانوثانیه از ابتدای شبیه‌سازی، پپتید به سمت سطح حرکت کرده و با گروه‌های شیمیایی مختلف سطح برهم‌کنش می‌کند. شکل ۱۵، نمودار به دست آمده از خوشه‌بندی کنفورماسیون‌های حاصل از ۴۸ شبیه‌سازی را نشان می‌دهد. با استفاده از اختلاف بین تعداد داده‌های وارد شده برای خوشه‌بندی و عددی که به ازای آن جهش بزرگی در این نمودار دیده شود می‌توان تعداد خوشه‌های مناسب برای خوشه‌بندی را تعیین نمود. در اینجا جهش بر روی عدد ۴۵ می‌باشد و بنابراین تعداد خوشه‌ی مناسب برای خوشه‌بندی برابر با سه به دست می‌آید. طبق شکل ۱۶ که نمودار حاصل از خوشه‌بندی را نشان می‌دهد، بیشترین فاصله بین خوشه‌ها نیز زمانی رخ می‌دهد که سه خوشه‌ی مختلف تشکیل شده باشد.
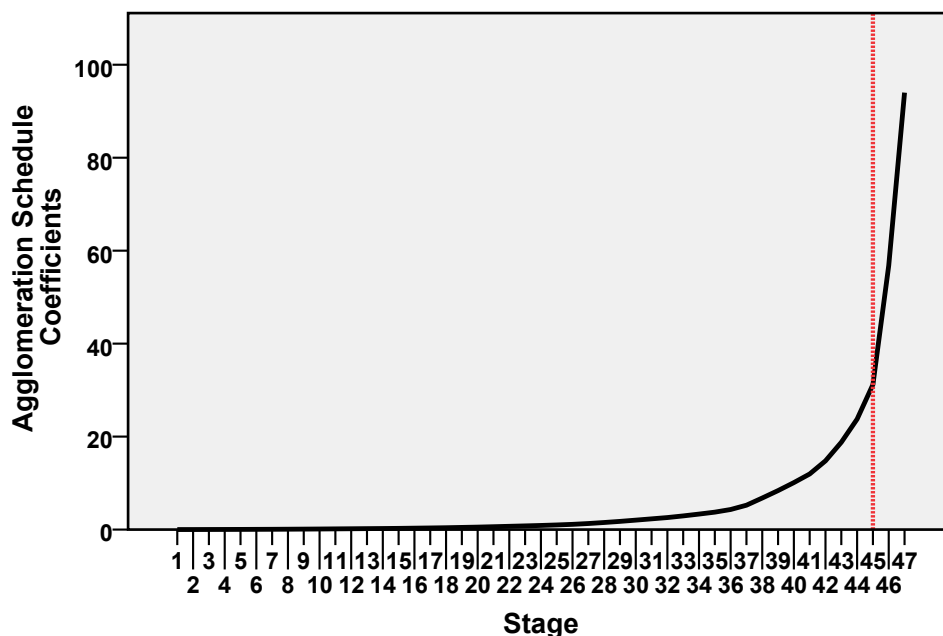

شکل ۱۵: نمودار نشان دهنده‌ی تعداد مناسب خوشه‌ها جهت خوشه‌بندی

۱۹
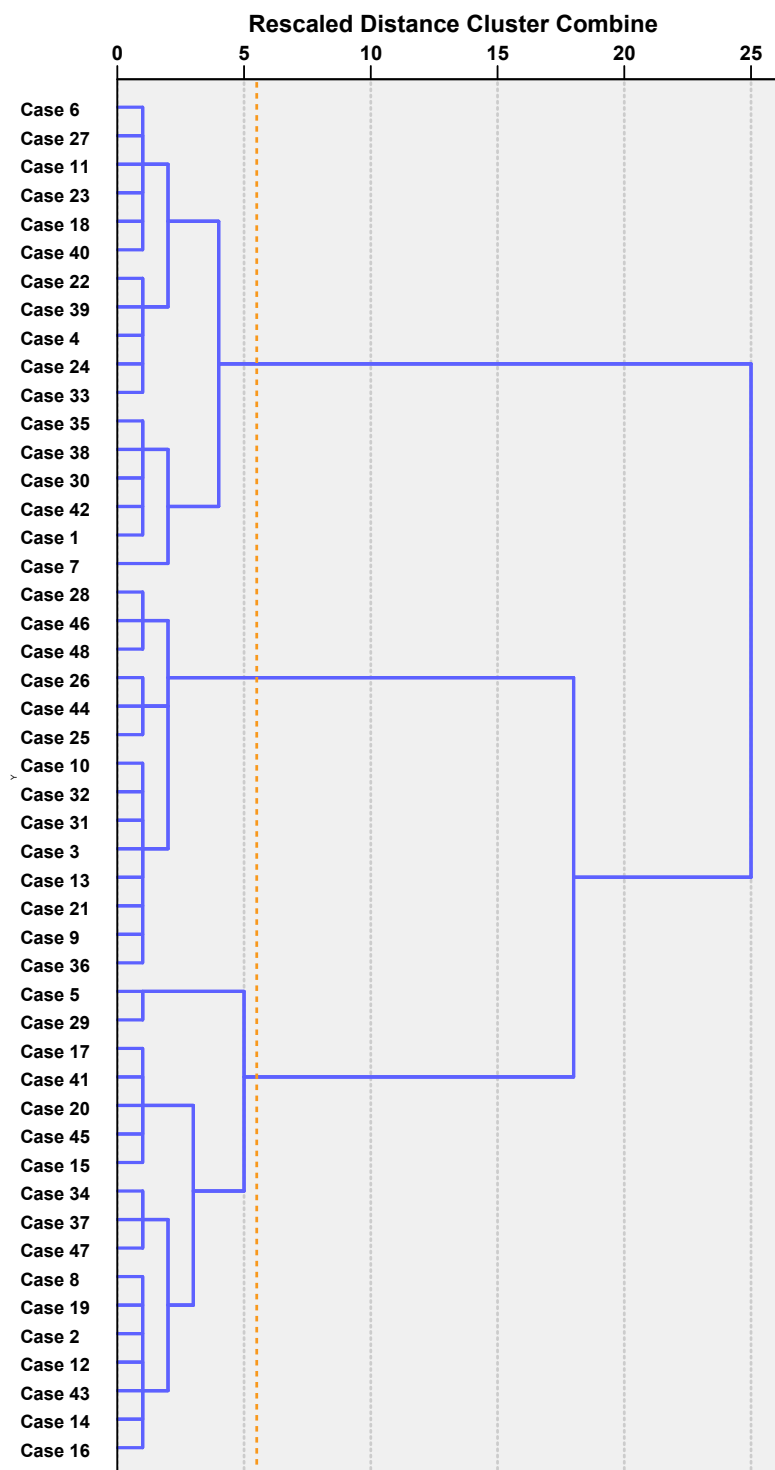
شکل ۱۶: نمودار دندروگرام نشان دهندهی خوشههای تشکیل شده

سه نمونه از کنفورماسیونهایی که در هر یک از خوشهها قرار دارند در شکل ۱۷ نمایش داده شدهاست. در خوشهی شماره یک پپتید به صورت خمیده، در خوشهی شماره دو به شکل گسترده بر روی سطح و در

خوشـه‌ی شـماره سـه به صـورت گسـترده ولی عمود بر سـطح می‌باشـد. طبق نمودار نشـان داده شـده در شکل۱۸، حدود ۳۵٪ از کنفورماسـیون‌ها در خوشـه‌ی شـماره یک، ۳۵٪ از آن‌ها در خوشـه‌ی شـماره دو و حدود ۳۰٪ از آن‌ها در خوشه‌ی شماره سه قرار گرفته‌اند.
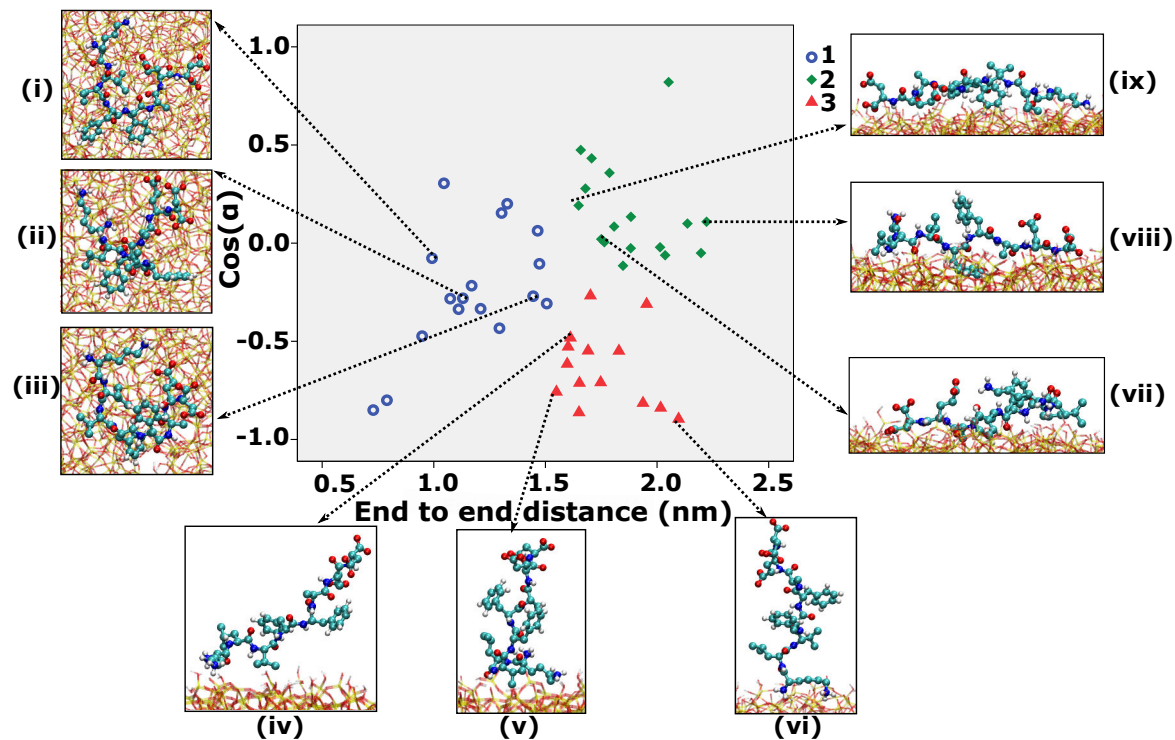
شکل ۱۷: کنفورماسیون‌های نهایی پپتید در سه خوشه دسته بندی می‌شوند.
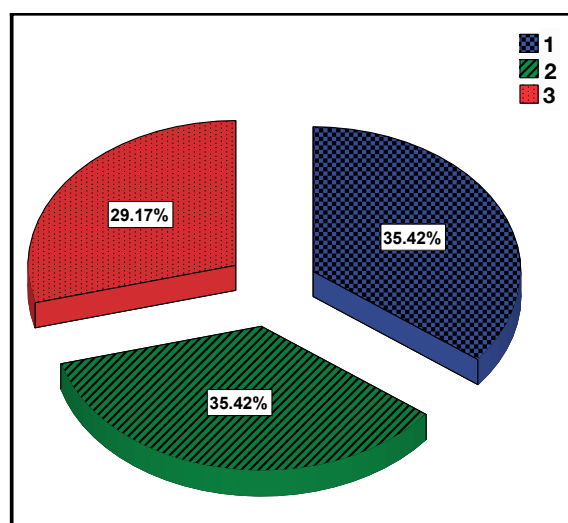
شکل ۱۸: درصد کنفورماسیون‌های موجود در هر خوشه

همان‌طور که می‌دانید، پپتید از گروه‌های شـیمیایی مختلفی تشـکیل شـده اسـت که با سـطح سـیلیکا برهم‌کنش می‌کنند. از جمله‌ی این گروه‌ها می‌توان به گروه آمین (NH_3^+) با بارمثبت، حلقه‌ی آب‌گریز فنیل‌آلانین (phenylalanine)، و گروه کربوکسـیلات (COO^-) با بار منفی اشـاره کرد. برای تعیین مد پیوندی غالب، تابع توزیع شعاعی را برای گروه‌های مختلف پپتید و سطح سیلیکا محاسبه می‌کنیم.

مدهای پیوندی پپتید

پپتید می‌تواند با گروه‌های شـیمیایی مختلف روی سـطح سـیلیکا پیوند تشـکیل دهد. به منظور کمی‌سازی بهتر نسـبت مدهای پیوندی مختلف، تابع توزیع شعاعی را برای گروه‌های مختلف پپتید و سیلیکا به دست آوردیم. شـکل ۱۹ تابع‌های توزیع شـعاعی مربوط به برهم‌کنش بین گروه‌های مختلف پپتید و سـیلیکا را نشـان می‌دهد. در این نمودار، میانگین مقادیر مربوطه در طول ۲۰ نانو ثانیه‌ی آخر شـبیه‌سازی‌ها نشان داده شده‌اند. پیوندهای آب‌گریزی عمدتا در خوشه‌های شماره‌ی یک و دو رخ داده‌اند؛ در حالی که در خوشه‌ی شماره سه برهم‌کنش‌های الکترواستاتیکی سهم بیشتری در پیوند پپتید به سطح داشته‌اند.
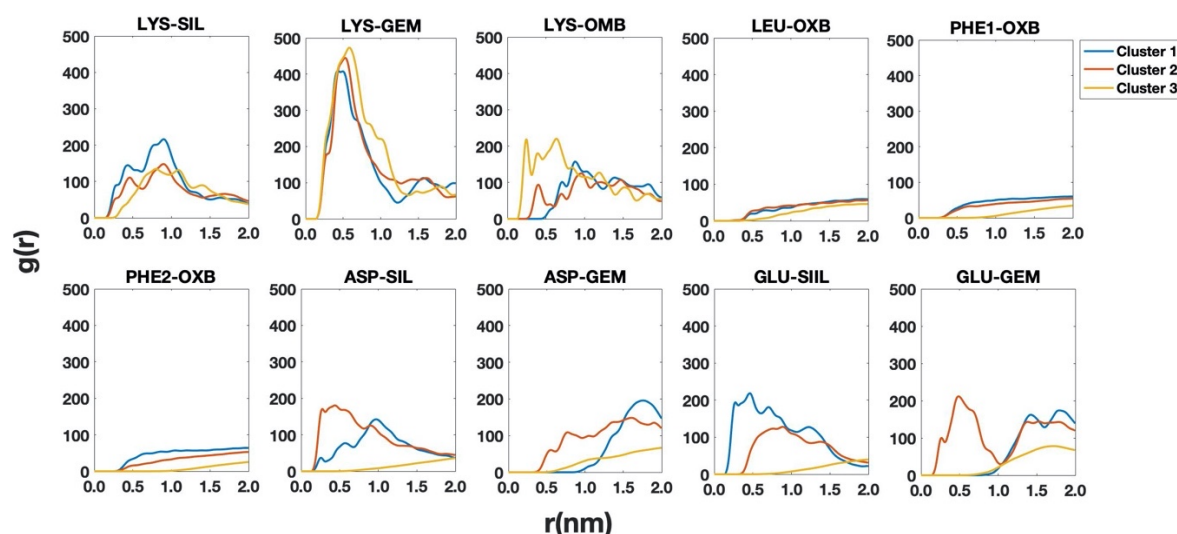
شکل ۱۹: میانگین توابع توزیع شعاعی اسیدهای آمینه‌ی مختلف در اطراف گروه‌های مورد نظر بر روی سطح سیلیکا برای سه خوشه‌ی نشان داده شده در شکل ۱۷

جلب اسـت بدانید که لایسـین (lysine) با بار مثبت بیشـتری به تشـکیل پیوند با گروه‌های هیدروکسـیل موجود روی سـطح نشـان می‌دهد. همچنین، برهم‌کنش بین سـطح و گروه‌های آسـپارتیک (aspartic) و گلوتامیک (glutamic) با بار منفی در موارد بسـیار کمی دیده می‌شـود. مشـابه با آنچه که مطالعات گذشـته گزارش کرده‌اند، ما نیز بر این باوریم که پیوند مولکول‌های زیسـتی به سـطح سـیلیکا نتیجه‌ی ترکیب پیچیده‌ای از برهم‌کنش‌های آب‌گریزی و الکترواستاتیکی می‌باشد [۱].

دینامیک جهت‌گیری مجدد (reorientational dynamics)

تاکنون در مورد تاثیر سـطح سـیلیکا بر ویژگی‌های ایسـتای پپتید با تاکید بر مدهای پیوندی و نیز اهمیت نسـبی برهم‌کنش‌های آب‌گریزی و الکترواسـتاتیکی صـحبت کردیم. انتظار می‌رود که این بر هم‌کنش‌های قوی تاثیر قابل ملاحظه‌ای بر افت و خیزهای دینامیکی پپتید داشـته باشند و به دنبال آن، تشکیل توده‌ی آمیلوییدی را تحت تاثیر قرار دهند. شـــکل ۲۰ دینامیک جهت‌گیری مجدد را برای کنفورماســـیون‌های متعلق به هر سه خوشه نشـان می‌دهد. برای به دست آوردن این کمیت، زاویه‌ی بین بردار عمود بر سطح و بردار واصـل دو انتهای پپتید را در نظر می‌گیریم و خود همبسـتگی آن را در طول زمان بررسـی می‌کنیم. همچنین، این خود همبستگی را برای پپتید در محیط آبی و در عدم حضور سیلیکا نیز به دست می‌آوریم. نتایج به دست آمده نشان می‌دهند که مشخصه‌ی دینامیک جهت‌گیری مجدد برای پپتید در هر خوشه با کنفورماسیون‌ها و مدهای پیوندی مختلف، متفاوت می‌باشد.
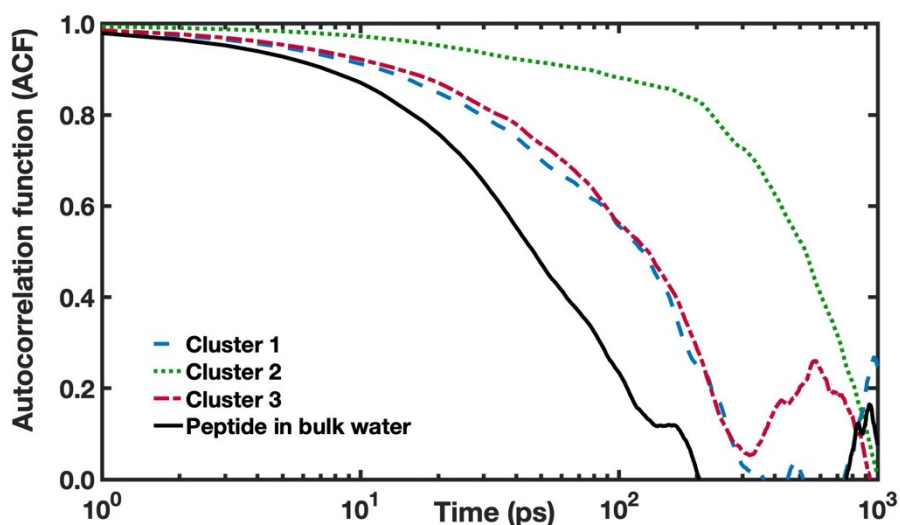
شکل ۲۰: تابع خودهمبستگی کسینوس زاویه‌ی بین بردار واصل دو سر پپتید و بردار نرمال سطح برای هریک از خوشه‌ها و همچنین برای پپتید در آب بر حسب زمان رسم شده است.

به طور مشـخص، کنفورماسـیون‌های مربوط به خوشـه‌ی شـماره دو دارای دینامیک آهسـته‌تری (در حدود یک نانوثانیه) نسـبت به کنفورماسـیون‌های موجود در دو خوشـه‌ی دیگر می‌باشند. به نوعی می‌توان گفت که ایجاد تعداد زیادی از پیوندهای قطبی و آب‌گریزی به شدت سبب عدم تحرک پپتید می‌گردد. این نتیجه با گزارش‌های موجود در مطالعات قبلی مبنی بر محدود شـدن درجه‌های آزادی پپتید روی سـطوح مطابقت دارد [۱۵۱]. این شـکل همچنین نشـان می‌دهد که کنفورماسـیون‌های مربوط به خوشـه‌ی شـماره یک که غالبا منحنی شـکل هسـتند، دارای افت و خیزهای آهسـته‌تری نسـبت به کنفرماسیون‌های مربوطه در غیاب سیلیکا می‌باشند.

جمع‌بندی و پیشنهادات

در بخش اول این مطالعه، با استفاده از روش دینامیک مولکولی غیر تعادلی وارون، هدایت گرمایی مدل‌های تمام اتم غشا با دو ترکیب مختلف را به دست آوردیم [۱۵۲]. ابتدا هدایت گرمایی غشای دی پالمیتویل فسفاتیدیل کولین را در غلظت‌های مختلف کلسترول بررسی کردیم. نتایج حاصل از این مطالعه نشان می‌دهند بین غلظت کلسترول در غشا و هدایت گرمایی غشا رابطه‌ی مستقیم وجود دارد. افزایش نظم ساختاری غشا را می‌توان دلیلی بر افزایش هدایت گرمایی آن در نتیجه‌ی افزایش کلسترول دانست. در مطالعه‌ی دیگری آمده است که اثر آب‌گریزی کلسترول باعث متراکم ساختن زنجیره‌های هیدروکربنی لیپیدها و در نتیجه افزایش نظم در غشا می‌شود [۱۲۵].

نتایج به دست آمده از مدل غشایی که توزیع کلسترول در دو لایه‌ی آن نامتقارن می‌باشد نیز تاییدی بر صحت این موضوع است. هدایت گرمایی کمتر غشای نامتقارن نسبت به غشاهای متقارن نشان‌دهنده‌ی ارتباط نزدیک بین نظم ساختاری غشا و هدایت گرمایی آن می‌باشد. علاوه بر این، نتایج این مطالعه نشان می‌دهد که اضافه شدن کلسترول به غشا سبب افزایش هیدراتاسیون سر فسفولیپیدها می‌شود. چگالی بیشتر مولکول‌های آب در سطح مشترک (interface) آب و لیپید، برهم‌کنش بین آب و غشا را افزایش می‌دهد. این افزایش می‌تواند تا حدودی کاهش شدید در هدایت گرمایی محلی در سطح مشترک آب و لیپید (که در گزارشات قبلی به آن اشاره شده است) را جبران کند [۸].

هم‌چنین، نشان داده شده است که کلسترول بر هم کنش واندروالس (van der Waals) بین زنجیره‌های هیدروکربنی لیپیدها را افزایش می‌دهد. این افزایش برهم‌کنش‌ها دلیلی بر افزایش هدایت گرمایی غشای لیپیدی می‌باشد. به طور مشابه، مایعات ساده نیز در چگالی بالا هدایت گرمایی بیشتری نشان می‌دهند که عمدتاً ناشی از نیروی دافعه‌ی بین مولکولی در آن‌ها می‌باشد [۱۲۶ و ۱۲۷].

سپس به بررسی غشای حاوی پروتیین آمیلویید پرداختیم. در این غشا تفاوت قابل توجهی بین ضرایب هدایت گرمایی در حالت مستقیم و معکوس مشاهده شد. در نتیجه می‌توان گفت هنگامی که گرما از غشای حاوی پروتیین در دو جهت متقابل شارش می‌یابدِ، غشا به شکل یک یکسوساز عمل می‌کند. اگرچه بسیاری معتقدند که این یکسوسازی به اختلاف دمای دو طرف غشا وابسته است [۹]، ضرایب یکسوسازی به دست آمده در این مطالعه به ضریب یکسوسازی غشای نامتقارن آرکائیال‌ها که در اختلاف دمای ۲۰ کلوین اندازه‌گیری شده‌اند نزدیک‌تر است تا به ضریب یکسوسازی نانولوله‌های کربنی که در اختلاف دمای ۱۰۰ کلوین به دست آمده‌اند [۱۲۸ و ۱۲۹]. بنابراین می‌توان گفت ضریب یکسوسازی هدایت گرمایی بیشتر از آن‌که به اختلاف دمای دو طرف بستگی داشته باشد تحت تاثیر ساختار است. البته برای اثبات این مطلب نیاز به بررسی‌های بیشتر می‌باشد.

نتایج این بخش از مطالعه در توسعه‌ی روش‌های درمان انتخابی مانند روش نور گرمایی (photothermal) برای درمان سرطان کاربرد دارد [۱۳۰]. طبق آنچه که به طور مشخص برای مدل غشای سلول‌های جداره‌ی روده‌ی بزرگ مطرح شد، سلول‌های سالم که در غشای آن‌ها نسبت کلسترول لایه‌ی خارجی به

۲۴

لایه‌ی داخلی بیشتر است در برابر هدایت گرما مقاومت بیشتری نشان داده و با احتمال بیشتری در مقابل آسیب احتمالی در فرایند درمان سالم می‌مانند.

در بخش دوم این مطالعه پپتید آمیلویید بتا مورد بررسی قرار گرفت. در شبیه‌سازی‌های انجام شده مشاهده کردیم که پپتید در بازه‌ی زمانی ۱۰ نانو ثانیه و به طور برگشت‌ناپذیری با سطح سیلیکا پیوند می‌دهد. مدهای پیوندی را می‌توان ترکیبی از برهم‌کنش‌های آب‌گریزی مربوط به گروه‌های فنیل‌آلانین و بر هم‌کنش‌های قطبی بین اسیدهای آمینه‌ی باردار و سطح سیلیکا معرفی کرد. همچنین، نشان دادیم که قرار گرفتن پپتید آمیلویید در کنار سطح منجر به شکل‌گیری کنفورماسیون‌های متنوعی می‌گردد که از آن جمله می‌توان به فرم خمیده، گسترده بر روی سطح و ایستاده به طور عمود بر سطح اشاره کرد.

بنابراین می‌توان گفت که سطح مشترک آب و سیلیکای آمورف می‌تواند کنفورماسیون‌های پپتید را به گونه‌ای تغییر دهد که تاثیر بسزایی بر فرآیند تشکیل توده‌ی آمیلویید داشته باشد. همچنین، این مطالعه تاییدی بر نتایج مطالعات گذشته است، چرا که طبق یافته‌های ما پیوند پپتید با سطح در نتیجه‌ی ترکیبی از برهمکنش‌های الکترواستاتیکی و آب‌گریزی می‌باشد. البته بررسی ترمودینامیک (thermodynamics) و کینتیک (kinetics) تشکیل توده‌ی آمیلویید در مجاورت سطح سیلیکای آمورف خارج از محدوده‌ی این مطالعه است.

شبیه‌سازی‌های انجام شده با یک پپتید، امکان پیش‌بینی مراحل بعدی را به طور کیفی فراهم می‌کند. به طور کلی می‌توان گفت جهت‌گیری یک پپتید چه به صورت موازی با سطح و چه عمود بر آن باشد، می‌تواند در مراحل ابتدایی تشکیل توده تاثیرگذار باشد. پیش‌بینی می‌شود که کنفورماسیون عمود بر سطح منجر به تشکیل صفحات بتای موازی در اولین لایه‌ی نزدیک سطح شود، چرا که برای تشکیل صفحات بتای غیرموازی (anti-parallel) لازم است دست کم یکی از پپتیدها از انتهای دارای بار منفی درمجاورت سطح سیلیکا قرار گیرد و از آنجا که سطح نیز دارای بار منفی است باید انرژی زیادی هزینه شود. از طرف دیگر، کنفورماسیون گسترده بر روی سطح می‌تواند با احتمال برابر منجر به تشکیل صفحات بتای موازی و یا غیرموازی شود. البته پیشنهاد می‌شود که برای اثبات این پیش‌بینی آزمایش‌ها و شبیه‌سازی‌های بیشتری انجام گیرد.